

**Electronic Structures of Porphyrinoid Complexes
Bearing Paramagnetic Metal Ions**

March 2018

Yuki Ide

Shimane University

Interdisciplinary Graduate School of Science and Engineering

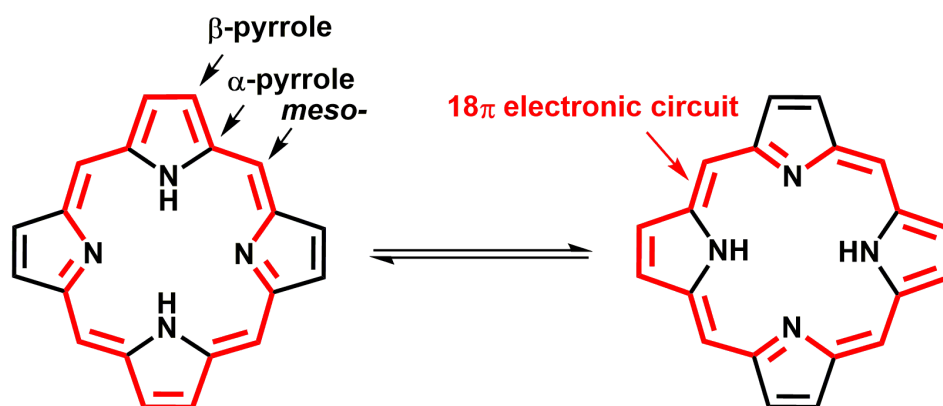
Contents

| | |
|--|-------------|
| General Introduction..... | p 1 |
| 1 Spectroscopic and Magnetic Properties of Nickel(II) Pyrrocorphin Complexes with Pyrrolidine Units by Addition of Pyridine..... | p 17 |
| 2 Spin-crossover Between High-spin ($S=5/2$) and Low-spin ($S=1/2$) States of Six-coordinate Iron(III) Porphyrins with Two Pyridine <i>N</i>-Oxide Derivatives..... | p 44 |
| 3 Synthesis of Oxo-Iron(IV) Porphyrin π-Radical Cation Complex with Pyridine <i>N</i>-Oxide Derivative..... | p 71 |
| Summary..... | p 84 |
| List of Publications..... | p 88 |
| List of Domestic Presentations..... | p 89 |
| List of International Presentations..... | p 92 |
| List of Awards..... | p 93 |
| Acknowledgement..... | p 94 |

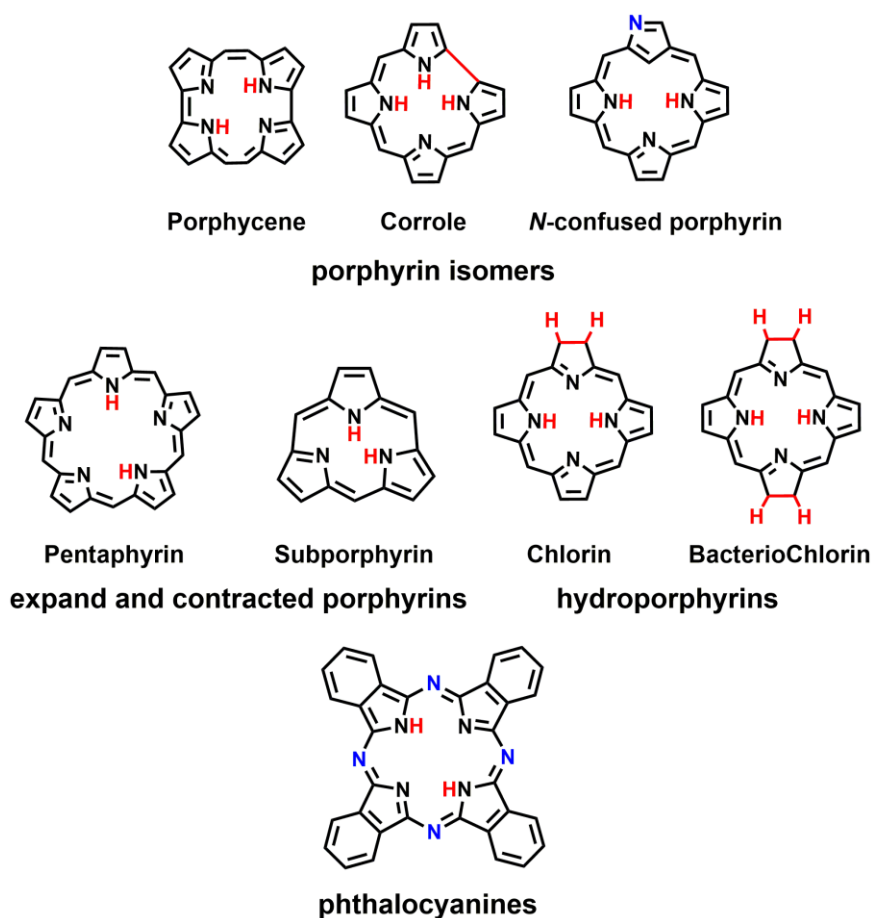
General Introduction

Porphyrioid frameworks

Porphyrioids are π -conjugated macrocycles with porphyrin-like skeletons, and usually exhibit a high degree of aromatic properties [1-3]. Porphyrin frameworks consist of four pyrrole subunits that are connected in a coplanar fashion at their α -carbon atoms through a methine (*meso*-) carbon bridge. The tautomerism of porphyrins occurs rapidly among the four nitrogens in the core, and each tautomer having similar stability exists in the equilibria (Scheme 1). The four inward-orientated pyrrolic nitrogen atoms can serve as an effective, dianionic ligand towards various metal ions to allow for the formation of metalloporphyrins, some of which fulfill catalytic functions in key synthetic reactions. Porphyrins often undergo facile electron-transfer reactions to generate cationic or anionic radicals, thus reflecting their relatively low LUMO (Lowest Unoccupied Molecular Orbital) levels and high HOMO (Highest Occupied Molecular Orbital) levels. Most porphyrins exist as a conjugated 18π -electronic aromatic circuit with rare examples of 16π - or 20π -electronic antiaromatic or non-aromatic species [4-8]. As the other representative chromophore molecules, porphyrin isomers (porphycene, corrole, and *N*-confused porphyrin), expanded and contracted porphyrins (pentaphyrin and subporphyrin), modified hydroporphyrins (chlorin and bacteriochlorin), and phthalocyanines are known as the porphyrioids (Scheme 2). For example, as the most important light-harvesting pigments such as chlorophylls, chlorin consists of three pyrroles and one pyrroline coupled through four methine(*meso*-) linkages, phthalocyanine composes of four 3,4-benzopyrrole(isoindole) subunits inter connected at their α -carbon atoms *via* nitrogen atoms. These modified macrocycles provide new insights into the nature of conjugation and aromaticity in porphyrioid π -system.



Scheme 1. Porphyrin tautomerism.



Scheme 2. Porphyrinoids structures.

Aromatic properties

The research on aromaticity, dating back to Faraday's landmark discovery of benzene [9], has seen a dramatic evolution in the course of the last two centuries [10–12]. During that time, our understanding of π -conjugated molecules has been greatly expanded by complementary and mutually dependent efforts of experimental and theoretical chemists. In fact, the most significant advances in the field have been marked not only by synthetic victories but also by the proposal of successful theoretical models. The quest for nontrivial aromatic molecules had its beginnings in the early work on the annulene series [13,14], and has since continued to encompass a remarkable diversity of structures [15]. The π -conjugation in porphyrinoids is controlled by many factors, including prototropic tautomerism, acid–base equilibria, metal coordination, and redox chemistry [16]. Among these effects, the role of conformational flexibility is especially important because of the diversity of observed structural effects and their apparent complexity. Recently, an increasing number of Möbius aromatic and antiaromatic expanded porphyrins have been produced from *meso*-aryl-substituted expanded porphyrins by metal complexation, fusion reaction, protonation, and deprotonation [17]. One of the simplest ways to confirm the aromaticity

is the measurements of absorption spectra in solution state. For instance, porphyrins exhibit a strong Soret band at 400-450 nm and moderate Q bands at 500-700 nm, whereas chlorins reveal broadened and red-shifted Soret and Q bands together with intensified Q bands relative to the Soret band due to the lower molecular symmetry. On the other hand, phthalocyanines exhibit a moderate Soret band at 300-400 nm and strong Q bands at 600-750 nm. Absorption properties of these are very attractive for artificial photosynthesis and solar energy conversion. In fact, Figure 1 shows UV-Vis spectra of porphyrin and phthalocyanine complexes taken in CHCl_3 solution: (a) NiTPP (TPP: TetraPhenylPorphyrin) and (b) $\text{ZnPc}(4\text{-}^t\text{Bu})_8$ ($\text{Pc}(4\text{-}^t\text{Bu})_8$: Octakis(4-tert-Butylphenoxy)Phthalocyanine).

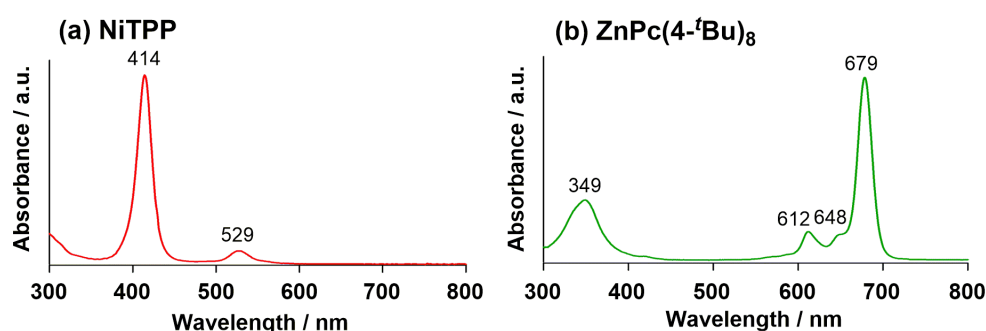


Figure 1. UV-Vis spectra of (a) NiTPP and (b) $\text{ZnPc}(4\text{-}^t\text{Bu})_8$ taken in CHCl_3 solution.

Porphyrioid applications

The unusual physical and chemical properties and beautiful colors of porphyrioid complexes with metal ions have attracted much attention. They are one of the archetypal functional molecules, playing an important role in diverse areas of scientific research owing to its unique electronic and optical properties [18]. In addition, porphyrioid complexes research has a long history, covering a wide variety of disciplines of natural sciences, including photosynthesis, P450-related biocatalysis, organic photovoltaic cells, photodynamic therapeutic agents, bioimaging probes, chemosensors, conductive organic materials, light-emitting materials, near-infrared dyes, nonlinear optical materials, information storage, molecular wires, metal ligands, supramolecules, and so forth [1-3]. To achieve these fascinating functions, various molecular design method have been proposed for controlling the photophysical, electrochemical, and coordination properties of porphyrioid π -systems. For example, hydrophilic substituents are often installed to increase solubility in aqueous media and enhance membrane permeability for cancer therapy applications [19-21]. Porphyrioid complexes for solar cell applications require donor and acceptor moieties at certain positions [22-24]. For energy and electron transfer studies, porphyrioid oligomers with adequate potential gradients have to be prepared. These complexes and elaborate structures are difficult to prepare using only conventional porphyrioid synthesis. Namely, functional groups and substituents are introduced after the construction of the porphyrioid macrocycles in these

types of reactions. Post-functionalization of porphyrinoids can be further classified into two categories: one is core-functionalization and the other is peripheral-functionalization [25]. In the case of core-functionalization, the core-skeleton of the porphyrinoid macrocycle is directly functionalized at the *meso*- and/or β - positions. On the other hand, functional groups can be introduced on the peripheral substituents. The most of these functionalizations are performed using various types of porphyrinoids bearing reactive substituents such as halogens, alkynes, and metals on the porphyrinoid core or the substituents.

Investigation strategy for porphyrinoid complexes

Importantly for inevitable interactions of porphyrins and chlorins with living organisms, the type of the central metal influences their pharmacokinetics [26,27]. Porphyrinoid complexes also receive considerable attention as model compounds of hemes with electron transfer and enzyme functions, as model pigments in photosynthesis research, and as the building blocks of supramolecular devices [28-35]. Encouraged by these features, the synthetic chemistry of porphyrinoids has been extensively developed, giving access to a lot of new compounds in fields that range from materials science to biomedical applications. Many factors are known to influence the reactivity of porphyrinoids, such as the nature of the solvent, the macrocyclic conformation, the coordination of incoming metal ions, and the aggregation effects, particularly strong in porphyrin complexes with small peripheral substituents [36]. Therefore, the electronic structures of porphyrinoid complexes are also strongly determined by inserted metal ions, coordinated axial ligands, peripheral substituents, and steric effects of macrocycles. Their electron distributions, HOMO-LUMO gaps, and thermodynamic parameters have been thoroughly studied using theoretical and experimental methods. As one of theoretical methods, quantum chemical calculations (DFT: density functional theory) were performed for the same set of molecules to examine the influence of structural and electronic factors on the energy of the frontier orbitals, the nucleophilicity/electronegativity of the macrocycle, its hardness, and conformation. On the other hand, experimentally structural, spectroscopic, and electronic data obtained by X-ray crystal structure analyses, NMR (Nuclear Magnetic Resonance) and absorption spectroscopy, and CV (cyclic voltammetry) measurement. As the metalloporphyrinoids having unpaired electrons, magnetic properties can be further investigated by variable-temperature NMR including EVANS method, ESR (Electron Spin Resonance), mössbauer spectroscopy, and SQUID (Superconducting Quantum Interference Device) measurement.

Paramagnetic theories

Paramagnetic molecules are not only a variety of complexes containing the transition metal and rare earth ions but also the oxygen molecule, nitric oxide and a large number of organic free

radicals [37-39]. A magnetic susceptibility is merely the quantitative measure of response of a material to an applied (i.e., external) magnetic field. Paramagnetic susceptibilities depend on the sample, but diamagnetic susceptibilities are temperature independent. The units of susceptibilities are often confusing. For the susceptibility χ , the definition is $M = \chi H$, where M is the magnetization (magnetic moment per unit of volume) and H is the magnetic field strength. This χ is dimensionless, but is expressed as emu/cm³. The dimension of emu is therefore cm³. The molar susceptibility χ_N is obtained by multiplying χ with the molar volume, v (in cm³ / mol). So, the molar susceptibility lead to $M = H\chi_N / v$, or $Mv = \chi_N H$, where Mv is now the magnetic moment per mol. The dimension of molar susceptibility is thus emu / mol or cm³ / mol. Most of chemists omit the subscript on χ in what follows. Another physical quantity important for understanding of magnetic systems is the specific heat. Indeed, non-magnetic study, at least at low temperatures, is complete without the measurement of the specific heat.

In principle χ is the algebraic sum of two contributions associated with different phenomena: $\chi = \chi_{\text{dia}} + \chi_{\text{para}}$ where χ_{dia} and χ_{para} represent the diamagnetic and paramagnetic susceptibilities, respectively. The former is negative and the latter positive. When χ_{dia} dominates, the sample is said to be diamagnetic; it is repelled by the magnetic field. When χ_{para} is the leading contribution, the sample is said to be paramagnetic; it is attracted by the applied field. Diamagnetism is an underlying property of matter. It is always present, even when it is masked by the paramagnetism. The diamagnetism is due to the interaction of the magnetic field with the motion of the electrons in their orbits. The theory of this phenomenon has been well understood for several decades, and, for some small molecules, *ab initio* calculations of the molar diamagnetic susceptibility afford reasonably good results. As a result, χ_{dia} was independent of the temperature and the strength of the applied field. Empirical formulas have been proposed to estimate its value. They are based on the idea that the diamagnetic susceptibility is essentially additive. χ_{dia} can then be roughly calculated either from atomic susceptibilities and constitutive corrections, or from group susceptibilities (group meaning here ligand or counterion). The constitutive corrections are generally positive. They account for the fact that a molecule with multiple or conjugated bonds is less diamagnetic than a rather similar molecule with only single bonds. Pascal et al. tabulated data allowing the application of these additive methods as Pascal's constants [40]. Recently, G. A. Bain and J. F. Berry reported some modified Pascal's constants [41]. When only a very rough estimation of the diamagnetic susceptibility is required, the author can use an equation of the type: $\chi_{\text{dia}} = -k \times MW \times 10^{-6}$ emu mol⁻¹ where MW is the molecular weight of the compound and k is a factor varying between 0.4 and 0.5. For paramagnetic compounds of low molecular weight, the additive methods or even simple method may be sufficient to estimate the diamagnetic contribution χ_{dia} . In such cases, this contribution is indeed small and may even become negligible at low temperature. On the other hand, the accuracy is different when studying compounds of

high molecular weight containing only a few paramagnetic centers. Greater accuracy can sometimes be obtained by the direct measurement of the susceptibility of a diamagnetic analog of the paramagnetic compound which is of interest. In recently researches, π -conjugated compounds with antiaromatic properties may have a quite large paramagnetic contribution χ_{para} .

In sometimes happens that systems with a spin singlet ground state, which from the development presented above would be expected to be diamagnetic, in fact exhibit a weak paramagnetic behavior. This paramagnetism is found to be temperature independent and, since it is only of the order of 10^{-4} emu mol $^{-1}$, is generally more important when considering measurements made at 80 K and above. This temperature independent paramagnetism (TIP) arise from a mixing into the ground state wave function of the excited states that are not thermally populated. TIP is also represented Na . Therefore, magnetic susceptibility containing diamagnetic susceptibility and TIP can be rewritten as follows, $\chi = \chi_{\text{para}} + \chi_{\text{dia}} + \text{TIP } (Na)$.

The molar magnetic susceptibility varies inversely with temperature; this is the Curie law, $\chi = C / T$, which was proposed in 1910 from experimental data before the introduction of quantum mechanics. Here, χ is measured susceptibility, C is called the Curie constant depending on the spin multiplicity of the ground state, and T is the absolute temperature. The diagrammatic illustrations of the Curie law and the inverse of χ are shown in Figure 2(a) and (b), respectively. Since $\chi^{-1} = C^{-1}T$, a plot of χ^{-1} vs. T is a convenient procedure for the determination of Curie constant; note that the line goes through the origin. It should be apparent that a good Curie law magnet will be found only when there are no thermally accessible states whose populations change with changing temperature. Furthermore, the most convenient way to establish experimentally that a compound obeys this Curie law is to obtain a horizontal straight line for the χT versus T plot (Figure 2(c)). The χT means the product of the molar magnetic susceptibility by the temperature. The χT is expressed in emu K mol $^{-1}$. Sometimes magnetic susceptibility data are given in the form of the temperature dependence of the so-called effective magnetic moment μ_{eff} and the units of μ_{eff} is μ_{B} . There are many situations in which the Curie law is not strictly obeyed. One source of the deviations can be the presence of an energy level whose population changes appreciably over the measured temperature interval; another source is the magnetic interactions which can occur between paramagnetic ions and/or radicals. Many paramagnetic materials have interactions which cause them to become antiferromagnets or ferromagnets, and their temperature-dependent properties become even more complex. The difference of these magnetic behaviors correlates closely with the chemical nature of the materials. To the simplest approximation, this behavior is expressed by a small modification of the Curie law, to the Curie-Weiss law, $\chi = C / (T - \theta)$, where the correction term, θ , has the units of temperature. Negative values of θ are common, but this should not be confused with unphysical negative temperatures. The θ is obtained empirically from a plot of χ^{-1} vs. T , as for the Curie law, but now the intercept

with the horizontal axis is not at origin. When θ is negative it is called antiferromagnetic in sign; when θ is positive, it is called ferromagnetic. The constant, θ , characteristic of any particular sample, is best evaluated when $T \cong 10 \times \theta$, as curvature of χ^{-1} usually becomes apparent at smaller values of T .

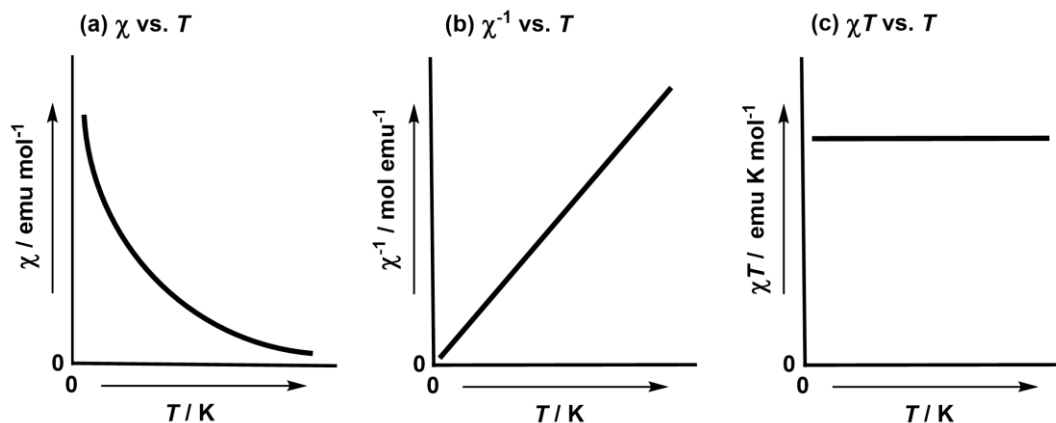


Figure 2. The diagrammatic illustrations of (a) χ vs. T plot for Curie law, (b) χ^{-1} vs. T plot for inverse Curie law, and (c) χT vs. T plot.

The simplest situation in molecular magnetism is that of molecules in which the $^{2S+1}\Gamma$ ground state has no first-order angular momentum and has a large separation in energy from the first excited states, such that any kind of coupling between ground and excited states may be neglected. In the absence of external magnetic field, the $2S+1$ spin degeneracy is then retained. It is convenient to choose the energy of this $^{2S+1}\Gamma$ state as the energy origin. When the field is applied, the energies of the $2S+1$ Zeeman components are given by $E_n = M_s g \beta H$ with M_s varying by an integer value from $-S$ to $+S$. Here, E_n ($n = 1, 2, \dots$) is energy spectrum, M_s is magnetization, g is the gyromagnetic factor or the g -factor, β is the Bohr magneton, and H is an applied magnetic field. Since the first excited states are assumed to be too high in energy to couple with the ground state, g is in principle isotropic and equal to $g_e = 2.0023$ (g_e : g -factor of the free electron); the magnetic properties will be isotropic too. The energies E_n are linear in H . On the other hand, as the case of the excited states supposed to be high enough in energy to be totally depopulated in the temperature range of interest, this coupling may lead to two phenomena, namely the anisotropy of the g -factor, and, if the spin S associated with the ground state is larger than $1/2$, the zero-field splitting. The correct interpretation of a series of magnetic measurements requires an accurate and uniquely defined spin Hamiltonian. The spin Hamiltonian is often divided into several components. The zero-field splitting within a $^{2S+1}\Gamma$ state without first-order angular momentum is expressed by the phenomenological Hamiltonian $H_{ZFS} = \mathbf{S} \cdot \mathbf{D} \cdot \mathbf{S}$ where \mathbf{S} is spin momentum operators and \mathbf{D} is a symmetric and traceless tensor. In matrix notation the total spin Hamiltonian taking into account the Zeeman perturbation is then $\mathbf{H} = \beta \mathbf{S} \cdot \mathbf{g} \cdot \mathbf{H} + \mathbf{S} \cdot \mathbf{D} \cdot \mathbf{S}$ where β is

the Bohr magneton, g is g -tensor, and H is an applied magnetic field. Assuming that the D - and g -tensors have some principal axes, the total spin Hamiltonian may be rewritten as $H = \beta \mathbf{S}_u \cdot g_u \cdot H_u + D[\mathbf{S}_z^2 - S(S + 1) / 3] + E(\mathbf{S}_x^2 - \mathbf{S}_y^2)$ where the index u notes the direction of the applied magnetic field; g_u is the value of g -factor and \mathbf{S}_u is the component of \mathbf{S} along this direction. D and E are the axial and rhombic zero-field splitting parameters, respectively. D and E are related to the principal values D_{uu} ($u = x, y, z$) of the D -tensor through $D = 3D_{zz} / 2$ and $E = |D_{xx} - D_{yy}| / 2$. The zero-field splitting are often responsible for deviations from Curie law behavior, they give rise to a characteristic specific heat behavior, and they limit the usefulness of certain substance for adiabatic demagnetization. Furthermore, zero-field splitting cause a single-ion anisotropy which is important in charactering anisotropic exchange, and are also one of the sources of canting or weak ferromagnetism. The population of the energy levels then depends, by the Boltzmann principle, on the relative value of the zero-field splitting parameter D and the thermal energy kT . The fact that D not only has magnitude but also sign is of large consequence for many magnetic system. An axial crystalline field is capable of causing a zero-field splitting establishes a principal or symmetry axis in the metal-containing molecule, and it is important to specify whether that axis of the molecule is oriented parallel to the field (H_{\parallel}), perpendicular (H_{\perp}) or at some intermediate direction. The name “zero-field splitting” arises from the fact that the splitting occurs in the absence of a magnetic field. If the energy levels of a system are known, the magnetic susceptibility may always be calculated by application of Van Vleck’s equation [42,43]. In fact, many susceptibility measurements are made on powdered paramagnetic samples, so that only the average susceptibility χ_{ave} is obtained. The quantity χ_{ave} is defined as $\chi_{\text{ave}} = (\chi_{\parallel} + 2\chi_{\perp}) / 3$, where χ_{\parallel} and χ_{\perp} are the susceptibility measured with the field parallel and perpendicular to the principal axis. One of the principal applications of ESR measurements to the study of transition metal ions is the determination of spin Hamiltonian parameters [44]. When metal ions are put into diamagnetic hosts in small concentration, this is one of the most accurate ways of determining g -factors and zero-field splitting that are relatively small. ESR measurements can also confirm the magnetic interactions between the paramagnetic molecular centers.

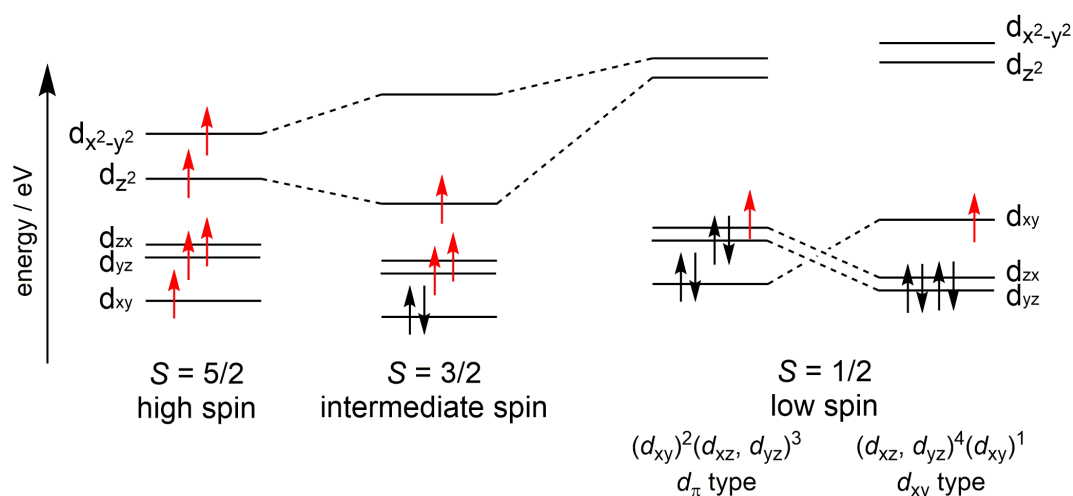
There is no doubt that the most important developments in molecular magnetism have concerned compounds where several magnetic centers interact. These magnetic moment carriers may be transition metal ions, rare earths, or organic radicals. The principles concerning short-range order that evolve here are useful for studies on more-extended systems. The most thoroughly investigated dinuclear compounds by far are those involving copper(II) ions, where the interaction occurs between two local doublet states. Considering a compound of this nature, two copper(II) ions (noted A and B) in the same molecular entity are bridged by a diamagnetic ligand capable of transmitting the electronic effects between A and B. If the two metal ions interact through the bridge, then the local spins $S_A = S_B = 1/2$ are not good quantum numbers. The good spin quantum

numbers are $S = 0$ and 1. Let $E(S = 0)$ and $E(S = 1)$ be the energies of the two pair states. $E(S = 0)$ and $E(S = 1)$ are in general not equal, but separated by a J energy gap defined as $J = E(S = 0) - E(S = 1)$. J value is often referred to as the isotropic interaction parameters. When the state $S = 0$ is the ground state, the interaction is said to be antiferromagnetic; J value is then negative. When the state $S = 1$ is the ground state, the interaction is said to be ferromagnetic and J value is positive. This latter situation is much less frequent than the former. As the application of Van Vleck's equation to energy levels for a pair of $S = 1/2$ ions undergoing antiferromagnetic exchange, the isothermal magnetic susceptibility (χ) per mol of dimers is readily calculated as: $\chi = 2Ng^2\beta^2 / kT[3 + \exp(-J/kT)]$ where N is Avogadro constant ($6.022 \times 10^{23} \text{ mol}^{-1}$), g is the g -factor, β is the Bohr magneton ($9.274 \times 10^{-24} \text{ J T}^{-1}$), k is Boltzmann constant ($1.381 \times 10^{-23} \text{ J K}^{-1}$), and T is the absolute temperature (K). This equation (called Bleaney-Bowers equation) was derived for the first time by Bleaney and Bowers. For $J < 0$, the magnetic susceptibility presents a maximum, and then tends to zero when T approaches zero. Indeed, at low temperature, only the diamagnetic ground state is thermally populated. This maximum in χ is a signature of antiferromagnetic interaction. On the other hand, for $J > 0$, on cooling, χ increases faster than in C/T . The best way to reveal a ferromagnetic interaction is to plot χT versus T . For $J = 0$, χT is constant and equal to $Ng^2\beta^2/2k$. For $J > 0$, χT is close to $2Ng^2\beta^2$ when $kT \gg J$. On cooling, χT increases, due to the depopulation of the diamagnetic excited state in favor of the triplet ground state, and tends to a plateau with $\chi T = 2Ng^2\beta^2/3k$ corresponding to the temperature range where the excited singlet state is fully depopulated. The ratio $(\chi T)_{\text{LT}} / (\chi T)_{\text{HT}}$ between the low- and high-temperature limits is equal to 4/3. Therefore, for $J < 0$, χT continuously decreases upon cooling. The isotropic interaction phenomenon is purely electrostatic in nature. It is often formally described by a coupling between the local spin operators S_A and S_B . The phenomenological Hamiltonian accounting for this may be written as $H = -2JS_A \cdot S_B$. Such a phenomenological description of the isotropic interaction was introduced first by Heisenberg, then discussed by Dirac and Van Vleck. H is generally called the Heisenberg-Dirac-Van Vleck (HDVV) Hamiltonian.

Electronic structures for iron(III) porphyrin complexes

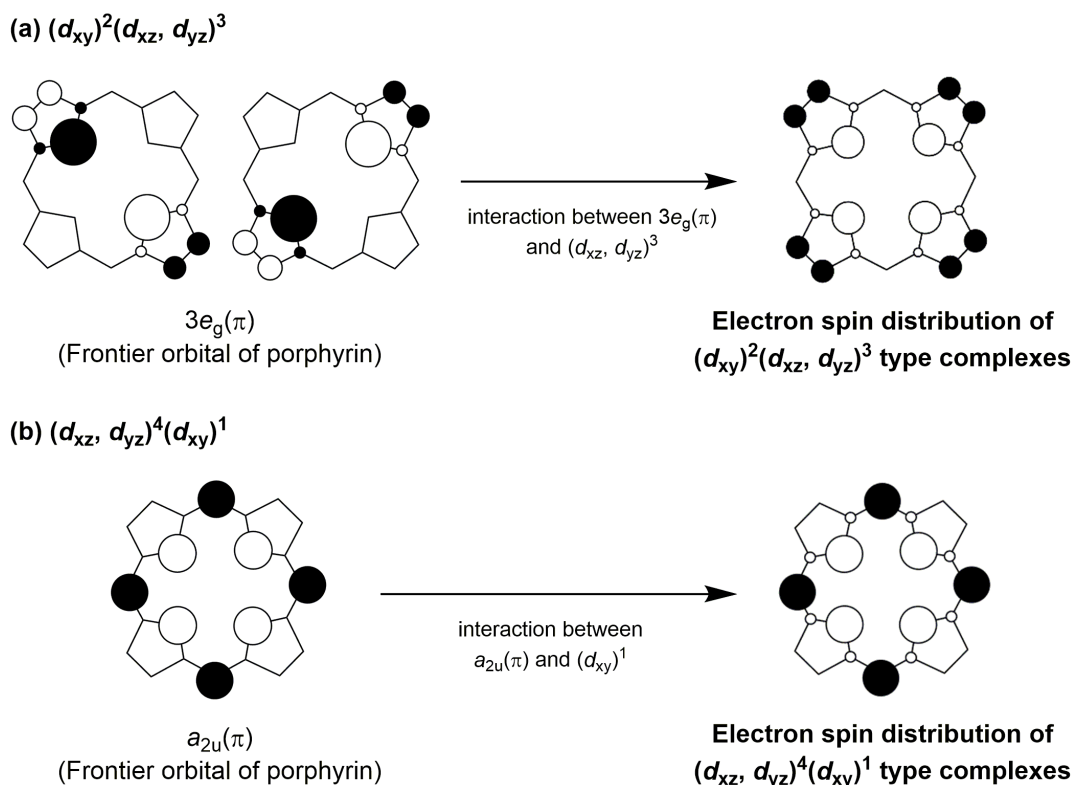
The most famous example having paramagnetic molecules is heme. Iron porphyrin complexes exist for heme within an organism. The active centers in heme proteins such as cytochrome P450, peroxidase, and catalase have a very important function of electron transfer and enzyme by the difference of axial ligands. For example, peroxidase and catalase, when activated by peroxides or peracids, form an oxo iron(IV) porphyrin π -cation radical intermediate called Compound I [45-47]. Compound I is also believed to be an active intermediate in the reactions of oxygenases such as cytochrome P450 [48-51]. The compound I in cytochrome P450 directly transfers a single oxygen atom to a variety of substrates. It is generally accepted that the diverse functions of

compound I are controlled by heme environmental structures, such as porphyrin peripheral structures, heme axial ligands, and protein structures around heme. Therefore, elucidation of the electronic structures in a variety of iron porphyrin complexes as model compounds is quite important to understand the function and catalytic processes of naturally occurring heme proteins. Various techniques have been used to solve this question, which include UV–Vis, NMR, EPR, resonance Raman, IR, MCD, Mössbauer, EXAFS, SQUID, X-ray crystallography, DFT calculation and so forth [52-55]. Among these techniques, NMR and ESR spectroscopy are highly desirable because they serve a detailed information on the electronic structures of the complexes with paramagnetic properties in solution at various temperatures. In addition, solution magnetic susceptibilities of paramagnetic porphyrinoids can also be determined by the Evans methods in deuterated solvent using non deuterated solvent as the chemical shift reference [56]. In the case of iron(III) porphyrin complexes, the half-occupied metal *d* orbitals can interact with the porphyrin π -molecular orbitals having the same symmetry. Consequently, unpaired electron delocalizes to the specific carbon and nitrogen atoms. The NMR signals for carbon and hydrogen atoms exhibit upfield or downfield shifts as the paramagnetic shifts. Many chemists can determine which *d* orbital has unpaired electron by the analysis of the observed ^1H and ^{13}C NMR chemical shifts. In other words, these chemical shifts can be a good probe to reveal the electronic structure of iron(III) porphyrin complexes. Through the extensive studies using ^1H and ^{13}C NMR spectroscopy, it is now clear that the spin states of iron(III) porphyrin complexes are controlled by the nature and number of the axial ligands and deformation of the porphyrin ring. Iron(III) ion has five electrons at *d* orbital. While the six-coordinate complexes carrying axial ligands with strong field strength such as imidazole and cyanide exhibit a low-spin ($S = 1/2$: one unpaired electron) state, the five-coordinate complexes carrying an anionic ligand such as halide and acetate show a high-spin ($S = 5/2$: five unpaired electrons) state. If the field strengths of anionic ligands become fairly weak, the complexes adopt a rare intermediate spin ($S = 3/2$: three unpaired electrons) state as shown in Scheme 3. The energy levels of the five *d* orbitals are perturbed to give a unique electronic structure. Since the symmetries of metal *d* and porphyrin π -orbitals vary depending on the deformation modes of porphyrin ring, the chemical shifts of the peripheral carbon and hydrogen atoms should be quite different between two complexes even if the electronic structure of the paramagnetic metal ions is the same. Since the porphyrin deformation is commonly observed in naturally occurring heme proteins, it is very important to elucidate the effect of porphyrin deformation on the physicochemical properties of the complexes [57,58]. There are two types of electronic ground state in low-spin iron(III) porphyrin complexes. One is the commonly observed ground state with the $(d_{xy})^2(d_{xz}, d_{yz})^3$ electron configuration (d_π type) and the other is the less common ground state with the $(d_{xz}, d_{yz})^4(d_{xy})^1$ electron configuration (d_{xy} type) as shown in Scheme 3. Previously studies have revealed that the ground state of low-spin



Scheme 3. Spin states and electron configurations of iron(III) porphyrin complexes.

complexes is controlled by the electronic nature of axial ligands and deformation structure of the porphyrin ring [53]. Electron configuration of the low-spin complexes causes tremendous influence on the NMR spectroscopy. In the case of the $(d_{xy})^2(d_{xz}, d_{yz})^3$ type complexes, the unpaired electron in the iron d_π orbitals delocalizes to the porphyrin ring through the interaction with the porphyrin($3e_g$) orbitals. Because the $3e_g$ orbital has sizable coefficients on the β -pyrrole carbon and nitrogen atoms and zero coefficient on the *meso*- carbon atoms as shown in Scheme 4(a), the interaction shifts the pyrrole-H signal to the upfield position [59]. On the other hand, X-ray crystallographic studies of the $(d_{xz}, d_{yz})^4(d_{xy})^1$ type complexes have revealed that the porphyrin core of these complexes commonly exhibits the highly ruffled structure [60]. Upon ruffling deformation, the symmetry of six-coordinate metalloporphyrin will be lowered from D_{4h} to D_{2d} [61,62]. As shown in Table 4, both the iron d_{xy} and porphyrin a_{2u} orbitals are represented as b_2 in ruffled D_{2d} complex and therefore they can interact. In other word, the complex is stabilized due to the d_{xy} - a_{2u} interaction by ruffling the porphyrin core. As a result, the unpaired electron in the d_{xy} orbital delocalizes to the porphyrin ring especially on the *meso*- carbon and pyrrole nitrogen atoms because the a_{2u} orbital has large coefficients at these atoms as shown in Scheme 4(b). As the result, the pyrrole-H signal slightly shifts to the downfield position due to the zero coefficients at the β -pyrrole carbons in the a_{2u} orbital [63]. Variable temperature NMR study is often possible not only to characterize the electronic ground state but also to determine the possible existence of a thermally accessible excited state by the using Curie plots. The Curie plot is plot of paramagnetic shift (δ) vs. $1/T$ for the signals of paramagnetic complex. Here, T is the absolute temperature. If these plots have the linearity, the paramagnetic complex maintains a constant of electronic structure and spin state by following the Curie law. The chemical shifts of observed signals in the NMR spectra of paramagnetic complexes are the sum of two contributions,



Scheme 4. Electron spin distributions of (a) the $(d_{xy})^2(d_{xz}, d_{yz})^3$ and (b) $(d_{xz}, d_{yz})^4(d_{xy})^1$

$\delta_{\text{obs}} = \delta_{\text{dia}} + \delta_{\text{para}}$, δ_{obs} is the observed chemical shift, δ_{dia} is the diamagnetic chemical shift, and δ_{para} is the paramagnetic chemical shift for the corresponding signals, respectively [64]. The paramagnetic chemical shift (δ_{para}) is also called the isotropic shift (δ_{iso}) and the hyperfine shift (δ_{hf}). An accurate approximation of the diamagnetic shift can be obtained from a diamagnetic compound that is similar to the paramagnetic one being studied. The paramagnetic shift can be

Table 4. Correlation table for the porphyrin complexes MO's [61,62].

| | D _{4h} | D _{2d} | D _{2d} | C _{4v} | C _{2v} | C _{2v} |
|------------------|-----------------|-----------------|-----------------|-----------------|-----------------|-----------------|
| | planar | ruffled | saddled | domed | ruffled | saddled |
| Metal | | | | | | |
| $d_{x^2-y^2}$ | b_{1g} | b_1 | b_2 | b_1 | a_2 | a_1 |
| d_{z^2} | a_{1g} | a_1 | a_1 | a_1 | a_1 | a_1 |
| d_{xz}, d_{yz} | e_g | e | e | e | b_1, b_2 | b_1, b_2 |
| d_{xy} | b_{2g} | b_2 | b_1 | b_2 | a_1 | a_2 |
| Porphyrin | | | | | | |
| 4 e_g^* (LUMO) | e_g | e | e | e | b_1, b_2 | b_1, b_2 |
| a_{1u} (HOMO) | a_{1u} | b_1 | b_1 | a_2 | a_2 | a_2 |
| a_{2u} (HOMO) | a_{2u} | b_2 | b_2 | a_1 | a_1 | a_1 |
| 3 e_g | e_g | e | e | e | b_1, b_2 | b_1, b_2 |

subdivided into two parts, $\delta_{\text{para}} = \delta_{\text{con}} + \delta_{\text{dip}}$, δ_{con} means the contact shift and δ_{dip} mean the electron-nuclear dipolar shift (or the pseudocontact shift: δ_{pc}) [65]. The contact shift term represents the paramagnetic shift of the resonance from the diamagnetic position caused by the delocalization of the unpaired electron through bonds. The second contribution to the observed chemical shift is the paramagnetic shift, which is also known as the isotropic the delocalization of the unpaired electron through bonds. If the delocalization occurs through σ bonds the sign of the contact shift is positive. This results in a positive shift of the resonance. If the delocalization occurs through π bonds, the sign of the contact shift for a proton attached to a carbon that is part of the π system is negative, and the observed shift is negative. The electron-nuclear dipolar shift results from the through space interaction between the unpaired electron at the metal center and the nucleus being studied and may be approximated as the following if the second-order Zeeman contribution to the magnetic susceptibilities is small and the ground state is well-separated from any excited states. Goff has shown that for bis-imidazole complexes of iron(III) porphyrin complexes the quantity $[2g_{zz}^2 - (g_{xx}^2 + g_{yy}^2)]$ is very similar whether calculated from ESR g values or from NMR data, suggesting that the second-order Zeeman term is probably quite small for these bis-imidazole complexes [66,67].

EPR spectroscopy is also a good method to elucidate the electron configuration and magnetic interaction of a variety of paramagnetic molecules containing iron(III) complexes at an extremely low temperature. In addition, g -, D and E values for g -factor and zero-field splitting parameters can be determined by using the simulation of observed ESR spectra. In the case of low spin iron(III) complexes, the complexes with the $(d_{xz}, d_{yz})^4 (d_{xy})^1$ ground state exhibit axial type spectra where g_{xx} and g_{yy} are nearly the same and they are larger than g_{zz} . The complexes with the $(d_{xy})^2 (d_{xz}, d_{yz})^3$ ground state show either rhombic or “large g_{max} ” type spectra. Extensive studies have revealed that the relative orientation of planar axial ligands determines the spectral type of the low-spin complexes [53,59]. Complexes carrying parallel aligned ligands exhibit the rhombic type spectra, here three signals are observed at $g_1 = 1.5\text{--}1.9$, $g_2 = 2.2\text{--}2.4$, and $g_3 = 2.5\text{--}2.9$. In contrast, the complexes carrying perpendicularly aligned ligands give large g_{max} type spectra, where a single strong signal appears at $g = 3.2\text{--}3.7$. The complexes with linear ligands such as cyanide also exhibit the large g_{max} type spectra. It is possible that the low-spin complex has two isomers with different ligand orientation; one has parallel aligned and the other has perpendicularly aligned ligands. In such a case, both rhombic and large g_{max} type signals can be observed even in frozen solution if the interconversion is slow on the ESR timescale [68].

Outlook for novel porphyrinoid complexes

Recently, novel porphyrinoids of π -conjugated macrocycles such as modified hydroporphyrins (chlorin, bacteriochlorin, and isobacteriochlorin), porphyrin isomers (porphycene, corrole, and N -

confused porphyrin), and expanded or contracted porphyrins (pentaphyrin and subporphyrin) have been synthesized by employing the exceptional reactions, reagents, and techniques. Although new porphyrinoid complexes containing paramagnetic metal ions attract an interest of many scientists, their investigated data are still insufficient due to the highly complex electron structure and some interaction between paramagnetic ions and/or free-radicals. In this dissertation, as the model compounds of active center in heme proteins, the author synthesized porphyrinoid complexes bearing the paramagnetic metal ions, confirmed the structure by X-ray crystal structure, and investigated the spectroscopic and magnetic properties both in solution and solid states by the UV-Vis, NMR, ESR, Mossbauer spectra, and SQUID measurements.

References

- [1] *The porphyrin hand book* (Eds.: K. M. Kadish, K. M. Smith, R. Guillard), Academic Press, San Diego, 2000.
- [2] *Hand book of porphyrin science* (Eds.: K. M. Kadish, K. M. Smith, R. Guillard), World Scientific, Singapore, 2010.
- [3] B. Szyszko, M. J. Białek, E. Pacholska-Dudziak, L. Latos-Grażyński, *Chem. Rev.* 2017, 117, 2839–2909.
- [4] J. A. Cissell, T. P. Vaid, G. P. A. Yap, *J. Am. Chem. Soc.* 2007, 129, 7841–7847.
- [5] Y. Yamamoto, A. Yamamoto, S. Furuta, M. Horie, M. Kodama, W. Sato, K. Akiba, S. Tsuzuki, T. Uchimaruru, D. Hashizume, F. Iwasaki, *J. Am. Chem. Soc.* 2005, 127, 14540–15541.
- [6] J. A. Cissell, T. P. Vaid, A. L. Rheingold, *J. Am. Chem. Soc.* 2005, 127, 12212–12213.
- [7] C. Liu, D.-M. Shen, Q.-Y. Chen, *J. Am. Chem. Soc.* 2007, 129, 5814–5815.
- [8] A. Weiss, M. C. Hodgson, P. D. W. Boyd, W. Siebert, P. J. Brothers, *Chem. Eur. J.* 2007, 13, 5982–5993.
- [9] M. Faraday, *Philos. Trans. R. Soc. London* 1825, 115, 440–446.
- [10] *Aromaticity and Antiaromaticity. Electronic and Structural Aspects* (Eds.: V. I. Minkin, M. N. Glukhovtsev, B. Y. Simkin), Wiley-Interscience, New York, 1994.
- [11] P. v. R. Schleyer, *Chem. Rev.* 2001, 101, 1115–1117.
- [12] P. v. R. Schleyer, *Chem. Rev.* 2005, 105, 3433–3435.
- [13] R. M. Willstätter, W. von Schmaedel, *Ber. Dtsch. Chem. Ges.* 1905, 38, 1992–1999.
- [14] R. M. Willstätter, E. Waser, *Ber. Dtsch. Chem. Ges.* 1911, 44, 3423–3445.
- [15] *Chemical Science of π -Electron Systems* (Eds.: T. Akasaka, A. Osuka, S. Fukuzumi, H. Kandori, Y. Aso), Springer, Japan, 2015.
- [16] M. Stępień, L. Latos-Grażyński in *Topics in Heterocyclic Chemistry*, Vol. 19 (Eds.: T. M. Krygowski, M. K. Cyrański), 2009, pp. 83–153.
- [17] T. Tanaka, A. Osuka, *Chem. Rev.* 2017, 117, 2584–2640.

- [18] J. Fabian, H. Nakazumi, M. Matsuoka, *Chem. Rev.* 1992, 92, 1197–1226.
- [19] R. Bonnett, *Chemical Aspects of Photodynamic Therapy*, Gordon and Breach Science Publishers, Australia, 2000.
- [20] E. D. Sternberg, D. Dolphin, C. Brückner, *Tetrahedron* 1998, 54, 4151–4202.
- [21] M. Obata, S. Hirohara, R. Tanaka, I. Kinoshita, K. Ohkubo, S. Fukuzumi, M. Tanihara, S. Yano, *J. Med. Chem.* 2009, 52, 2747–2753.
- [22] T. Hasobe, H. Imahori, P. V. Kamat, T. K. Ahn, S. K. Kim, D. Kim, A. Fujimoto, T. Hirakawa, S. Fukuzumi, *J. Am. Chem. Soc.* 2005, 127, 1216–1228.
- [23] K. Kurotobi, Y. Toude, K. Kawamoto, Y. Fujimori, S. Ito, P. Chabera, V. Sundström, H. Imahori, *Chem. Eur. J.* 2013, 19, 17075–17081
- [24] B. C. O'Regan, I. López-Duarte, M. V. Martínez-Díaz, A. Forneli, J. Albero, A. Morandeira, E. Palomares, T. Torres, J.R. Durrant, *J. Am. Chem. Soc.* 2008, 130, 2906–2907.
- [25] S. Hiroto, Y. Miyake, H. Shinokubo, *Chem. Rev.* 2017, 117, 2910–3043.
- [26] D. K. Lavalley, *Coord. Chem. Rev.* 1985, 61, 55–96.
- [27] P. Hambright, *Coord. Chem. Rev.* 1971, 6, 247–268.
- [28] A. Eschenmoser, *Angew. Chem. Int. Ed.* 2011, 50, 12412–12472.
- [29] K. Zheng, P. D. Ngo, V. L. Owens, X. Yang, S. O. Mansoorabadi, *Science* 2016, 354, 339–342.
- [30] J. Geng, L. Huoa, A. Liu, *J. Inorg. Biochem.* 2017, 167, 60–67.
- [31] G. Hartwich, L. Fiedor, I. Simonin, E. Cmiel, W. Schafer, D. Noy, A. Scherz, H. Scheer, *J. Am. Chem. Soc.* 1998, 120, 3675–3683.
- [32] D. Noy, L. Fiedor, G. Hartwich, H. Scheer, A. Scherz, *J. Am. Chem. Soc.* 1998, 120, 3684–3693.
- [33] A. Drzewiecka-Matuszek, A. Skalna, A. Karocki, G. Stochel, L. Fiedor, *J. Biol. Inorg. Chem.* 2005, 10, 453–462.
- [34] A. Tsuda, A. Osuka, *Science* 2001, 293, 79–82.
- [35] J. Y. Lee, O. K. Farha, J. Roberts, K. A. Scheidt, S. B. T. Nguyen, J. T. Hupp, *Chem. Soc. Rev.* 2009, 38, 1450–1459.
- [36] D. Dolphin, *The Porphyrins*, Academic Press, New York, 1978.
- [37] R. L. Carlin, *Magnetochemistry*, Springer-Verlag, Berlin, 1986.
- [38] C. J. O'connor, *Progress in Inorg. Chem.* 1982, 29, 203–283.
- [39] O. Kahn, *Molecular Magnetism*, VCH, Weinheim, 1993.
- [40] P. Pascal, *Ann. Chim. Phys.* 1910, 19, 5.
- [41] G. A. Bain, J. F. Berry, *J. Chem. Educ.* 2008, 85, 532–536.
- [42] J. H. Van Vleck, *The Theory of Electric and Magnetic Susceptibilities* Oxford University Press, London, 1932.
- [43] J. H. Van Vleck, *J. Phys. Radium.* 1951, 12, 262–274.
- [44] H. W. J. Blöte, W. J. Huiskamp, *Phys. Lett.* 1969, A29, 304–305.

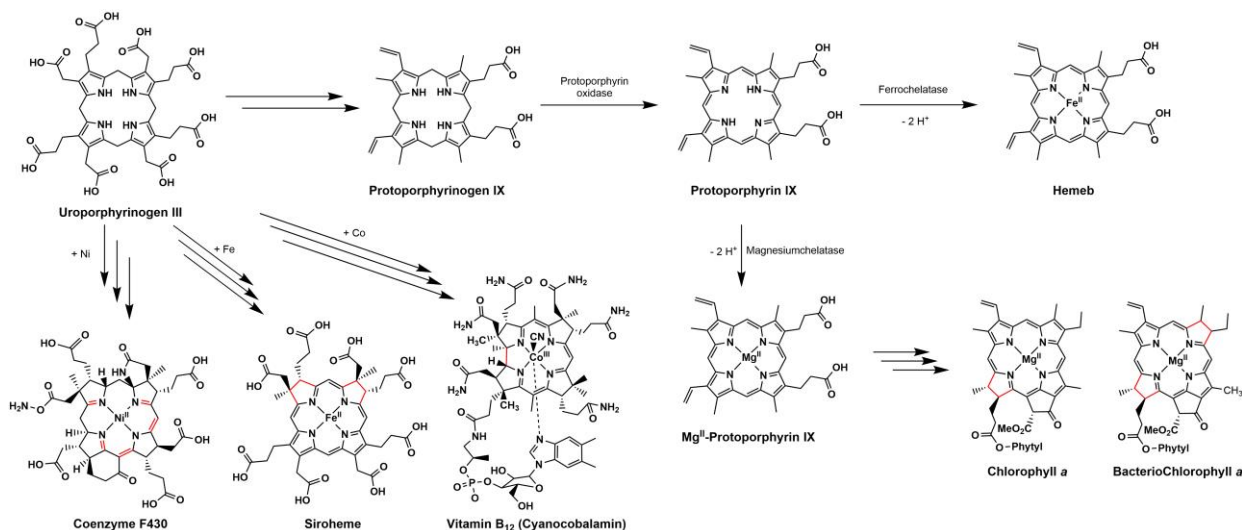
- [45] H. -P. Hersleth, U. Ryde, P. Rydberg, C. H. Görbitz, K. K. Andersson, *J. Inorg. Biochem.* 2006, 100, 460–476.
- [46] H. B. Dunford, *Heme Peroxidases*, Wiley-VCH, New York, 1999.
- [47] H. N. Kirkman, G. F. Gaetani, *Trends Biochem. Sci.* 2007, 32, 44–50.
- [48] I. G. Denisov, T. M. Makris, S. G. Sliger, I. Schlichting, *Chem. Rev.* 2005, 105, 2253–2278.
- [49] P. R. Ortiz de Montellano, *CytochromeP450. Structure, Mechanism, and Biochemistry*, 2nd ed., Plenum Publishing Corporation, New York, 1995.
- [50] A. Takahashi, T. Kurahashi, H. Fujii, *Inorg. Chem.* 2009, 48, 2614–2625.
- [51] J. T. Groves, R. Quinn, T. J. McMurry, M. Nakamura, G. Lang, Brian Boso, *J. Am. Chem. Soc.*, 1985, 107, 354–360.
- [52] *Inorganic Electronic Structure and Spectroscopy* (Eds.: E. I. Solomon, A. B. P. Lever), John Wiley & Sons, Inc., New York, 1999.
- [53] M. Nakamura, *Coord. Chem. Rev.* 2006, 250, 2271–2294.
- [54] A. Ikezaki, Y. Ohgo, M. Nakamura, *Coord. Chem. Rev.* 2009, 253, 2056–2069.
- [55] F. A. Walker, U. Simonis, *Iron Porphyrin Chemistry.*, Encyclopedia of Inorganic Chemistry, John Wiley & Sons, Ltd., USA, 2006.
- [56] D. F. Evans, T. A. James, *J. Chem. Soc., Dalton Trans.* 1979, 723–726.
- [57] R. -J. Cheng, P. -Y. Chen, P. -R. Gau, C. -C. Chen, S. -M. Peng, *J. Am. Chem. Soc.* 1997, 119, 2563–2569.
- [58] J. A. Shelnut, X. -Z. Song, J. -G. Ma, S. -L. Jia, W. Jentzen, C. J. Medforth, *Chem. Soc. Rev.* 1998, 27, 31–41.
- [59] F. A. Walker, *Chem. Rev.* 2004, 104, 589–615.
- [60] M. K. Safo, F. A. Walker, A. M. Raitsimring, W. P. Walters, D. P. Dolata, P. G. Debrunner, W. R. Scheidt, *J. Am. Chem. Soc.* 1994, 116, 7760–7770.
- [61] R. -J. Cheng, P. -Y. Chen, T. Lovell, T. Liu, L. Noodleman, D. A. Case, *J. Am. Chem. Soc.* 2003, 125, 6774–6783.
- [62] J. Conradie, A. Ghosh, *J. Phys. Chem. B.* 2003, 107, 6486–6490.
- [63] T. Ikeue, Y. Ohgo, T. Saitoh, M. Nakamura, H. Fujii, M. Yokoyama, *J. Am. Chem. Soc.* 2000, 122, 4068–4076.
- [64] C. T. Watson, S. Cai, N. V. Shokhirev, F. A. Walker, *Inorg. Chem.* 2005, 44, 7468–7484.
- [65] F. A. Walker, *Inorg. Chem.* 2003, 42, 4526–4544.
- [66] H. M. Goff, Nuclear Magnetic Resonance of Iron Porphyrins. *In Iron Porphyrins, Part One* (Eds.: A. B. P. Lever, H. B. Gray), Addison-Wesley: Reading, MA, 1983, pp. 249.
- [67] W. D. Horrocks, E. S. Greenberg, *Mol. Phys.* 1974, 27, 993–999.
- [68] T. Ikeue, T. Yamaguchi, Y. Ohgo, M. Nakamura, *Chem. Lett.* 2000, 29, 342–344.

1 Spectroscopic and Magnetic Properties of Nickel(II) Pyrrocorphin Complexes with Pyrrolidine Units by Addition of Pyridine

1.1 Introduction

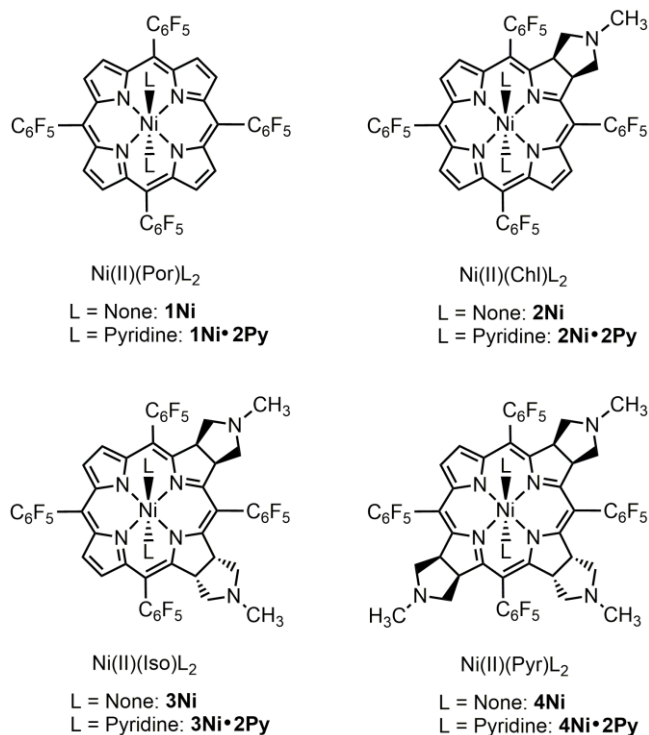
Porphyrimoids are macrocycles with porphyrin-like skeletons [1-4]. In recent years, great effort has been focused on the development and improvement of new methods to convert porphyrins into hydroporphyrins such as dihydroporphyrins (chlorins), tetrahydroporphyrins (isobacteriochlorins and bacteriochlorins), and hexahydroporphyrins (pyrrocorphin). This is mainly due to the potential use of these compounds as photosensitizers in photodynamic therapy (PDT) for various cancers [5-7]. Although there are ample studies on the synthesis and characterization of hydroporphyrins such as chlorin, bacteriochlorin, and isobacteriochlorin as well as their metal complexes, little is known on the spectroscopic properties of further reduced porphyrimoids such as pyrrocorphins and their metal complexes [1-2,8-13].

In nature, highly reduced hydroporphyrins and their metal complexes are playing important roles as shown in Scheme 1-1. For example, coenzyme F430, which is the prosthetic group of methyl coenzyme M reductase in methanogenic and anaerobic methanotrophic archaea, is known to have Ni(II) corphin structure with only five peripheral double bonds [14-16]. Recently, Zheng et al. reported that the biosynthesis of coenzyme F430 from sirohemochlorin proceeds via four steps [17]. Furthermore, siroheme is a heme-like prosthetic group at the active sites of some enzymes to accomplish the six-electron reduction of sulfur and nitrogen [18]. It is a cofactor at the active



Scheme 1-1. Hydroporphyrin compounds within organism.

site of sulfite dehydrogenase, which plays a major role in sulfur assimilation pathway, converting sulfite into sulfide, which can be incorporated into the organic compound homocysteine [19]. The sequence begins with the insertion of nickel and iron mediated by a chelatase, similar to the biosynthesis of vitamin B₁₂ (cobalamine); vitamin B₁₂ is a Co(III) complex of another highly reduced porphyrinoid named corrin [20-22]. The macrocyclic ligand in coenzyme F430, siroheme, and vitamin B₁₂ is derived from uroporphyrinogen III [23,24]. This porphyrinogen is methylated at two adjacent pyrrole rings to give dihydrosirohydrochlorin, which is subsequently oxidized to give sirohydrochlorin. In the case of metal-free compounds, pyrrocorphin is less stable than the corresponding porphyrinogen. In the presence of a complexing metal ion and a base, however, the equilibrium lies on the side of the pyrrocorphin. Some years ago, Kratky et al. reported the X-ray structural analyses of Ni(II) complexes of diastereomeric 2,3,7,8,12,13,17,18-octaethylpyrrocorphins [25]. More recently, Cavaleiro et al. reported three kinds of diastereomeric pyrrolidine-fused pyrrocorphins by 1,3-dipolar cycloadditions of azomethine ylides to 5,10,15,20-tetrakis(pentafluorophenyl)porphyrin [26]. These compounds are quite stable in spite of the presence of the highly reduced porphyrin ring. Quite recently, Herges et al. used porphyrin **1**, chlorin **2**, and isobacteriochlorin **3** reported by Cavaleiro et al. and converted them to the corresponding Ni(II) complexes, **1Ni**, **2Ni**, and **3Ni** as shown in Scheme 1-2 [27]. Although square planar Ni(II) complexes were diamagnetic, the corresponding six-coordinate pyridine



Scheme 1-2. Ni(II) complexes examined in this study. Abbreviations: porphyrin (Por), chlorin (Chl), isobacteriochlorin (Iso), and pyrrocorphin (Pyr).

ligated complexes, **1Ni•2Py**, **2Ni•2Py**, and **3Ni•2Py**, showed paramagnetic $S = 1$ spin state. Consequently, the spectroscopic properties changed drastically by the addition of pyridine. These authors called the phenomena as *coordination-induced spin-state switching* (CISSS). Interestingly, the binding constants of pyridine toward four-coordinate Ni(II) complexes showed a large increase on going from porphyrin **1Ni** to chlorin **2Ni**, and then to isobacteriochlorin **3Ni**. These results have attracted our attention since the author have been studying the effect of the reduced porphyrin ring on the physicochemical properties of the metal complexes.

In this section, the author would like to show the structural, spectroscopic, redox, and magnetic properties of Ni(II) complexes of pyrrocorphin together with those of the five- and six-coordinate pyridine ligated complexes, **4Ni•Py** and **4Ni•2Py**, by means of UV-Vis, ^1H NMR, CV, SQUID, and X-ray crystallography as well as DFT calculations. The author will also compare these properties with those of the corresponding porphyrin, chlorin, and isobacteriochlorin complexes reported by Herges et al.

1.2 Experimental

1.2.1 Instrumentation

Elemental analyses for carbon, hydrogen, and nitrogen were conducted using a Yanako CHN CORDER MT-6. UV-Vis absorption spectra were recorded in CH_2Cl_2 and pyridine solution on a Shimadzu UV-3100 spectrometer. Reflectance spectra were recorded on a Shimadzu ISR-3100 spectrometer. ^1H and ^{19}F NMR spectra were recorded on a JEOL Delta ECX-500 spectrometer operating at 500.1 and 470.6 MHz for ^1H and ^{19}F , respectively. Chemical shifts for ^1H signals were referenced to the residual solvent protons of CDCl_3 , CD_2Cl_2 , and pyridine- d_5 ($\delta = 7.24$, 5.32 , and 7.19 ppm, respectively). Chemical shifts of ^{19}F NMR spectra were referenced to hexafluorobenzene ($\delta = -164.9$ ppm). Mass spectra were recorded on a Bruker microTOF using positive mode ESI-TOF method for acetonitrile solutions by using sodium formate as reference. Cyclic voltammograms were measured on a BAS ALS-DY2325 electrochemical analyzer. Samples were dissolved in CH_2Cl_2 solution containing tetrabutylammonium hexafluorophosphate (TBAPF_6). A glassy carbon disk (3.0 mm radius), platinum wire, and saturated calomel electrode (SCE) were used as working, counter, and reference electrodes, respectively. The solid-state magnetic susceptibilities were measured between 2 and 300 K under a magnetic field of 0.5 T on Quantum Design MPMS-7 and MPMS-7XL SQUID magnetometers. The fitting curves were obtained by using EasySpin software package [28].

1.2.2 Syntheses and Complex Data

1.2.2.1 Syntheses of free base porphyrinoids

Free base pyrrocorphin was prepared by the method developed by Cavaleiro et al. as shown in Scheme 1-1 [26,29]. Thus, the 1,3-dipolar cycloaddition of an azomethine ylide to *meso*-tetrakis(pentafluorophenyl)porphyrin, H₂(TPFP)Por **1•H₂** gave corresponding chlorin, H₂(TPFP)Chl **2•H₂** and diastereomeric isobacteriochlorins, *cctc*- and *cccc*-H₂(TPFP)Iso **3•H₂** and **3a•H₂**, respectively. Pure *cctc*-H₂(TPFP)Iso **3•H₂** was then treated with the azomethine ylide to give *cctctc*-H₂(TPFP)Pyr **4•H₂** as described below.

1.2.2.2 Synthesis of *cctctc*-H₂(TPFP)Pyr: **4•H₂** [26]

Successive additions of sarcosine (88.2 mg, 990 μmol) and paraformaldehyde (74.5 mg, 2.48 mmol) to a refluxed toluene (30 mL) solution of **3** (539 mg, 495 μmol) were made every 12 h, for totally 72 h under a nitrogen atmosphere. After being cooled to room temperature, the reaction mixture was separated by chromatography on silica gel using CH₂Cl₂/acetone (10:1) as an eluent. Unreacted **3•H₂** was eluted followed by **4•H₂**, which was further purified by the preparative TLC using CH₂Cl₂/acetone (10:1) as an eluent. Yield: 76.3 mg (66.6 μmol, 13.4%).

1.2.2.3 Synthesis of Ni(II)[*cctctc*-(TPFP)Pyr]: **4Ni**

The nickel complex of pyrrocorphin **5** was obtained by the following procedure. Free base pyrrocorphin **4•H₂** (27.1 mg, 23.7 μmol) and nickel(II) acetylacetonate dihydrate (18.3 mg, 71.1 μmol) were dissolved in toluene (30 ml) and refluxed for 24 h under a nitrogen atmosphere. The solvent was removed under reduced pressure. The reaction mixture was dissolved in CHCl₃ (100 ml), washed with water (3 × 100 ml), and then the organic layer was extracted with CH₂Cl₂. The solution was evaporated and dried *in vacuo* at rt to remove low boiling substances. The residual solid was dissolved in CH₂Cl₂ and separated by preparative TLC on silica gel with the use of CH₂Cl₂/acetone (10:1) as an eluent to give unchanged isobacteriochlorin **4•H₂** followed by the nickel complex **4Ni** (12.9 mg, 10.7 μmol) as purple crystals in 45 % yield. Anal. Found: C, 52.30; H, 2.54; N, 7.68%. Calcd for C₅₃H₂₉N₇F₂₀Ni+H₂O: C, 52.16; H, 2.56; N, 8.03%. ¹H NMR (CD₂Cl₂, 500 MHz, 298 K): δ 2.09 (N-CH₃, 3H, br), 2.13 (N-CH₃, 6H, br), 2.27 (CH₂, 4H, br), 2.34 (CH₂, 2H, br), 2.48 (CH₂, 4H, br), 2.55 (CH₂, 2H, br), 3.80 (pyrrolidine-CH, 2H, br), 3.95 (pyrrolidine-CH, 4H, br), and 6.63 ppm (pyrrole β-H, 2H, br). ¹⁹F NMR (CD₂Cl₂, 470 MHz, 298 K): δ = -137.7 (*o*-F, 2F, br), -138.2 (*o*-F, 2F, br), -139.7 (*o*-F, 2F, d, *J* = 21.9 Hz), -142.4 (*o*-F, 2F, d, *J* = 23.8 Hz), -154.6 (*p*-F, 2F, br), -157.4 (*p*-F, 2F, br), -162.5

(*m*-F, 4F, br), -164.4 (*m*-F, 2F, br), and -164.6 ppm (*m*-F, 2F, br). UV-vis (CH₂Cl₂): λ_{\max}/nm ($\log \epsilon$) = 349 (2.9), 406 (3.0), 519 (0.4), 598 (1.0), and 647 nm (1.7). Reflectance: λ_{\max} = 346, 406, 534, and 659 nm. HR-MS (ESI-TOF): Found: 1202.1570, Calcd. for [C₅₃H₂₉N₇F₂₀Ni+H]⁺ : 1202.1591 m/z.

1.2.2.4 Synthesis of Ni(II)[*cctctc*-(TPFP)Pyr](Py)₂: 4Ni•2Py

Nickel complex **4Ni** (40.3 mg, 33.5 μmol) was dissolved in pyridine, from which the crude solid was obtained after the evaporation of pyridine. Recrystallization of the solid from pyridine/hexane gave 44.6 mg (98 %) of **4Ni•2Py**. Anal. Found: C, 55.44; H, 3.08; N, 9.32 %. Calcd. for C₆₃H₃₉N₉F₂₀Ni: C, 55.61; H, 2.89; N, 9.26 %. ¹H NMR (pyridine-*d*₅, 500 MHz, 298 K): δ = -21.0 (pyrrolidine-CH, 2H, br), -17.5 (pyrrolidine-CH, 2H, br), -0.93 (pyrrolidine-CH, 2H, br), 1.17 (N-CH₃, 3H, br), 1.22 (N-CH₃, 6H, br), 5.83 (CH₂, 2H, br), 7.46 (CH₂, 6H, br), 8.34 (CH₂, 2H, br), 8.59 (CH₂, 2H, br), and 57.2 ppm (pyrrole β -H, 2H, br). ¹⁹F NMR (pyridine-*d*₅, 470 MHz, 298 K): δ = -138.2 (*o*-F, 2F, br), -140.0 (*o*-F, 2F, br), -140.2 (*o*-F, 2F, br), -142.4 (*o*-F, 2F, br), -155.0 (*p*-F, 2F, br), -157.5 (*p*-F, 2F, br), -163.7 (*m*-F, 2F, br), -163.8 (*m*-F, 2F, br), -165.0 (*m*-F, 2F, br), and -165.6 ppm (*m*-F, 2F, br). UV-vis (pyridine): $\lambda_{\max}(\log \epsilon)$ = 360 (6.0), 399 (4.5), 416 (5.3), 486 (0.5), 579 (1.2), and 631 nm (3.0). Reflectance: λ_{\max} = 357, 409, 487, 539, 586, 633, 729, 779, and 826 nm. HR-MS (ESI-TOF): Found: 1201.1541, Calcd. for [C₅₃H₂₉N₇F₂₀Ni - 2(C₅H₅N)]⁺: 1201.1513 m/z.

1.2.3 X-ray Crystallography on 4Ni•2Py

Single crystals of **4Ni•2Py** suitable for X-ray structure analysis were obtained by recrystallization from the pyridine/hexane mixed-solvent solution. X-ray measurements were done with Rigaku VariMax Saturn-724 (1.2 kW Mo rotating anode) at 100 K. Diffraction data were processed using Crystal Clear 1.6.3 followed by CrystalStructure Ver. 4.0.1. The structures were solved using SUPERFLIP and expanded using the Fourier technique [30]. All calculations were performed using the CrystalStructure crystallographic software package [31]. The structure was refined on F^2 by full-matrix least-squares using the SHELXL-2014 program package [32]. Crystal data and details concerning the data collection are given in Table 1-1. All non-hydrogen atoms were refined anisotropically. Hydrogen atoms were located in the calculated positions and refined by using riding models. Large electron peaks near the special position (0 0 0) were found probably due to the disordered solvent molecule. The author failed to model them properly. Therefore, the original diffraction data were modified by the PLATON SQUEEZE technique in order to refine the structure without the disordered solvent molecules [33]. The final structure was

validated by Platon CIF check. Selected bond distances and angles are listed in Table 1-2. Crystallographic data for complex **4Ni•2Py** reported in this paper have been deposited with the Cambridge Crystallographic Data Centre, CCDC no. 1557743.

Table 1-1. Crystal data and data collection details for **4Ni•2Py**.

| | |
|--|--|
| Empirical formula | C ₆₃ H ₃₉ N ₉ F ₂₀ Ni · C ₅ H ₅ N + 1.5(C ₆ H ₁₄) |
| Formula weight | 1569.10 |
| Temperature (K) | 100(2) |
| Wave length (Å) | 0.71075 |
| Crystal system | Triclinic |
| Space group | P-1 |
| a (Å) | 14.137(5) |
| b (Å) | 15.767(5) |
| c (Å) | 16.864(5) |
| α(°) | 90.935(3) |
| β(°) | 95.332(7) |
| γ(°) | 107.881(5) |
| Volume (Å ³) | 3558(2) |
| Z | 2 |
| Density (Calculated) (g cm ⁻³) | 1.465 |
| Absorption coefficient (mm ⁻¹) | 0.378 |
| F (000) | 1610.0 |
| Crystal size (mm) | 0.250 x 0.050 x 0.050 |
| θ Range for data collection (°) | 1.847 to 28.000 |
| Index ranges | -18<=h<=18, -20<=k<=20, -22<=l<=22 |
| Reflections collected | 17120 |
| Independent reflections | 13374 [<i>R</i> _{int} = 0.0856] |
| Max. and Min. transmission | 0.981 and 0.870 |
| Refinement method | Full-matrix least-squares on <i>F</i> ² |
| Data/restraints/parameters | 17120 / 367 / 1079 |
| Goodness-of-fit on <i>F</i> ² | 1.064 |
| Final <i>R</i> indices (<i>I</i> >2σ(<i>I</i>)) | <i>R</i> ₁ = 0.0856, w <i>R</i> ₂ = 0.2097 |
| <i>R</i> indices (all data) | <i>R</i> ₁ = 0.1068, w <i>R</i> ₂ = 0.2265 |
| Largest peak and hole (e Å ⁻³) | +0.917 and -0.616 |

Table 1-2. Structural parameters of **4Ni•2Py** and related complexes.

| Complexes | Ni-N ^c / Å | Ni-N ^d / Å | ΔNi ^e / Å | tilt ^f / ° | τ ^g / ° | φ ^h / ° | θ ⁱ / ° | RMS ^j / Å | space group |
|------------------------------|-----------------------|--------------------------|-----------------------|-------------------------|--------------------|-------------------------|--------------------|----------------------|--------------------|
| 1Ni•2Py ^a | 2.047 | 2.223 (Py ¹) | 0.000 | 0.41 (Py ¹) | 0.0 | 24.9 (Py ¹) | 0.0 | 0.030 | P-1 |
| | | 2.223 (Py ²) | | 0.41 (Py ²) | | 24.9 (Py ²) | | | |
| | | 2.223 (ave) | | 0.41 (ave) | | 24.9 (ave) | | | |
| 2Ni•2Py ^a | 2.062 | 2.185 (Py ¹) | 0.003 | 0.72 (Py ¹) | 1.4 | 39.4 (Py ¹) | 23.8 | 0.072 | P2 ₁ /c |
| | | 2.199 (Py ²) | | 10.6 (Py ²) | | 21.3 (Py ²) | | | |
| | | 2.192 (ave) | | 5.66 (ave) | | 30.4 (ave) | | | |
| 3aNi•2Py ^a | 2.060 | 2.181 (Py ¹) | 0.039 | 3.65 (Py ¹) | 3.1 | 17.9 (Py ¹) | 29.6 | 0.169 | P-1 |
| | | 2.192 (Py ²) | | 9.92 (Py ²) | | 43.4 (Py ²) | | | |
| | | 2.187 (ave) | | 6.79 (ave) | | 30.7 (ave) | | | |
| 4Ni•2Py ^b | 2.089 | 2.170 (Py ¹) | 0.008 | 3.64 (Py ¹) | 1.6 | 44.4 (Py ¹) | 78.3 | 0.127 | P-1 |
| | | 2.178 (Py ²) | | 8.36 (Py ²) | | 33.2 (Py ²) | | | |
| | | 2.174 (ave) | | 6.00 (ave) | | 38.8 (ave) | | | |

^a Cited from Herges and co-workers.²⁷

^b This work.

^c Average value of the four Ni–N(porphyrin) bond lengths.

^d Ni–N(pyridine) bond length.

^e The out-of-plane displacement of Ni(II) ion.

^f Tilt angle of each pyridine ligand from the heme normal.

^g The maximum torsion angle between the four macrocycle nitrogen atoms.

^h The orientation angle of the axial ligand to the nearest NP–Fe–NP axis

ⁱ The dihedral angle between two pyridine ligands.

^j The RMS values for deformation of the macrocycles(C₂₀N₄).

1.2.4 Theoretical Calculation

All calculations were carried out using the *Gaussian 09* program [34]. The initial geometry of **4Ni•2Py** was obtained from its X-ray structure. Full optimizations were performed with Becke's three-parameter hybrid exchange functional and the Lee–Yang–Parr correlation functional (B3LYP) and the 6-31G(d) basis set for all atoms [35-37]. For the high spin complex, unrestricted open-shell calculations were conducted. The calculated absorption wavelengths and oscillator strengths were obtained for the optimized geometry with the TD-DFT method at the B3LYP/6-31G(d) level.

1.3 Results

1.3.1 X-ray crystallography

Figure 1-1 shows the molecular structure of **4Ni•2Py** determined by X-ray crystallography at 100 K. Table 1-2 lists the selected structural parameters of **4Ni•2Py** together with those of the corresponding porphyrin **1Ni•2Py**, chlorin **2Ni•2Py**, and isobacteriochlorin **3Ni•2Py** [27]. The geometry around the Ni(II) ion in **4Ni•2Py** was octahedral with tetragonal distortion. As the number of the saturated pyrrole rings increased, the Ni–N equatorial bonds increased while the Ni–N axial bonds decreased. As revealed from the RMS values, the macrocycle ring of **4Ni•2Py** was slightly more distorted as compared with those of the analogous complexes listed in Table 1-2; the RMS values were calculated on the basis of the deviation of 24 atoms from the mean porphyrin plane. Figure 1-2 shows perpendicular displacement of the peripheral carbon (black) and nitrogen (blue) atoms from the C₂₀N₄ least-square plane. The maximum deviations among pyrrole β-carbon and *meso*-carbon atoms from the average porphyrin plane were 0.323 and 0.135 Å, respectively. As compared with the six-coordinate Ni(II) complexes, the related four-

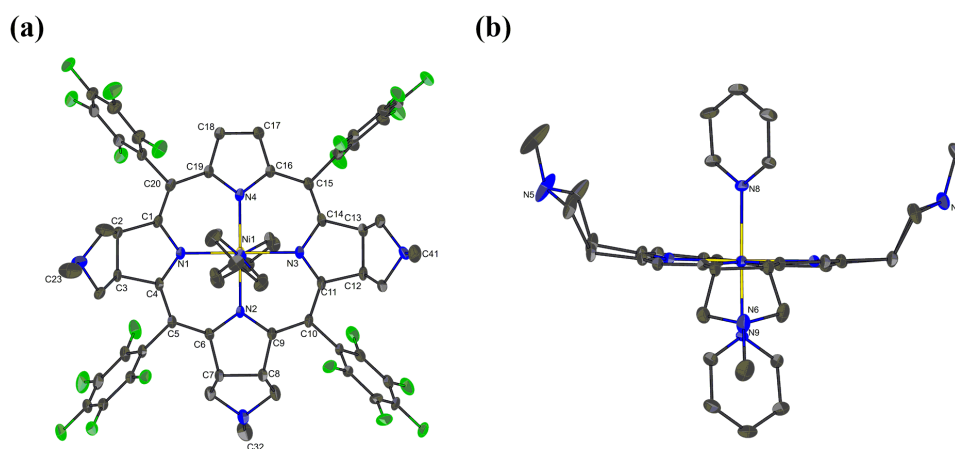


Figure 1-1. ORTEP drawings of **4Ni•2Py** at 100 K with the 30% probability thermal ellipsoids. (a) Top view and (b) Side view.

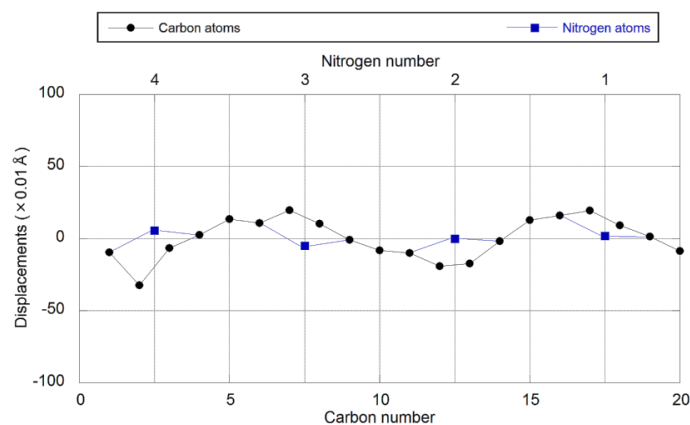


Figure 1-2. Perpendicular displacements of the peripheral carbon (black) and nitrogen (blue) atoms from the least-square plane ($C_{20}N_4$) in **4Ni·2Py**. Atom numbers corresponding to the ones in Figure 1-1.

coordinate Ni(II) complexes were more nonplanar and the Ni–N equatorial bonds were shorter in average [1,25,38-40]. As shown in Figure 1-3, the DFT calculation at the B3LYP/6-31G(d) level of theory provided the optimized structure of four-coordinate **4Ni**, which exhibited the large distortion from the $C_{20}N_4$ least-square plane (RMS value was 0.323 Å) and shorter Ni–N equatorial bonds (the average Ni–N bond length was 1.918 Å). Bond length alternations of the pyrrocorphin core for **4Ni·2Py** are depicted in Figure 1-4, which indicated that the peripheral carbon-carbon bond lengths are classified into two groups, i.e. 1.326–1.438 Å and 1.506–1.539 Å. The dihedral angle (θ) between the axially coordinating pyridine ligands in **4Ni·2Py** was much larger than the corresponding angles in other three complexes, i.e. 78° vs. $0\sim 30^\circ$. Thus, the two pyridine ligands were aligned nearly along the C_{meso} –Ni– C_{meso} axes and took mutually perpendicular orientation as shown in Figure 1-1(a). Correspondingly, the optimized structure of **4Ni·2Py** shows in Figure 1-5 also confirmed the similar orientation in the axial ligand orientation (θ was 82°).

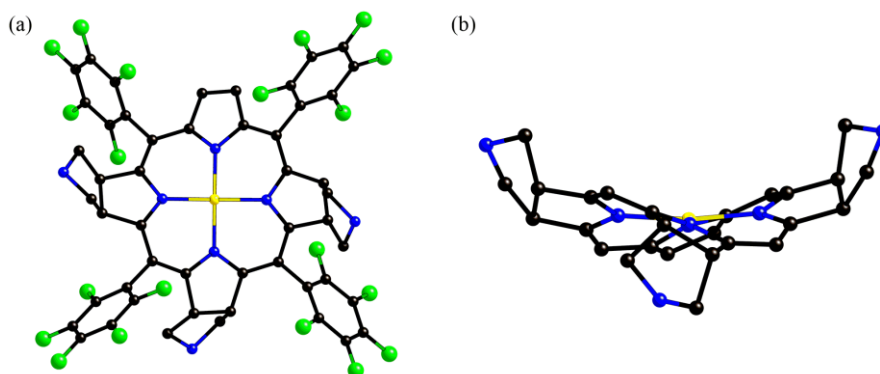


Figure 1-3. Optimized structure of **4Ni**. (a) Top view and (b) side views. Hydrogen atoms, *N*-methyl groups, and *meso*-pentafluorophenyl groups (only side view) are omitted for clarity.

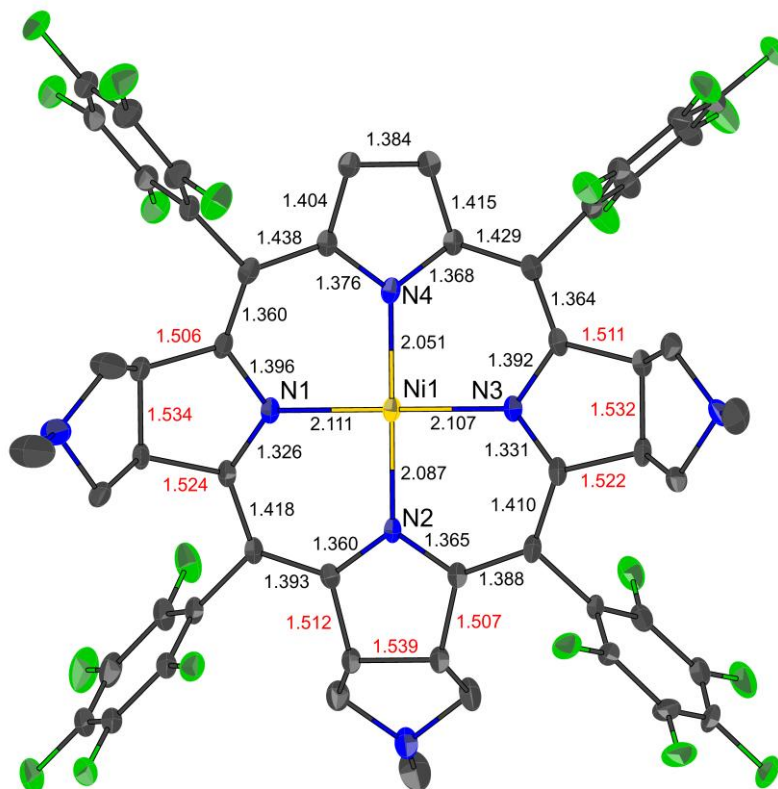


Figure 1-4. Crystal structure of $4\text{Ni}\cdot 2\text{Py}$ (100 K). Hydrogen atoms, and solvents are omitted for clarity. The thermal ellipsoids are scaled at 50% probability level. Selected bond lengths are also shown.

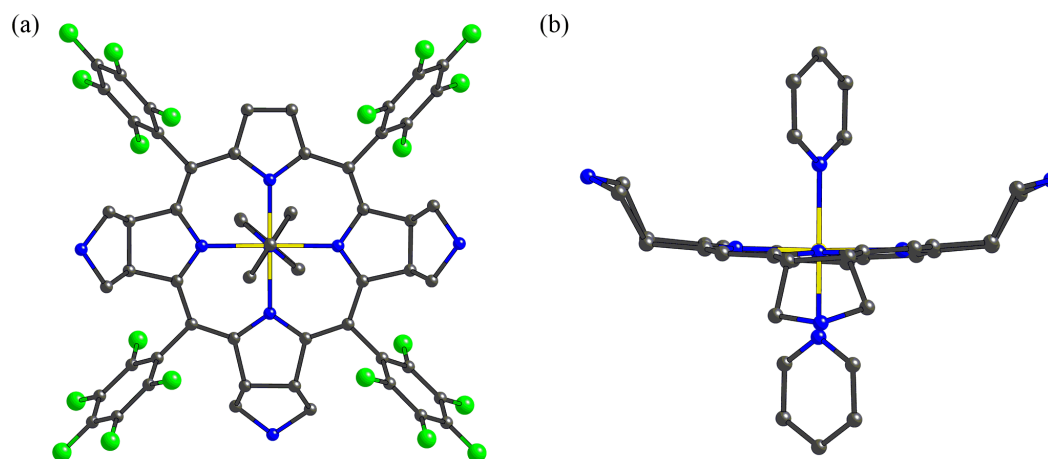


Figure 1-5. Optimized structure of $4\text{Ni}\cdot 2\text{Py}$. (a) Top view and (b) side view. Hydrogen atoms, *N*-methyl groups, and *meso*-pentafluorophenyl groups (only side view) are omitted for clarity.

1.3.2. SQUID Magnetometry

Figure 1-6 shows the temperature dependence of the effective magnetic moment (μ_{eff}) of powdered **4Ni•2Py**. The effective magnetic moment was maintained at $2.96 \pm 0.01 \mu_{\text{B}}$ between 300 and 15 K, which is slightly higher than the spin-only value for a pure $S = 1$ state, *i.e.* $\mu_{\text{eff}} = 2.83 \mu_{\text{B}}$. The solid line in Figure 1-6 represents a spin-Hamiltonian simulation with a zero-field splitting of $D = +4.41 \text{ cm}^{-1}$ and $g_{\text{mean}} = 2.21$.

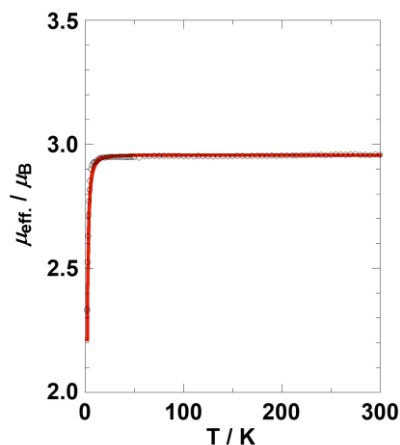


Figure 1-6. Temperature dependence of the effective magnetic moments of **4Ni•2Py** taken for the microcrystalline sample by SQUID magnetometry. The solid line in red represents a simulation with a zero-field splitting of $D = +4.41 \text{ cm}^{-1}$, $S = 1$, and $g_{\text{mean}} = 2.21$.

1.3.3 Electrochemistry

Figure 1-7 illustrates a cyclic voltammogram (CV) of four-coordinate **4Ni** taken in a CH_2Cl_2 solution containing 0.1 M tetrabutylammonium hexafluorophosphate (TBAPF_6) as supporting electrolyte at a glassy carbon working electrode and a saturated calomel electrode (SCE). Two well-defined oxidations and one reduction were observed at $E_{1/2} = +0.79$, $+0.40$, and -1.05 V vs

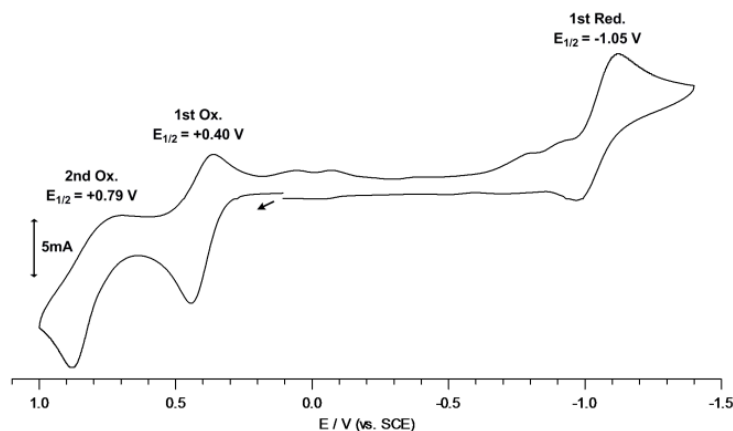


Figure 1-7. Cyclic voltammogram of $\text{Ni(II)[(TPFP)Pyr}] \mathbf{4Ni}$ in a CH_2Cl_2 solution at a glassy carbon working electrode with a scan rate 0.05 V s^{-1} , $[\mathbf{4Ni}] = 1 \times 10^{-3} \text{ M}$, and $[\text{TBAPF}_6] = 0.1 \text{ M}$.

SCE. In Table 1-3 are listed the half-wave potentials for the 1st and 2nd oxidations and reductions together with the potential differences between the HOMO and the LUMO of **4Ni** as well as those of **1Ni–3Ni**.

Table 1-3. Half-wave potentials (V vs. SCE) for a series of Ni(II) complexes in a CH₂Cl₂ solution containing 0.1 M TBAPF₆.

| Complexes | 2 nd ox $E_{1/2}$ (V) | 1 st ox $E_{1/2}$ (V) | 1 st red $E_{1/2}$ (V) | 2 nd red $E_{1/2}$ (V) | ΔE^a (V) |
|------------|----------------------------------|----------------------------------|-----------------------------------|-----------------------------------|------------------|
| 1Ni | 1.54 | 1.42 | -0.92 | -1.43 | 2.34 |
| 2Ni | 1.48 | 1.19 | -0.89 | -1.37 | 2.08 |
| 3Ni | 1.23 | 0.82 | -1.06 | n.d. | 1.88 |
| 4Ni | 0.79 | 0.40 | -1.05 | n.d. | 1.45 |

^a The electrochemical HOMO–LUMO gap.

1.3.4 NMR Spectroscopy

Figure 1-8(a) shows the ¹H NMR spectra of **4Ni** taken in a CDCl₃ solution at 298 K. All the signals in **4Ni** appeared in a so-called diamagnetic region in a CDCl₃ solution, indicating clearly that four-coordinate complex is diamagnetic. The spectrum changed drastically in a pyridine-*d*₅ solution as shown in Figure 1-8(b). Some signals appeared extremely downfield or upfield because of the conversion of four-coordinate diamagnetic **4Ni** to six-coordinate paramagnetic (*S* = 1) **4Ni•2Py** in the presence of a large amount of pyridine. Table 1-4 lists the ¹H NMR chemical shifts taken in CDCl₃ and pyridine-*d*₅ solutions.

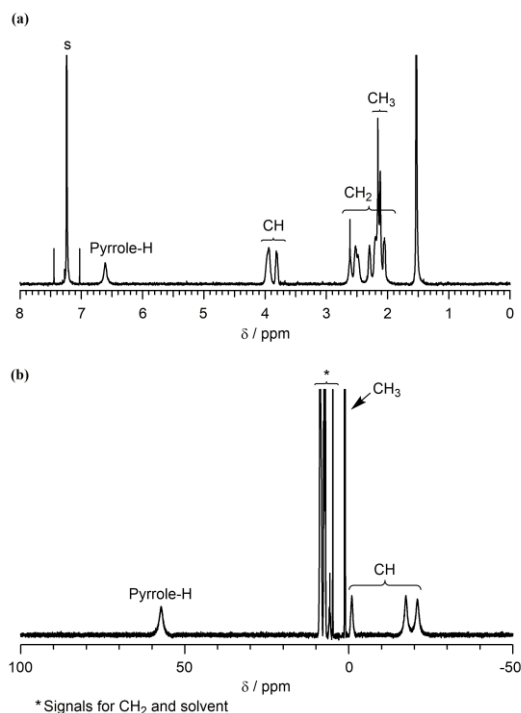


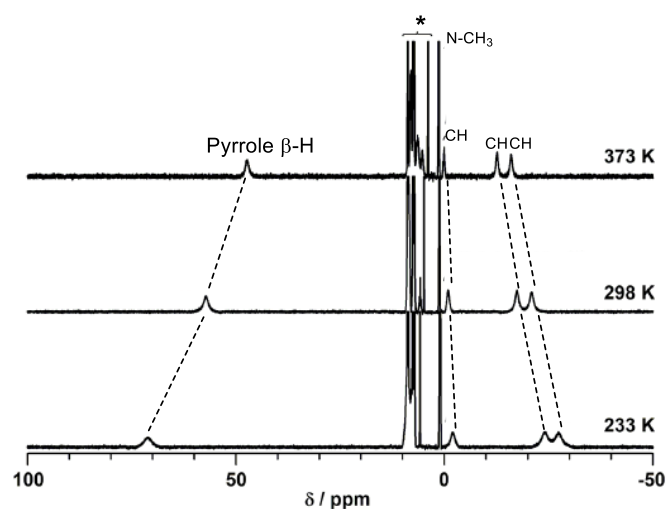
Figure 1-8. ¹H NMR spectra of **4Ni** taken in (a) CDCl₃ and (b) pyridine-*d*₅ solutions.

Table 1-4. ^1H NMR chemical shifts.

| Compounds | porphyrin | | <i>N</i> -methylpyrrolidine | |
|-----------------------------|-------------------------------------|--|--|------------------------|
| | Pyrrole-H | CH | CH ₂ | CH ₃ |
| 1Ni^a | 8.79 (s) | | | |
| 2Ni^a | 8.38 (d) 8.26 (s) 8.02 (d) | 4.94 (t) | 3.08 (m) 2.51 (m) | 2.32 (s) |
| 3Ni^a | 7.74 (s) 7.31 (s) | 4.37 (m) 4.28 (m) | 2.87 (m) 2.73 (m) 2.35–2.25 (m) | 2.22 (s) |
| 4Ni^b | 6.61 (br) | 3.81 (br) 3.94 (br) 3.97 (br) | 2.06 (br) 2.20 (br) 2.30 (br) 2.48 (br) 2.52 (br) 2.61 (br) | 2.12 (s) 2.16 (s) |
| 1Ni•2Py^c | 54.2 (br) | | | |
| 2Ni•2Py^c | 51.7 (br) 54.4 (br) 55.6 (br) | –9.21 (br) | 7.19 (br) 8.44 (br) | 1.37 (br) |
| 3aNi•2Py^c | 53.0 (br) 56.9 (br) | –17.1 (br) –7.59 (br) | 6.59 (br) 8.19 (br) 8.30 (br) | 1.26 (br) |
| 4Ni•2Py^c | 57.2 (br) | –21.0 (br) –17.5 (br) –0.93 (br) | 5.83 (br) 7.46 (br) 8.34 (br) 8.59 (br) | 1.17 (br) 1.22 (br) |

^a Reported by Herges et al. in CDCl₃. ^b This work. Taken in CDCl₃. ^c This work. Taken in pyridine-*d*₅.

Figure 1-9 shows the temperature dependent ^1H NMR spectra of **4Ni•2Py** taken in pyridine-*d*₅ solution. The pyrrole proton signal observed at 57.2 ppm at 298 K moved downfield while three CH signals at –21.0, –17.5, and –0.93 ppm moved upfield as the temperature was lowered. Figure 1-10 shows the Curie plots of **4Ni•2Py** taken in (a) pyridine-*d*₅ and (b) CD₂Cl₂ solutions. The solid



* This part contains CH₂ and solvent signals.

Figure 1-9. Temperature dependent ^1H NMR spectra of **4Ni•2Py** taken in pyridine-*d*₅.

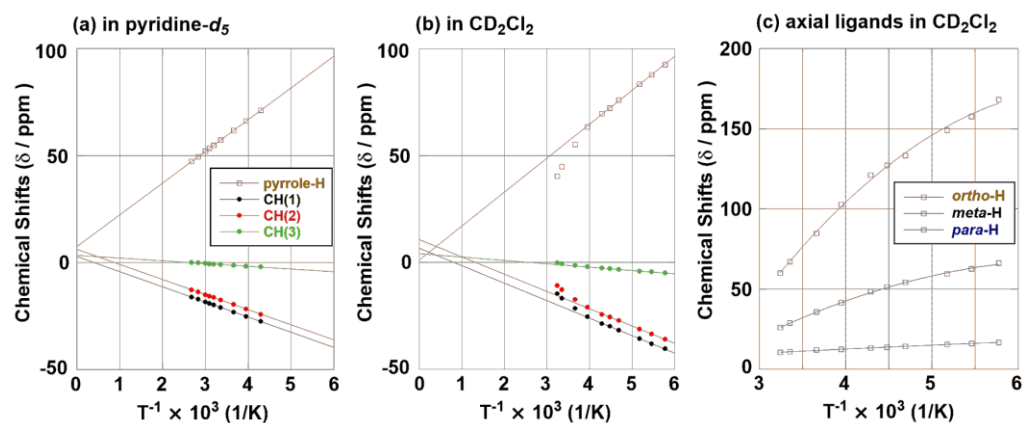


Figure 1-10. Curie plots of some pyrrocorphin signals in **4Ni** taken in (a) pyridine-*d*₅ and (b) CD₂Cl₂. Curie plots of the axially coordinating pyridine ligands taken in CD₂Cl₂ are given in (c).

sample of pure **4Ni**·**2Py** was dissolved in these solvents and the chemical shifts were measured at various temperatures, which were then plotted against 1/T. As shown in Figure 1-10(a), Curie plots of the paramagnetically shifted signals such as those of pyrrole proton and CH exhibited good linearity. In contrast, Curie plots of the same signals taken in CD₂Cl₂ solution gave curved lines as shown in Figure 1-10(b). Figure 1-10(c) shows Curie plots of the axially coordinating pyridine ligand. The *ortho* and *meta* proton signals of the pyridine ring appeared extremely downfield with extensive curvature. In contrast, the downfield shift of the *para* proton signal was quite small and the Curie line showed a good linearity.

Figure 1-11 shows titration curves of the pyrrole proton signal obtained by the addition of pyridine to the toluene-*d*₈ solution of **4Ni** at four different temperatures. The pyrrole proton signal observed at 7.65 ppm at 298 K shifted downfield upon addition of pyridine. The signal reached the constant value, ca. 57 ppm, after the addition of 10 molar equiv of pyridine relative to **4Ni**. A similar tendency was observed at higher temperature although the constant values decreased to

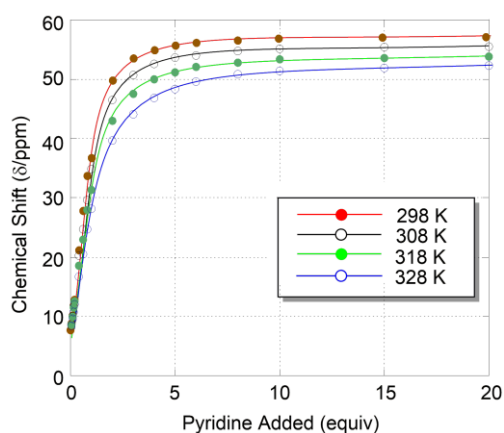
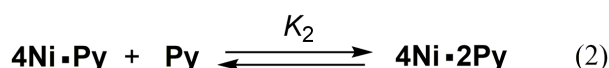
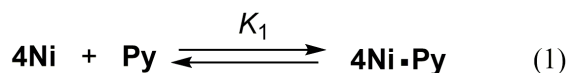


Figure 1-11. Titration curves of the pyrrole proton signal of **4Ni** taken at various temperatures in toluene-*d*₈.

55.4, 53.8, and 52.3 ppm at 308, 318, and 328 K, respectively. The results suggest that **4Ni** was converted to **4Ni•Py** and then to **4Ni•2Py** upon addition of pyridine according to Eqs (1) and (2) in Scheme 1-3, where K_1 and K_2 are binding constants corresponding to Eqs (1) and (2), respectively.



Scheme 1-3. Formation of **4Ni•Py** and **4Ni•2Py** upon addition of pyridine (Py) to four-coordinate **4Ni** in a toluene solution.

1.3.5 UV-Visible Spectra

Figure 1-12 shows the UV-Visible spectrum of four-coordinate **4Ni** complex taken in (a) CH_2Cl_2 and (b) pyridine solutions. For comparison, the UV-Visible spectra of analogous **1Ni** – **3Ni** were also included. As reported by Herges and co-workers, these complexes were converted to pyridine

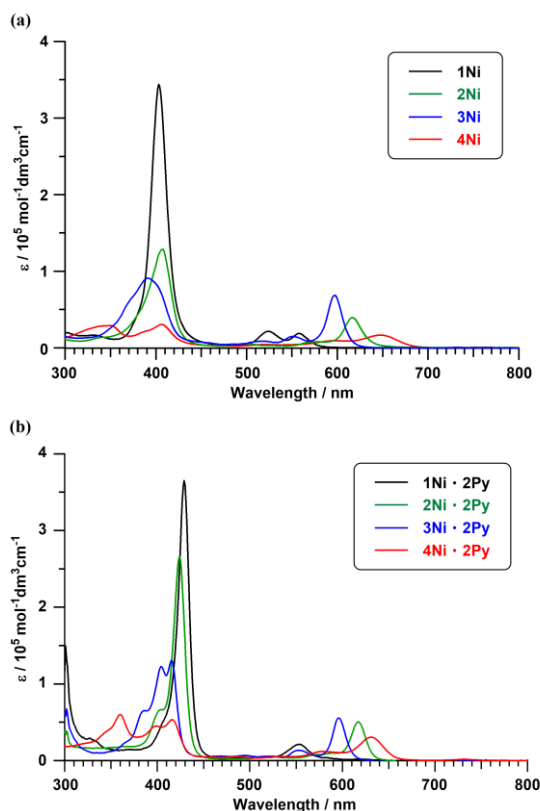


Figure 1-12. UV-Visible spectra of **1Ni**–**4Ni** taken in (a) CH_2Cl_2 and (b) pyridine.

ligated six-coordinate complexes in the presence of large excess of pyridine. Thus, the UV-Visible spectra shown in Figure 12(b) correspond to those of **1Ni·2Py–4Ni·2Py**. The extinction coefficients of the Soret bands decreased on the reduction of the porphyrin ring in both CH₂Cl₂ and pyridine solutions. The absorption maxima of the major bands in these complexes are listed in Table 1-5. The most bathochromic absorption bands (Q bands) in four- and six-coordinate complexes were observed in pyrrocorphin complexes at 647 in **4Ni** and 631 nm in **4Ni·2Py**.

Figure 1-13 (a) shows UV-Visible spectral change observed when a small amount of pyridine was added step by step up to 1030 equiv to the toluene solution of **4Ni** at ambient temperature. A clear isosbestic point was observed at 655 nm as shown in Figure 1-13(b) when pyridine solution was added up to 9.0 equiv.

Table 1-5. UV-Visible spectral data of four-coordinate and pyridine ligated six-coordinate complexes taken in CH₂Cl₂ and pyridine.

| Complexes | Solvent | Solet bands, λ_{\max} nm (log ϵ) | Q bands |
|-------------------------|---------------------------------|--|------------------------------------|
| 1Ni ^a | CH ₂ Cl ₂ | 403 (5.54) | 524 (4.33), 558 (4.26) |
| 2Ni ^a | CH ₂ Cl ₂ | 407 (5.11) | 497 (3.74), 576 (3.93), 613 (3.90) |
| 3Ni ^a | CH ₂ Cl ₂ | 391 (4.96) | 517 (3.94), 551 (4.17), 597 (4.83) |
| 4Ni | CH ₂ Cl ₂ | 349 (4.46), 406 (4.48) | 519 (3.63), 598 (3.98), 647 (4.22) |
| 1Ni·2Py | Pyridine | 429 (5.56) | 554 (4.32) |
| 2Ni·2Py | Pyridine | 424 (5.43) | 521 (3.74), 617 (4.70) |
| 3Ni·2Py | Pyridine | 404 (5.09), 415 (5.12) | 522 (4.12), 596 (4.74) |
| 4Ni·2Py | Pyridine | 360 (4.78), 399 (4.73), 416 (4.73) | 579 (4.07), 631 (4.48) |

^a Originally reported by Herges and co-workers in CH₃CN solution [27].

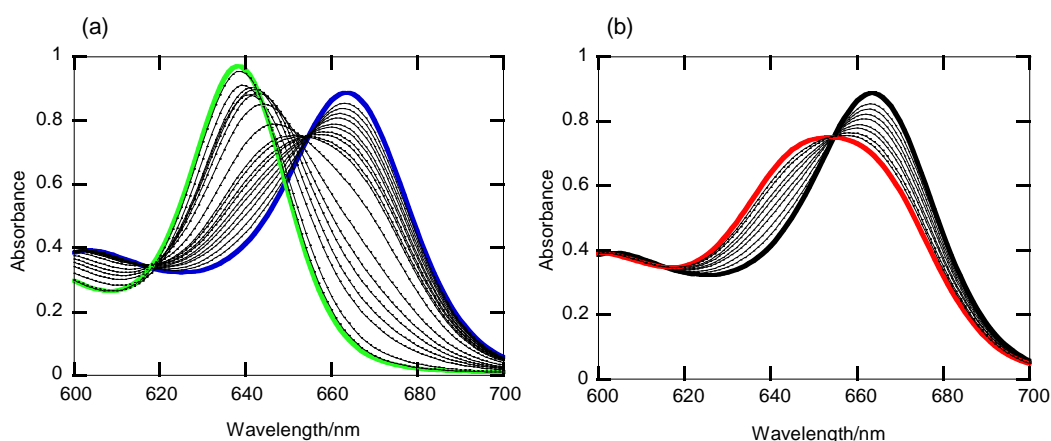


Figure 1-13. UV-Visible spectral changes of Q bands upon the addition of (a) 0 – 1027 equiv and (b) 0 – 9 equiv of pyridine to the toluene solution of **4Ni** (3.99×10^{-5} mol/L) at ambient temperature. Spectra for pure **4Ni** and **4Ni·2Py** are given by blue and green lines in (a) and the spectrum drawn by red line in (b) represents the one obtained by the addition of 9.0 equiv of pyridine.

1.4 Discussion

1.4.1 Electronic Structures of Ni(II) Pyrrocorphin Complexes

One of the most characteristic features in four-coordinate Ni(II) pyrrocorphin **4Ni** is a very low oxidation potential, *i.e.* $E_{1/2} = 0.40$ V, as compared with the oxidation potentials of analogous **1Ni**–**3Ni**. The data in Table 1-3 indicate that both the 1st and the 2nd oxidation potentials exhibit negative shift as the reduction of porphyrin ring proceeds. The largest decrease in oxidation potential was observed when isobacteriochlorin ring was reduced to pyrrocorphin ring; the differences in oxidation potentials reached as much as 0.42 V for the 1st and 0.44 V for the 2nd oxidation potentials. In contrast, the 1st reduction potentials are not much different among four complexes. Consequently, the HOMO–LUMO gap in **4Ni** is the smallest among the four complexes examined in this study. Figure 1-14 shows the plots of the 1st oxidation and reduction potentials against the number of the reduced double bonds, which clearly indicates that the reduction of porphyrin ring narrows the HOMO–LUMO gap. Thus, **4Ni** has the smallest HOMO–LUMO gap, which should correspond to the most bathochromic band at 647 nm.

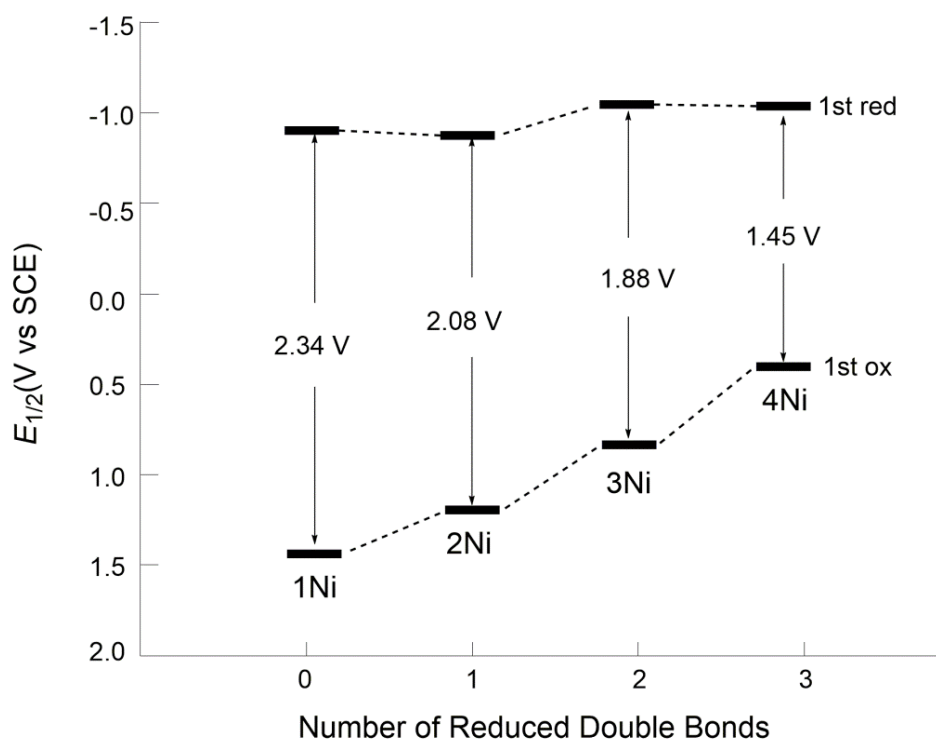


Figure 1-14. Relationship between 1st $E_{1/2}$ for oxidation and reduction and the number of the double bonds reduced. The HOMO–LUMO gap for each complex is also given.

Figure 1-15 shows the frontier orbitals determined by time-dependent (TD) DFT calculations at the B3LYP/6-31G(d) level. The absorption at 615 nm (Q band) was assigned to a transition from HOMO to LUMO and the one at 382 nm (Soret band) was ascribed to an overlapped absorption from HOMO-1 to LUMO and from HOMO to LUMO+1. As shown in Figure 1-16, the calculated absorption bands corresponding to these transitions were 607 and 377 nm, respectively.

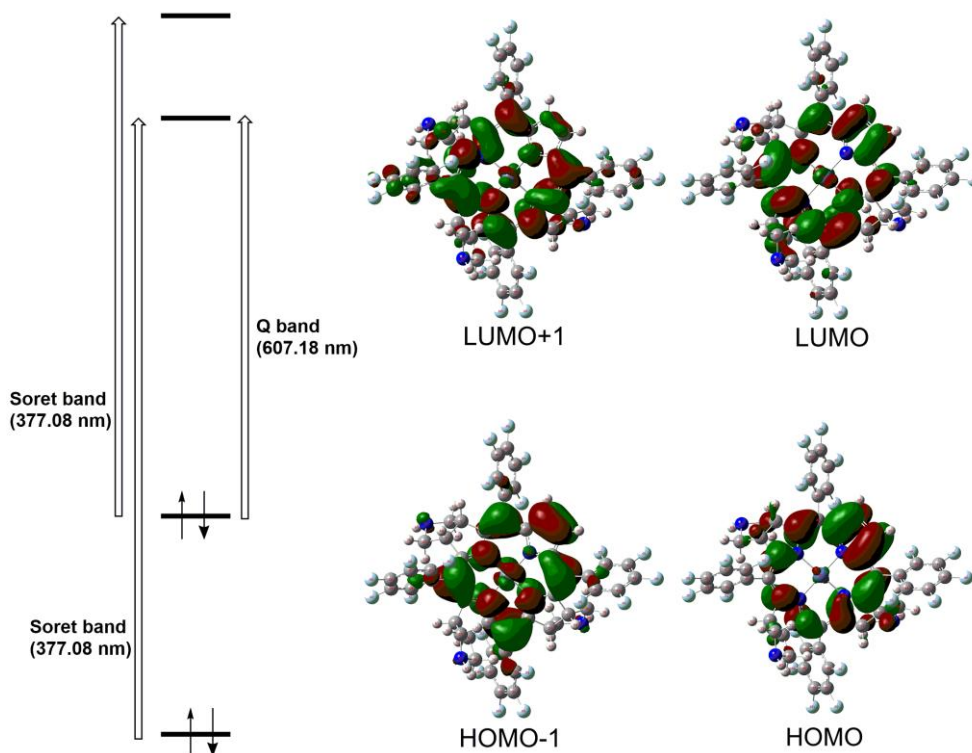


Figure 1-15. TD DFT calculation of Ni(II) Pyrrocorphin **4Ni** for the assignments of absorption bands at the B3LYP/6-31G(d) level.

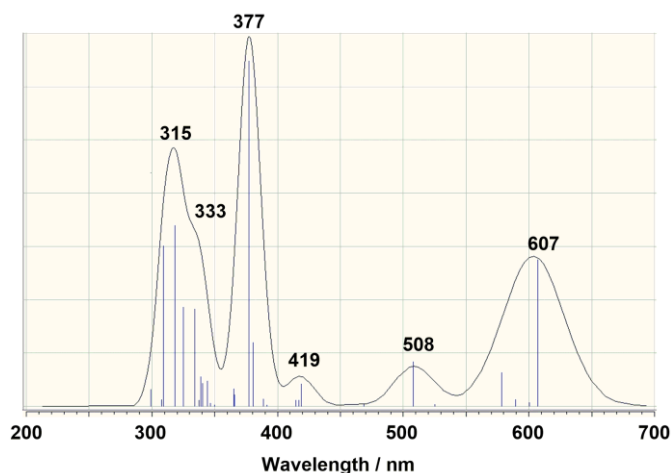


Figure 1-16. Calculated spectrum of **4Ni** by the TD-DFT method at the B3LYP/6-31G(d) level.

surprisingly, when the powder sample of the four-coordinate **4Ni** was measured by the SQUID magnetometry, it exhibited the obvious paramagnetism as shown in Figure 1-17. The observed effective magnetic moment (black circle) was $2.10 \pm 0.02 \mu_B$ between 300 and 30 K, which is a little higher than the spin-only value for a pure $S = 1/2$ state, *i.e.* $\mu_{\text{eff}} = 1.73 \mu_B$. Although the effective magnetic moment value of paramagnetic metal ion or free radical with a spin state of $S = 1/2$ is nearly temperature-independent in the range 2 - 300 K, the four-coordinate **4Ni** showed a drop of effective magnetic moment value below 30 K, reached a value of $1.01 \mu_B$ at 2.0 K. This drop is ascribed to the zero-field splitting because the solid sample may form a dimer as shown in Scheme 1-5. The recalculated effective magnetic moment was maintained at $2.97 \pm 0.03 \mu_B$ between 300 and 30 K, decreases to a value of $1.42 \mu_B$ at 2.0 K. Thus, One of two Ni(II) ions in a dimer is a diamagnetic $S = 0$ state, and the other is a paramagnetic $S = 1$ state, either Ni(II) ion center axially coordinates to *N*-methyl-pyrrolidine unit or not coordinate. The solid line of blue in Figure 1-17 represents a spin-Hamiltonian simulation with a zero-field splitting of $D = +12.1 \text{ cm}^{-1}$ and $g_{\text{mean}} = 2.22$. In comparison with the zero-field splitting value ($D = +4.41 \text{ cm}^{-1}$) of six-coordinate Ni(II) pyrrocorphin **4Ni•2Py**, the higher value for solid sample of **4Ni** indicates the symmetry lowering of the estimated structure.

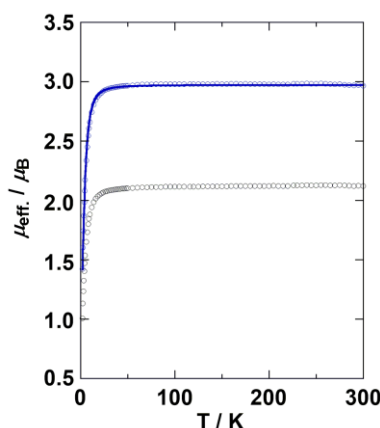
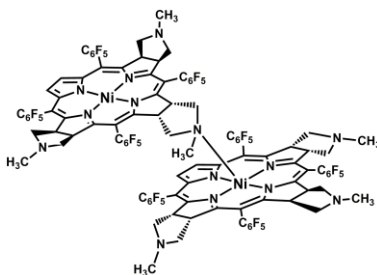


Figure 1-17. Temperature dependence of the effective magnetic moments (black circle) of **4Ni** taken for the microcrystalline sample by SQUID magnetometry. The effective magnetic moments (blue circle) recalculated as a dimer structure in Scheme 1-5. The solid line in blue represents a simulation with a zero-field splitting of $D = +12.1 \text{ cm}^{-1}$, $S = 1$, and $g_{\text{mean}} = 2.22$.



Scheme 1-5. The estimated dimer structure of **4Ni** in solid states.

To understanding the dimerization of **4Ni** in solid state, the four-coordinate **2Ni** was also confirmed by X-ray crystal structure analysis and SQUID measurement. Single crystal of **2Ni** was obtained by recrystallization from CHCl_3 / *n*-hexane solution. Figure 1-18 shows the ORTEP diagram of polymerized **2Ni** together with the atom labeling at 100K, which formed the one-dimensional chain. The same crystal structure was already reported by Herges et al., but bond length, planarity, and dihedral angle in macrocycles have not made a detailed research [27]. The bond length of the axially coordinated *N*-methyl-pyrrolidine nitrogen to the nickel atom Ni-N_{ax} is 2.181(5) Å, while the average bond length of chlorin nitrogen to the nickel atom Ni-N_{eq} is 2.052(5) Å. The Ni(II) ion is located in a distorted square-pyramidal coordination geometry (five-coordinate) and is displaced from the C_{20}N_4 least-square plane by 0.284 Å toward the axially coordinated *N*-methyl-pyrrolidine nitrogen atom. Figure 1-19 shows perpendicular displacement of the peripheral carbon (black) and nitrogen (blue) atoms from the C_{20}N_4 least-square plane. The maximum deviations among pyrrole β-carbon and *meso*-carbon atoms from the average porphyrin plane were 0.303 and 0.108 Å, respectively. In addition, the RMS value of the macrocycle ring and the maximum torsion angle between the four macrocycle nitrogen atoms in polymerized **2Ni** were 0.135 and 2.499, respectively. The dihedral angle between the macrocycle plane and one of the neighboring molecule was 63.3°. Therefore, because four-coordinate Ni(II) chlorin **2Ni** would be more planar than pyrrocorphin **4Ni** the same as the correlation between the macrocycle ring distortion of the six-coordinate Ni(II) chlorin **2Ni** and pyrrocorphin **4Ni**·**2Py**, **2Ni** in solid state

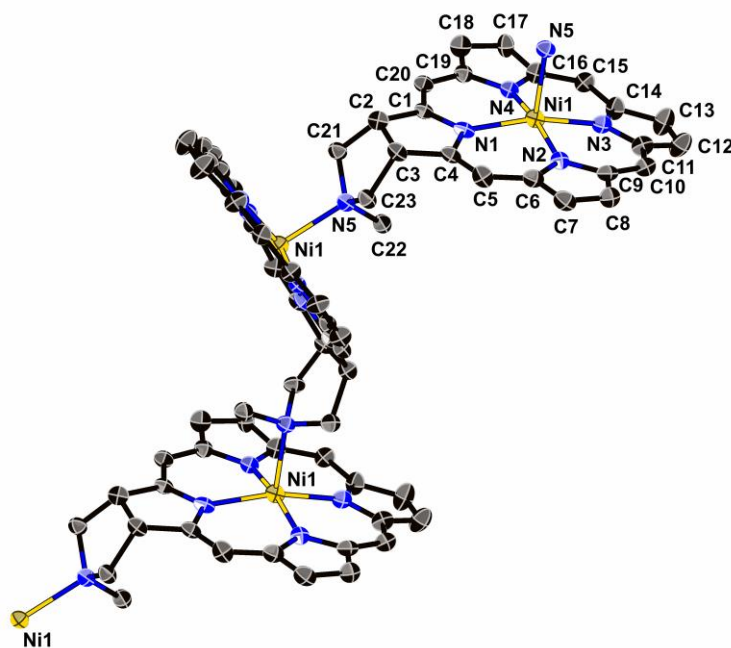


Figure 1-18. ORTEP drawings of polymerized **2Ni** at 100 K with the 50% probability thermal ellipsoids and atom labeling. Hydrogen, solvent, and *meso*-pentafluorophenyl group ($-\text{C}_6\text{F}_5$) atoms are omitted for clarity.

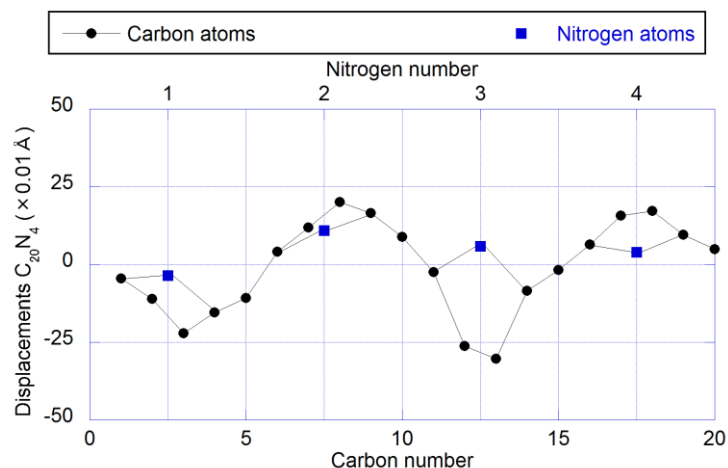


Figure 1-19. Perpendicular displacements of the peripheral carbon (black) and nitrogen (blue) atoms from the least-square plane ($C_{20}N_4$) in polymerized **2Ni**. Atom numbers corresponding to the ones in Figure 1-18.

formed the polymerized structure. On the other hand, **4Ni** in solid state might constituted a dimer structure because of high steric hindrance. As shown in Figure 1-20, the effective magnetic moment μ_{eff} was $2.86 \mu_B$ at 300 K, and this corresponds to the spin only value, $2.83 \mu_B$, for the $S = 1$ state. When decreasing the temperature, the μ_{eff} value is almost constant ($2.80 \mu_B$ at 30 K), but it drops below 20 K to a minimum ($1.15 \mu_B$ at 2 K). This drop must be due to the local zero-field splitting and/or the exchange interaction between Ni(II) ions. In the χ vs. T plot, no maximum due to the antiferromagnetic interaction was observed. Since the exchange interaction seems to be weak, the data was analyzed based on the mononuclear model considering the zero-field splitting, and the exchange interaction was introduced by the molecular field approximation.

$$\chi_z = \frac{N g_z^2 \beta^2}{k T} \frac{\exp(-D/k T)}{1 + 2 \exp(-D/k T)} + \text{TIP}$$

$$\chi_x = \frac{N g_x^2 \beta^2}{D} \frac{1 - \exp(-D/k T)}{1 + 2 \exp(-D/k T)} + \text{TIP}$$

$$\chi_A' = \frac{\chi_z + 2 \chi_x}{3}$$

$$\chi_A = \frac{\chi_A'}{1 - n J (\chi_A' / N g^2 \beta^2)}$$

In the equations, D is the axial zero-splitting parameter, TIP is the temperature independent paramagnetism, n is the number of the nearest neighbors ($n = 2$), and J is the exchange interaction parameter. The best fitting parameters were $g_z = g_x = 2.02 \text{ cm}^{-1}$, $D = +17.2 \text{ cm}^{-1}$, $J = +0.02 \text{ cm}^{-1}$, and $\text{TIP} = 0 \text{ cm}^3 \text{ mol}^{-1}$, with good discrepancy factors $R(\chi_A) = 1.2 \times 10^{-5}$ and $R(\mu_{\text{eff}}) = 3.7 \times 10^{-6}$. Further analyses considering the g -anisotropy could not be done. The positive D value is reasonable for the present nickel(II) complex, whose equatorial ligand field is strong[41].

Consequently, the drop in μ_{eff} below 20 K is mainly due to the zero-field splitting, and the exchange interactions between nickel(II) ions are very weak. These results indicated that the four-coordinate Ni(II) porphyrinoid complexes with *N*-methyl-pyrrolidine units exhibited the difference coordination behavior between solution and solid states, and the five-coordinate Ni(II) chlorin **2Ni** and pyrrocorphin **4Ni** in solid state were a paramagnetic $S = 1$ state per a Ni(II) ion.

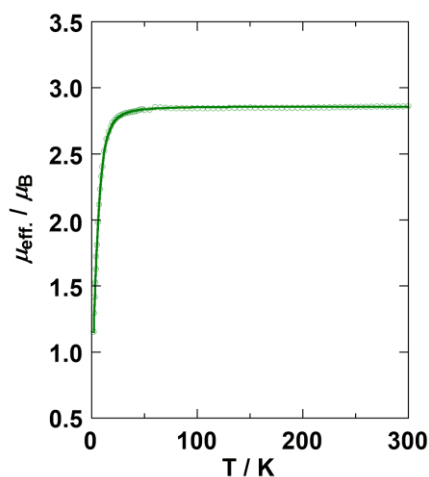


Figure 1-20. Temperature dependence of the effective magnetic moments (green circle) per a Ni(II) chlorin complex of **2Ni** taken for the microcrystalline sample by SQUID magnetometry. The solid line in green represents a simulation with a zero-field splitting of $D = +17.2 \text{ cm}^{-1}$, $S = 1$, $g_{\text{mean}} = 2.02$, and $J = +0.02$

1.4.2 Binding Constants of Ni(II) Pyrrocorphin toward Pyridine Ligand

Ni(II) porphyrinoids can bind one or two ligands to form five- or six-coordinate complexes. Stepwise coordination of pyridine ligand to the Ni(II) ion was clearly seen in the titration experiment monitored by UV-Visible spectroscopy as shown in Figure 1-13(a). Close inspection of the figure has revealed that the titration spectra include isosbestic points if the amount of pyridine ligand added is less than 9 molar equivalents relative to **4Ni** as shown in Figure 1-13(b). The result indicates that Eq. (1) in Scheme 1-3 is the only process occurring under this condition. The absorbance of the observed spectrum (A_{obs}) at each wavelength in Figure 1-13(b) is expressed by Eq. (3), where A_0 and A_1 are the

$$A_{\text{obs}} = A_0(1-\alpha) + A_1\alpha \quad (3)$$

absorbances of **4Ni** and **4Ni•Py**, respectively, and α is a molar fraction of **4Ni•Py**. In order to determine the binding constant (K_1), one has to know the UV-Visible spectrum of pure five-coordinate **4Ni•Py**. Thus, the absorbance $A_0(1-\alpha)$ was subtracted from A_{obs} at each wavelength, which was then multiplied by α^{-1} . Molar fraction α was determined under the following assumptions: (i) the maximum absorption of the Q band in **4Ni•Py** is less than that of **4Ni•2Py** on the basis of the titration curves in Figure 1-14(a), and (ii) the absorption band should have no

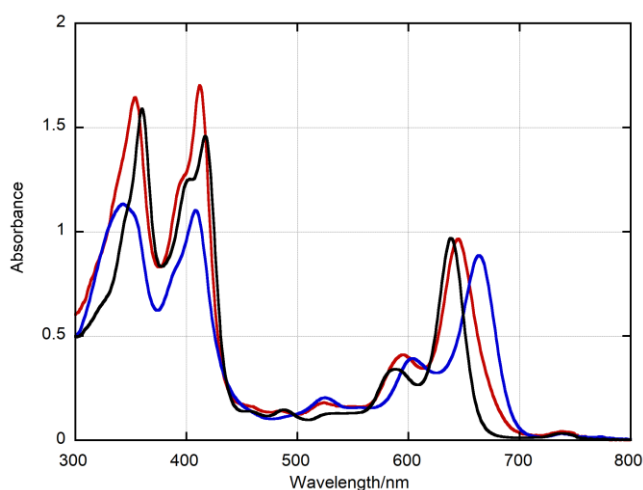


Figure 1-21. UV-Visible spectra of **4Ni** (blue) and **4Ni•2Py** (black) taken in a toluene solution at ambient temperature. The spectrum of **4Ni•Py** (red) calculated under assumptions mentioned in the text.

shoulder at 663 nm, which is the λ_{max} of **4Ni** in toluene solution. The α values that satisfy the above-mentioned conditions were in the range of 0.4 – 0.5. Figure 1-21 shows the UV-Visible spectrum of **4Ni•Py** with a molar fraction $\alpha = 0.45$ together with those of **4Ni** and **4Ni•2Py**. Binding constant corresponding to Eq (1) in Scheme 1-3 was obtained by the plots of $\alpha/(1-\alpha)$ against free pyridine concentration [Py], which yielded the K_1 value of $1900 \pm 300 \text{ L mol}^{-1}$ for $\alpha = 0.4 - 0.5$. Binding constant K_1 was similarly obtained on the basis of the ^1H NMR chemical shifts of the pyrrole proton signals. In contrast to the case of UV-Visible spectroscopy, no stepwise change was observed in the titration curve as shown in Figure 1-13. The result indicates that the chemical shift of the pyrrole proton signal in **4Ni•Py** is similar to that in **4Ni•2Py**, ca. 57 ppm at ambient temperature. This is understandable because both **4Ni•Py** and **4Ni•2Py** adopt high-spin ($S = 1$) state; the unpaired electron in the $d_{x^2-y^2}$ orbital should induce a similar downfield shift to the pyrrole proton signals. The $[\text{4Ni•Py}]/[\text{4Ni}]$ values were plotted against free [Py] in the range of 0 – 5 eq of pyridine to yield $K_1 = 1780 \text{ L mol}^{-1}$.

Because of the lack of the isosbestic points corresponding to Eq. (2), K_2 was determined by the simulation method. As mentioned, the UV-Visible spectra consist of three components, **4Ni**, **4Ni•Py**, and **4Ni•2Py**, if the addition of pyridine ligand exceeds 9 equiv. The absorbance of the observed spectrum at each wavelength should be expressed by Eq. (4), where A_0 , A_1 , and A_2 are the absorbances of **4Ni**, **4Ni•Py**, and **4Ni•2Py**, respectively, and α , β , and γ are the corresponding

$$A_{\text{obs}} = A_0\alpha + A_1\beta + A_2\gamma \quad (4)$$

molar fractions. The UV-Visible spectra obtained by the addition of 15, 19, 23, 27, and 30 eq of pyridine were simulated by changing the molar fractions of three components. The ratios $[\text{4Ni•2Py}]/[\text{4Ni•Py}]$ were plotted against free [Py] to yield $K_2 = 590 \text{ L mol}^{-1}$. The K_1 and K_2

values of **4Ni** are listed in Table 1-6 together with those of analogous **1Ni**, **2Ni**, and **3Ni** reported by Herges and co-workers [27]. It is clear that the binding constant increases as the reduction of porphyrin ring proceeds.

Table 1-6. Binding constants K_1 and K_2 determined in a toluene solution at 298 K.

| Complexes | K_1 (L mol ⁻¹) | K_2 (L mol ⁻¹) | $\beta_2 = K_1 K_2$ (L ² mol ⁻²) | Ref. |
|------------|--|------------------------------|---|-----------|
| 1Ni | 7.8 ^a | 20.5 ^a | 1.6×10^2 | 27 |
| 2Ni | 91.1 ^a | 43.4 ^a | 4.0×10^3 | 27 |
| 3Ni | 441.0 ^a | 77.5 ^a | 3.4×10^4 | 27 |
| 4Ni | 1780 ^a 1900 ^b | 590 ^b | 1.0×10^6 | This work |

^aDetermined by ¹H NMR spectroscopy. ^bDetermined by UV-Visible spectroscopy.

In order to confirm the strong affinity of **4Ni** for axial ligand binding, I have examined the competitive ligation of **4Ni** and **2Ni** toward pyridine. In each time after the addition of a certain amount of pyridine to the CD₂Cl₂ of **2Ni** and **4Ni**, the ratios $[4Ni \cdot Py]/[4Ni]$ and $[2Ni \cdot Py]/[2Ni]$ were determined on the basis of the chemical shifts of the pyrrole proton signals; CD₂Cl₂ was used as a solvent instead of toluene-d₈ since the toluene signals overlapped with pyrrole signals. Figure 1-22 shows the plots of $[4Ni \cdot Py]/[4Ni]$ and $[2Ni \cdot Py]/[2Ni]$ against [Py]. Since [Py] is less than 0.0085 equiv (1.5×10^{-4} mol/L) relative to **2Ni** and **4Ni**, the concentrations of bis-adducts **4Ni·2Py** and **2Ni·2Py** should be negligibly small. Thus, the ratio of the slopes, which was estimated to be 10.4, corresponds to the ratio of equilibrium constants, $K_1(\text{pyr})/K_1(\text{chl})$. Although the ratio is much smaller than the corresponding ratio in toluene-d₈ solution, *i.e.* $K_1(\text{pyr})/K_1(\text{chl}) = 19.5$, probably due to the solvent effect, the result clearly indicates that the binding ability of Ni(II) porphyrin complexes increases as the reduction of the porphyrin ring proceeds.

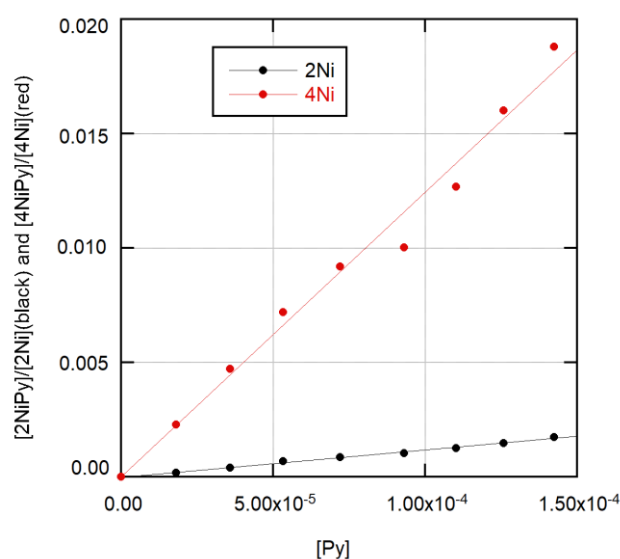


Figure 1-22. Competitive ligation of pyridine toward **2Ni** and **4Ni** complexes. Slopes of the lines indicate the binding constants (K_1).

Let us now consider the reasons for high binding ability of **4Ni** as compared with less reduced complexes such as **1Ni** – **3Ni**; the binding ability toward pyridine ligand is **1Ni** < **2Ni** < **3Ni** < **4Ni**. The structural data listed in Table 1-2 indicates that the averaged Ni–N(porphyrin) length increases as the reduction of the porphyrin ring proceeds. The results indicate that the electron density on Ni(II) ion decreases as the reduction of the porphyrin ring proceeds. Consequently, Ni–N(pyridine) bonds are strengthened in highly reduced complexes, which is verified by the shortest Ni–N(pyridine) bonds in **4Ni•2Py**.

1.5 Conclusion

Four-coordinate Ni(II) complex of pyrrolidine-fused pyrrocorphin **4Ni** was prepared by successive 1,3-dipolar cycloaddition reactions of an azomethine ylide to 5,10,15,20-tetrakis(pentafluorophenyl)porphyrin. The addition of excess pyridine to **4Ni** in toluene solution yielded mono-pyridine complex **4Ni•Py**, which was then converted completely to bis-pyridine complex **4Ni•2Py**. The first oxidation potentials of four-coordinate Ni(II) complexes determined by CV in CH₂Cl₂ solution were quite different; they showed a large decrease as the reduction of the porphyrin ring proceeds. In contrast, the first reduction potentials were not so sensitive to the difference in porphyrin structure. Consequently, the HOMO–LUMO gap (ΔE) was the smallest in **4Ni**, 1.45 V, as compared with **1Ni** (2.34 V), **2Ni** (2.08 V), and **3Ni** (1.88 V). The result was further verified by UV-Vis spectroscopy and DFT calculation. SQUID magnetometry for the microcrystalline sample revealed that **4Ni•2Py** was paramagnetic with $S = 1$ spin state between 2 and 300 K. Correspondingly, ¹H NMR spectrum showed the pyrrole and pyrrolidine β -proton signals extremely downfield and upfield positions, respectively, supporting the presence of unpaired electrons. Close inspection of the chemical shifts suggested that the spin densities on pyrrocorphin α -carbon and nitrogen atoms are quite different as is revealed from the large difference in chemical shifts of the pyrrolidine β -proton signals at –21.0, –17.5, and –0.93 ppm. UV-Vis and NMR titration experiments have shown that the binding constant of pyridine to **4Ni** is ca. 4 times as large as that of **3Ni**. The difference was ascribed to the fact that **4Ni** has longer a Ni–N(porphyrin) length than the other three complexes. Thus, the pyridine ligand prefers the electron deficient Ni(II) in **4Ni**, resulting in the larger binding constant as compared with other three complexes.

1.6 References

- [1] *The porphyrin hand book* (Eds.: K. M. Kadish, K. M. Smith, R. Guillard), Academic Press, San Diego, 2000.
- [2] *Hand book of porphyrin science* (Eds.: K. M. Kadish, K. M. Smith, R. Guillard), World Scientific, Singapore, 2010.
- [3] K. Nakamura, A. Ikezaki, Y. Ohgo, T. Ikeue, S. Neya, M. Nakamura, *Inorg. Chem.* 2008, 47, 10299–10307.
- [4] T. Ikeue, S. Kurahashi, M. Handa, T. Sugimori, M. Nakamura, *J. Porphyrins Phthalocyanines* 2008, 12, 1041–1049.
- [5] R. Bonnett, *Chemical Aspects of Photodynamic Therapy*, Gordon and Breach Science Publishers, Australia, 2000.
- [6] E. D. Sternberg, D. Dolphin, C. Brückner, *Tetrahedron* 1998, 54, 4151–4202.
- [7] M. Obata, S. Hirohara, R. Tanaka, I. Kinoshita, K. Ohkubo, S. Fukuzumi, M. Tanihara, S. Yano, *J. Med. Chem.* 2009, 52, 2747–2753.
- [8] A. Ikezaki, J. Ono, Y. Ohgo, M. Fukagawa, T. Ikeue, M. Nakamura, *J. Porphyrins Phthalocyanines* 2014, 18, 778–791.
- [9] A. C. Tomé, P. S. S. Lacerda, M. G. P. M. S. Neves, J. A. S. Cavaleiro, *Chem. Commun.* 1997, 1199–1200.
- [10] M. Gałężowski, D. T. Gryko, *J. Org. Chem.* 2006, 71, 5942–5950.
- [11] F. –P. Montforts, B. Gerlach, F. Höper, *Chem. Rev.* 1994, 94, 327–347.
- [12] R. J. Abraham, C. J. Medforth, K. M. Smith, D. A. Goff, D. J. Simpson, *J. Am. Chem. Soc.* 1987, 109, 4786–4791.
- [13] M. Taniguchi, J. S. Lindsey, *Chem. Rev.* 2017, 117, 344–535.
- [14] S. W. Ragsdale, *Met. Ions Life Sci.* 2014, 14, 125–145.
- [15] R. K. Thauer, *Microbiology* 1998, 144, 2377–2406.
- [16] M. Krüger, A. Meyerdierks, F. O. Glöckner, R. Amann, F. Widdel, M. Kube, R. Reinhardt, J. Kahnt, R. Böcher, R. K. Thauer, S. Shima, *Nature* 2003, 426, 878–881.
- [17] K. Zheng, P. D. Ngo, V. L. Owens, X. Yang, S. O. Mansoorabadi, *Science* 2016, 354, 339–342.
- [18] M. J. Murphy, L. M. Siegel, S. R. Tove, H. Kamin, *Proc. Nat. Acad. Sci. USA* 1974, 71, 612–616.
- [19] D. Thomas, Y. Surdin-Kerjan, *Microbiol. Mol. Biol. Rev.* 1997, 61, 503–532.
- [20] A. Eschenmoser, *Angew. Chem. Int. Ed.* 50 (2011) 12412–12472.
- [21] J. –H. Martens, H. Barg, M. J. Warren, D. Jahn, *Appl. Microbiol. Biotechnol.* 58 (2002) 275–285.
- [22] M. J. Warren, N. J. Stolowich, P. J. Santander, C. A. Roessner, B. A. Sowa, A. I. Scott, *FEBS Lett.* 261 (1990) 76–80.
- [23] I. U. Heinemann, M. Jahn, Dieter Jahn, *Arch. Biochem. Biophys.* 2008, 474, 238–251.
- [24] B. C. Tripathy, I. Sherameti, R. Oelmüller, *Plant Signal Behav.* 2010, 5, 14–20.

- [25] C. Kratky, R. Waditschatka, C. Angst, J. E. Johansen, J. C. Plaquevent, J. Schreiber, A. Eschenmoser, *Helv. Chim. Acta* 1985, 68, 1312–1337.
- [26] A. M. G. Silva, A. C. Tomé, M. G. P. M. S. Neves, A. M. S. Silva, J. A. S. Cavaleiro, *J. Org. Chem.* 2005, 70, 2306–2314.
- [27] M. Dommaschk, V. Thoms, C. Schütt, C. Näther, R. Puttreddy, K. Rissanen, R. Herges, *Inorg. Chem.* 2015, 54, 9390–9392.
- [28] S. Stoll, A. Schweiger, *J. Magn. Reson.* 2006, 178, 42–55.
- [29] A. M. G. Silva, A. C. Tomé, M. G. P. M. S. Neves, A. M. S. Silva, J. A. S. Cavaleiro, *Chem. Commun.* 1999, 1767–1768.
- [30] L. Palatinus, G. Chapuis, *J. Appl. Cryst.* 2007, 40, 786–790.
- [31] *CrystalStructure Ver. 4.1: Crystal structure analysis package*, Rigaku, Tokyo, Japan and Rigaku/MSO (The Woodlands, TX, USA), 2014.
- [32] G. M. Sheldrick, *Acta Cryst.* 2015, A71, 3–8.
- [33] A.L. Spek, *Acta Cryst.* 2015, C71, 9–18.
- [34] *Gaussian 09, Revision D.01*, M. J. Frisch, G. W. Trucks, H. B. Schlegel, G. E. Scuseria, M. A. Robb, J. R. Cheeseman, G. Scalmani, V. Barone, B. Mennucci, G. A. Petersson, H. Nakatsuji, M. Caricato, X. Li, H. P. Hratchian, A. F. Izmaylov, J. Bloino, G. Zheng, J. L. Sonnenberg, M. Hada, M. Ehara, K. Toyota, R. Fukuda, J. Hasegawa, M. Ishida, T. Nakajima, Y. Honda, O. Kitao, H. Nakai, T. Vreven, J. A. Montgomery, Jr., J. E. Peralta, F. Ogliaro, M. Bearpark, J. J. Heyd, E. Brothers, K. N. Kudin, V. N. Staroverov, R. Kobayashi, J. Normand, K. Raghavachari, A. Rendell, J. C. Burant, S. S. Iyengar, J. Tomasi, M. Cossi, N. Rega, J. M. Millam, M. Klene, J. E. Knox, J. B. Cross, V. Bakken, C. Adamo, J. Jaramillo, R. Gomperts, R. E. Stratmann, O. Yazyev, A. J. Austin, R. Cammi, C. Pomelli, J. W. Ochterski, R. L. Martin, K. Morokuma, V. G. Zakrzewski, G. A. Voth, P. Salvador, J. J. Dannenberg, S. Dapprich, A. D. Daniels, Ö. Farkas, J. B. Foresman, J. V. Ortiz, J. Cioslowski, and D. J. Fox, Gaussian, Inc., Wallingford CT, 2009. 10.
- [35] A. D. Becke, *Phys. Rev. A* 1988, 38, 3098–3100.
- [36] C. Lee, W. Yang, R. G. Parr, *Phys. Rev. B* 1988, 37, 785–789.
- [37] M. Dolg, U. Wedig, H. Stoll, H. Preuss, *J. Chem. Phys.* 1987, 86, 866–872.
- [38] A. Eschenmoser, *Angew. Chem. Int. Ed.* 1988, 27, 5–39.
- [39] Y. Song, R. E. Haddad, S. –L. Jia, S. Hok, M. M. Olmstead, D. J. Nurco, N. E. Schore, J. Zhang, J. –G. Ma, K. M. Smith, S. Gazeau, J. Pécaut, J. –C. Marchon, C. J. Medforth, J. A. Shelnutt, *J. Am. Chem. Soc.* 2005, 127, 1179–1192.
- [40] C. Brückner, S. J. Rettig, D. Dolphin, *J. Org. Chem.* 1998, 63, 2094–2098.
- [41] R. Boča, *Coord. Chem. Rev.* 2004, 248, 757–815.

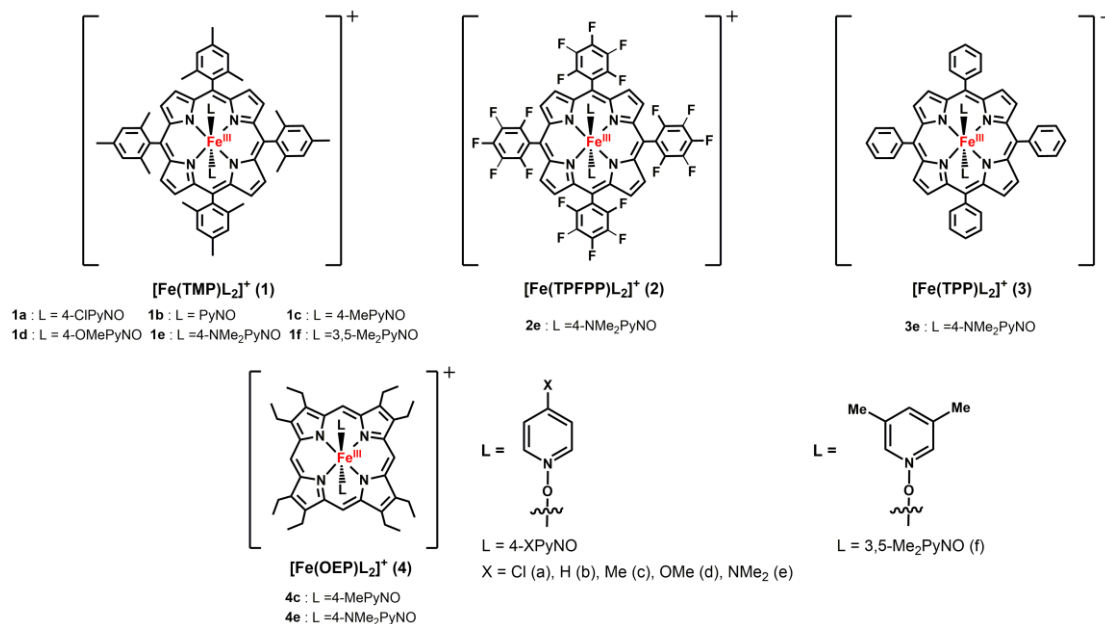
2 Spin-crossover Between High-spin ($S=5/2$) and Low-spin ($S=1/2$) States of Six-coordinate Iron(III) Porphyrins with Two Pyridine N-Oxide Derivatives

2.1 Introduction

Spin-crossover phenomenon in iron porphyrins has attracted much attention of chemists and biochemists who are working to reveal the functions and catalytic processes of heme proteins as well as their model complexes [1-5]. Some years ago, Ikeue et al. reported that the six-coordinated iron(III) porphyrins with suitably substituted pyridine as axial ligands exhibit a quite rare spin-crossover phenomenon between intermediate-spin ($S = 3/2$) and low-spin ($S = 1/2$) states if the porphyrin ring is highly deformed in a saddled fashion [6-10]. At that time the author considered that the process occurred only under very limited conditions. However, soon after this finding, the same spin-crossover process was observed in biological system. Rivera and co-workers reported on the basis of the ^{13}C NMR studies that the hydroxide complex of *Pseudomonas aeruginosa* heme oxygenase, which was considered to be a model for the elusive ferric hydroperoxide ($\text{Fe}^{\text{III}}\text{-OOH}$) intermediate in heme catabolism at ambient temperatures, led to the formation of three species and that the major species exhibited a spin crossover between $S = 3/2$ and $S = 1/2$ [11,12]. Since the population of two spin states should be dependent on temperature, pH, hydrogen bonding, etc. [13], the reactivity of the protein could be finely tuned by the change in microenvironment. This is one of the examples showing the importance of model studies to gain deeper insight into the enzymatic mechanisms in naturally occurring heme proteins.

As an extension of our work on seeking for the new spin-crossover system, the author have examined the electronic, magnetic, and structural properties of iron(III) *meso*-tetramesitylporphyrin cation complexes $[\text{Fe}(\text{TMP})\text{L}_2]^+$ (**1a-1e**), *meso*-tetra(perfluorophenyl)porphyrin cation complex $[\text{Fe}(\text{TPFPP})\text{L}_2]^+$ (**2e**), *meso*-tetraphenylporphyrin cation complex $[\text{Fe}(\text{TPP})\text{L}_2]^+$ (**3e**), and octaethylporphyrin cation complexes $[\text{Fe}(\text{OEP})\text{L}_2]^+$ (**4c** and **4e**) carrying *para*- or *meta*-substituted pyridine *N*-oxides ($\text{L} = 4\text{-XPyNO}$ or $3,5\text{-Me}_2\text{PyNO}$; $\text{X} = \text{Cl}, \text{H}, \text{Me}, \text{OMe}, \text{NMe}_2$) as axial ligands, where $\text{L} = 4\text{-ClPyNO}$ (**a**), PyNO (**b**), 4-MePyNO (**c**), 4-OMePyNO (**d**), $4\text{-NMe}_2\text{PyNO}$ (**e**), and $3,5\text{-Me}_2\text{PyNO}$ (**f**) (Scheme 2-1). The author has found that **2e** is the first example of six-coordinated iron(III) porphyrin that adopts the $S=1/2$ state in spite of the coordination of neutral oxygen ligands. Furthermore, some of these complexes have shown spin-crossover phenomenon between high spin ($S = 5/2$) and low spin ($S = 1/2$) states both in solution and in the solid. These are the new findings that greatly expand the

knowledge mentioned in our previous papers [14,15]. Therefore, the author will report the magnetic behaviors of **1a-1f**, **2e**, **3e**, **4c** and **4e** as studied by means of spectroscopic, magnetometric, and crystallographic methods.



Scheme 2-1. Structures of six-coordinate iron(III) porphyrin complexes bearing *para*- or *meta*- substituted pyridine *N*-oxides as axial ligands.

2.2 Experimental Section

2.2.1 Instrumentation

Elemental Analyses for carbon, hydrogen, and nitrogen were conducted using a Yanako CHN CORDER MT-6. UV-Vis absorption spectra were recorded in CHCl₃ solution on a Shimadzu UV-3100 spectrometer. ¹H and ¹⁹F NMR spectra were recorded on a JEOL delta ECX-500 spectrometer operating at 500.1 and 470.6 MHz for ¹H and ¹⁹F, respectively. Chemical shifts for ¹H NMR spectra were referenced to CH₂Cl₂ ($\delta = 5.32$ ppm for ¹H). Chemical shifts of ¹⁹F NMR spectra were referenced to hexafluorobenzene ($\delta = -164.9$ ppm). Mass spectra were recorded on a Bruker microTOF using positive mode ESI-TOF method for acetonitrile solutions by using sodium formate as reference. Unless otherwise noted, materials obtained from commercial suppliers were used without further purification. ESR spectra were recorded on a Bruker E500 spectrometer operating at the X band and equipped with an Oxford helium cryostat. The *g*-values were determined by the simulation of observed spectra. Iron 57 Mössbauer spectra were measured on a Wissel

Mössbauer spectrometer system. The samples were kept in a gas-flow cryostat and the $^{57}\text{Co}(\text{Rh})$ source was kept at room temperature. Isomer shifts (δ) are given relative to α -iron foil at room temperature. The solid-state magnetic susceptibilities were measured between 2 and 300 K under a magnetic field of 0.5 T with the SQUID magnetometers (Quantum Design MPMS-7 and MPMS-XL7). Solution magnetic moments were measured by the Evans method in CD_2Cl_2 solution using CH_2Cl_2 as the chemical shift reference [16]. The magnetic moments (μ^1_{eff}) were determined at various temperatures relative to that of high-spin $\text{Fe}(\text{TPP})\text{Cl}$ ($\mu^2_{\text{eff}} = 5.92 \mu_{\text{B}}$) according to $\mu^1_{\text{eff}} = (\Delta\nu^1 / \Delta\nu^2)^{1/2} \mu^2_{\text{eff}}$ [17].

2.2.2 Syntheses and Complex Data

2.2.2.1 Syntheses of free base porphyrinoids

The general synthetic procedures were carried out according to previous literatures [14]. Free base porphyrins such as $\text{H}_2(\text{TMP})$, $\text{H}_2(\text{TPFPP})$, $\text{H}_2(\text{TPP})$ were prepared by the Lindsey methods [18]. The corresponding iron(III) complexes $\text{Fe}(\text{TMP})\text{Cl}$, $\text{Fe}(\text{TPFPP})\text{Cl}$, and $\text{Fe}(\text{TPP})\text{Cl}$ were also prepared by the literature methods [19]. $\text{Fe}(\text{OEP})\text{Cl}$ was purchased from Sigma-Aldrich. The iron(III) chloride porphyrin complexes were converted to the tetrafluoroborate or the perchlorate complexes by the reaction with AgBF_4 (4eq.) or AgClO_4 (3 eq.) in dehydrated THF solution. The crude solid was purified by the recrystallization from CH_2Cl_2 , THF and *n*-hexane. A series of six-coordinate complexes with two axial PyNO derivatives ligands (**1a-1f**, **2e**, **3e**, **4c**, and **4e**) were obtained at ambient temperature by the addition of the CD_2Cl_2 solution of each axial ligand (L: 10 eq.) into a CD_2Cl_2 solution of $\text{Fe}(\text{Por})\text{BF}_4$ or $\text{Fe}(\text{Por})\text{ClO}_4$ (10 μM) placed in an NMR sample tube. Addition of the ligand was continued until each signal showed no appreciable change in chemical shift. Analytically pure solid samples were obtained by recrystallization from CH_2Cl_2 and *n*-hexane.

2.2.2.2 Synthesis of $[\text{FeTMP}(4\text{-ClPyNO})_2]\text{BF}_4$: **1a**

Yield of **1a**: 72.8 %. *Anal.* Found: C, 66.70; H, 4.96; N, 7.09 %, Calcd. for $\text{C}_{66}\text{H}_{60}\text{N}_6\text{O}_2\text{Cl}_2\text{FeBF}_4$: C, 67.02; H, 5.11; N, 7.11 %. ^1H NMR (CD_2Cl_2 , 500 MHz, 298 K): $\delta = 59.8$ (Pyrrole-H, 8H), 8.9 (*meso-m*-H, 8H), 3.7 (*meso-p*-Me, 12H), and 3.0 ppm (*meso-o*-Me, 24H). UV-vis (CH_2Cl_2): $\lambda_{\text{max}}(\epsilon: 10^4 \text{ mol}^{-1}\text{dm}^3\text{cm}^{-1}) = 419$ (10.9), 509 (1.4), 577 (0.3), and 694 nm (0.3). HR-MS (ESI-TOF): Found: 965.3516 and 836.3541 m/z; Calcd. for $\text{C}_{61}\text{H}_{56}\text{N}_5\text{OClFe}$ ($[\text{M} - 4\text{-ClPyNO} - \text{BF}_4]^+$) and $\text{C}_{56}\text{H}_{52}\text{N}_4\text{Fe}$ ($[\text{M} - 2(4\text{-ClPyNO}) - \text{BF}_4]^+$) = 965.3519 and 836.3537 m/z. ESR (frozen CH_2Cl_2 -toluene, 15 K): $g_1 = 5.94$, $g_2 = 5.94$,

$g_3 = 1.99$; (solid, 4 K): $g_1 = 5.62$, $g_2 = 5.62$, $g_3 = 1.98$. SQUID (solid, 300 K): $\mu_{\text{eff.}} = 5.36 \mu_{\text{B}}$. Evans (CH_2Cl_2 , 298 K) $\mu_{\text{eff.}} = 5.76 \mu_{\text{B}}$.

2.2.2.3 Synthesis of $[\text{FeTMP}(\text{PyNO})_2]\text{BF}_4$: **1b**

Yield of **1b**: 75.4 %. *Anal.* Found: C, 70.89; H, 5.62; N, 8.02 %, Calcd. for $\text{C}_{66}\text{H}_{62}\text{N}_6\text{O}_2\text{FeBF}_4$: C, 71.17; H, 5.61; N, 7.54 %. $^1\text{H NMR}$ (CD_2Cl_2 , 500 MHz, 298 K): $\delta = 63.6$ (Pyrrole-H, 8H), 8.8 (*meso-m*-H, 8H), 3.6 (*meso-p*-Me, 12H), and 2.9 ppm (*meso-o*-Me, 24H). UV-vis (CH_2Cl_2): $\lambda_{\text{max}}(\epsilon: 10^4 \text{ mol}^{-1}\text{dm}^3\text{cm}^{-1}) = 416$ (10.3), 495 (1.0), 532 (1.1), 651 (0.2), and 698 nm (0.2). HR-MS (ESI-TOF): Found: 931.3893 and 836.3532 m/z; Calcd. for $\text{C}_{61}\text{H}_{57}\text{N}_5\text{OFe}$ ($[\text{M} - \text{PyNO} - \text{BF}_4]^+$) and $\text{C}_{56}\text{H}_{52}\text{N}_4\text{Fe}$ ($[\text{M} - 2(\text{PyNO}) - \text{BF}_4]^+$) = 931.3909 and 836.3537 m/z. ESR (frozen CH_2Cl_2 -toluene, 15 K): $g_1 = 5.88$, $g_2 = 5.88$, $g_3 = 1.99$; (solid, 4 K): $g_1 = 5.68$, $g_2 = 5.68$, $g_3 = 1.95$. SQUID (solid, 300 K): $\mu_{\text{eff.}} = 5.22 \mu_{\text{B}}$. Evans (CH_2Cl_2 , 298 K) $\mu_{\text{eff.}} = 5.54 \mu_{\text{B}}$.

2.2.2.4 Synthesis of $[\text{FeTMP}(4\text{-MePyNO})_2]\text{BF}_4$: **1c**

Yield of **1c**: 75.5 %. *Anal.* Found: C, 70.68; H, 5.50; N, 7.72 %, Calcd. for $\text{C}_{68}\text{H}_{66}\text{N}_6\text{O}_2\text{FeBF}_4 + \text{H}_2\text{O}$: C, 70.41; H, 5.91; N, 7.25 %. $^1\text{H NMR}$ (CD_2Cl_2 , 500 MHz, 298 K): $\delta = 66.8$ (Pyrrole-H, 8H), 56.0 (*4-MePyNO-p*-Me, 6H), 28.8 (*4-MePyNO-m*-H, 4H), 8.7 (*meso-m*-H, 8H), 3.5 (*meso-p*-Me, 12H), 2.8 (*meso-o*-Me, 24H), and -45.7 ppm (*4-MePyNO-o*-H, 4H). UV-vis (CH_2Cl_2): $\lambda_{\text{max}}(\epsilon: 10^4 \text{ mol}^{-1}\text{dm}^3\text{cm}^{-1}) = 416$ (11.4), 495 (1.0), 530 (1.1), 650 (2.2) and 689 nm (0.2). HR-MS (ESI-TOF): Found: 945.4085 and 836.3551 m/z; Calcd. for $\text{C}_{62}\text{H}_{59}\text{N}_5\text{OFe}$ ($[\text{M} - 4\text{-MePyNO} - \text{BF}_4]^+$) and $\text{C}_{56}\text{H}_{52}\text{N}_4\text{Fe}$ ($[\text{M} - 2(4\text{-MePyNO}) - \text{BF}_4]^+$) = 945.4065 and 836.3537 m/z. ESR (frozen CH_2Cl_2 -toluene, 15 K): $g_1 = 5.89$, $g_2 = 5.89$, $g_3 = 1.99$; (solid, 4 K): $g_1 = 2.41$, $g_2 = 2.23$, $g_3 = 1.92$. SQUID (solid, 300 K): $\mu_{\text{eff.}} = 4.98 \mu_{\text{B}}$. Evans (CH_2Cl_2 , 298 K) $\mu_{\text{eff.}} = 5.64 \mu_{\text{B}}$.

2.2.2.5 Synthesis of $[\text{FeTMP}(4\text{-OMePyNO})_2]\text{BF}_4$: **1d**

Yield of **1d**: 77.4 %. *Anal.* Found: C, 68.84; H, 5.38; N, 7.43 %, Calcd. for $\text{C}_{66}\text{H}_{66}\text{N}_6\text{O}_4\text{FeBF}_4 + \text{H}_2\text{O}$: C, 68.52; H, 5.75; N, 7.05 %. $^1\text{H NMR}$ (CD_2Cl_2 , 500 MHz, 298 K): $\delta = 67.8$ (Pyrrole-H, 8H), 22.4 (*4-OMePyNO-m*-H, 4H), 8.4 (*meso-m*-H, 8H), 3.7 (*4-OMePyNO-p*-OMe, 6H), 3.4 (*meso-p*-Me, 12H), 2.7 (*meso-o*-Me, 24H), and -38.6 ppm (*4-OMePyNO-o*-H, 4H). UV-vis (CH_2Cl_2): $\lambda_{\text{max}}(\epsilon: 10^4 \text{ mol}^{-1}\text{dm}^3\text{cm}^{-1}) = 417$ (11.5), 495 (1.0), 528 (1.0), 655 (0.2) and 686 nm (0.2). HR-MS (ESI-TOF): Found: 961.4015 and 836.3528 m/z; Calcd. for $\text{C}_{62}\text{H}_{59}\text{N}_5\text{O}_2\text{Fe}$ ($[\text{M} - 4\text{-MeOPyNO} - \text{BF}_4]^+$) and $\text{C}_{56}\text{H}_{52}\text{N}_4\text{Fe}$ ($[\text{M} - 2(4\text{-MeOPyNO}) - \text{BF}_4]^+$) = 961.4014 and 836.3537 m/z. ESR (frozen CH_2Cl_2 -toluene,

15 K): $g_1 = 2.41$, $g_2 = 2.22$, $g_3 = 1.92$; (solid, 4 K): $g_1 = 2.41$, $g_2 = 2.23$, $g_3 = 1.99$. SQUID (solid, 300 K): $\mu_{\text{eff.}} = 4.89 \mu_{\text{B}}$. Evans (CH_2Cl_2 , 298 K) $\mu_{\text{eff.}} = 5.43 \mu_{\text{B}}$.

2.2.2.6 Synthesis of $[\text{FeTMP}(4\text{-NMe}_2\text{PyNO})_2]\text{BF}_4$: **1e**

Yield of **1e**: 78.0 %. *Anal.* Found: C, 69.97; H, 5.85; N, 9.07 %, Calcd. for $\text{C}_{70}\text{H}_{72}\text{N}_8\text{O}_2\text{FeBF}_4$: C, 70.06; H, 6.05; N, 9.34 %. ^1H NMR (CD_2Cl_2 , 500 MHz, 298 K): $\delta = 57.4$ (Pyrrole-H, 8H), 18.2 (*4-NMe}_2\text{PyNO-}p\text{-N}(\text{Me})_2*, 12H), 16.5 (*4-NMe}_2\text{PyNO-}m\text{-H}*, 4H), 7.8 (*meso-m-H*, 8H), 3.0 (*meso-p-Me*, 12H), 2.3 (*meso-o-Me*, 24H), and -20.7 ppm (*4-NMe}_2\text{PyNO-}o\text{-H}*, 4H). UV-vis (CH_2Cl_2): $\lambda_{\text{max}}(\epsilon: 10^4 \text{ mol}^{-1}\text{dm}^3\text{cm}^{-1}) = 418$ (13.2), 491 (1.3), 526 (1.0), 646 (0.3) and 684 nm (0.2). HR-MS (ESI-TOF): Found: 974.4343 and 836.3523 m/z; Calcd. for $\text{C}_{63}\text{H}_{62}\text{N}_6\text{OFe}$ ($[\text{M} - 4\text{-NMe}_2\text{-PyNO} - \text{BF}_4]^+$) and $\text{C}_{56}\text{H}_{52}\text{N}_4\text{Fe}$ ($[\text{M} - 2(4\text{-NMe}_2\text{PyNO}) - \text{BF}_4]^+$) = 974.4331 and 836.3537 m/z. ESR (frozen CH_2Cl_2 -toluene, 15 K): $g_1 = 2.39$, $g_2 = 2.21$, $g_3 = 1.93$; (solid, 4 K): $g_1 = 2.41$, $g_2 = 2.22$, $g_3 = 1.93$. SQUID (solid, 300 K): $\mu_{\text{eff.}} = 4.23 \mu_{\text{B}}$. Evans (CH_2Cl_2 , 298 K) $\mu_{\text{eff.}} = 4.74 \mu_{\text{B}}$.

2.2.2.7 Synthesis of $[\text{FeTMP}(3,5\text{-Me}_2\text{PyNO})_2]\text{ClO}_4$: **1f**

Yield of **1f**: 74.5 %. ^1H NMR (CD_2Cl_2 , 500 MHz, 298 K): $\delta = 67.3$ (Pyrrole-H, 8H), 8.9 (*meso-m-H*, 8H), 3.6 (*meso-p-Me*, 12H), 3.0 (*meso-o-Me*, 24H), -18.3 (*3,5-Me}_2\text{PyNO-}m\text{-Me}*, 6H), -50.5 (*3,5-Me}_2\text{PyNO-}p\text{-H}*, 2H), and -50.9 ppm (*3,5-Me}_2\text{PyNO-}o\text{-H}*, 4H). UV-vis (CH_2Cl_2): $\lambda_{\text{max}}(\epsilon: 10^4 \text{ mol}^{-1}\text{dm}^3\text{cm}^{-1}) = 396$ (sh, 11.1), 416 (12.5), 505 (1.4), 529 (1.5), 658 (sh, 0.3), and 693 nm (0.3). HR-MS (ESI-TOF): Found: 959.4197 m/z; Calcd. for $\text{C}_{63}\text{H}_{61}\text{N}_5\text{OFe}$ ($[\text{M} - 3,5\text{-Me}_2\text{PyNO} - \text{ClO}_4]^+$) = 959.4222 m/z. ESR (frozen CH_2Cl_2 -toluene, 15 K): $g_1 = 5.78$, $g_2 = 5.78$, $g_3 = 2.00$; (solid, 4 K): $g_1 = 5.66(2.41)$, $g_2 = 5.66(2.23)$, $g_3 = 2.00(1.94)$. SQUID (solid, 300 K): $\mu_{\text{eff.}} = 5.22 \mu_{\text{B}}$.

2.2.2.8 Synthesis of $[\text{FeTPFPP}(4\text{-NMe}_2\text{PyNO})_2]\text{BF}_4$: **2e**

Yield of **2e**: 80.1 %. *Anal.* Found: C, 49.82; H, 2.33; N, 7.81 %, Calcd. for $\text{C}_{58}\text{H}_{28}\text{N}_8\text{O}_2\text{FeBF}_4$: C, 50.06; H, 2.03; N, 8.05 %. ^1H NMR (CD_2Cl_2 , 500 MHz, 298 K): $\delta = 24.1$ (Pyrrole-H, 8H), 12.7 (*4-NMe}_2\text{PyNO-}m\text{-H}*, 4H), 9.6 (*4-NMe}_2\text{PyNO-}p\text{-N}(\text{Me})_2*, 12H), and -4.3 (*4-NMe}_2\text{PyNO-}o\text{-H}*, 4H). ^{19}F NMR (CD_2Cl_2 , 470 MHz, 298 K): $\delta = -139.8$ (*meso-o-F*, 8F), -154.4 (*meso-p-F*, 4F), and -164.1 ppm (*meso-o-H*, 8F). UV-vis (CH_2Cl_2): $\lambda_{\text{max}}(\epsilon: 10^4 \text{ mol}^{-1}\text{dm}^3\text{cm}^{-1}) = 408$ (10.9), 488 (1.5), and 581 nm (1.0). HR-MS (ESI-TOF): Found: 1304.1361, 1166.0580 and 1027.9761 m/z; Calcd. for $\text{C}_{58}\text{H}_{28}\text{N}_8\text{O}_2\text{F}_{20}\text{Fe}$ ($[\text{M} - \text{BF}_4]^+$), $\text{C}_{51}\text{H}_{18}\text{N}_6\text{OF}_{20}\text{Fe}$ ($[\text{M} - 4\text{-NMe}_2\text{PyNO} - \text{BF}_4]^+$) and $\text{C}_{44}\text{H}_8\text{N}_4\text{F}_{20}\text{Fe}$ ($[\text{M} - 2(4\text{-NMe}_2\text{PyNO}) - \text{BF}_4]^+$) = 1304.1361, 1166.0568 and 1027.9774 m/z. ESR (frozen CH_2Cl_2 -toluene, 15 K):

$g_1 = 2.42$, $g_2 = 2.22$, $g_3 = 1.92$; (solid, 4 K): $g_1 = 2.37$, $g_2 = 2.19$, $g_3 = 1.95$. SQUID (solid, 300 K): $\mu_{\text{eff.}} = 2.49 \mu_{\text{B}}$. Evans (CH_2Cl_2 , 298 K) $\mu_{\text{eff.}} = 3.74 \mu_{\text{B}}$.

2.2.2.9 Synthesis of $[\text{FeTPP}(4\text{-NMe}_2\text{PyNO})_2]\text{BF}_4$: **3e**

Yield of **3e**: 78.0 %. $^1\text{H NMR}$ (CD_2Cl_2 , 500 MHz, 298 K): $\delta = 55.3$ (Pyrrole-H, 8H), 18.9 ($4\text{-NMe}_2\text{PyNO-p-NMe}_2$, 12H), 15.1 ($4\text{-NMe}_2\text{PyNO-m-H}$, 4H), 10.6 (*meso-o*-H, 8H), 8.9 (*meso-p*-H, 4H), 8.5 (*meso-m*-H, 8H), and -20.5 ppm ($4\text{-NMe}_2\text{PyNO-o-H}$, 4H). HR-MS (ESI-TOF): Found: 806.2468 m/z; Calcd. for $\text{C}_{51}\text{H}_{38}\text{N}_6\text{OFe}$ ($[\text{M} - 4\text{-NMe}_2\text{PyNO} - \text{BF}_4]^+$) = 806.2452 m/z. ESR (frozen CH_2Cl_2 -toluene, 15 K): $g_1 = 2.41$ $g_2 = 2.21$, $g_3 = 1.93$; (solid, 4 K): $g_1 = 2.39$, $g_2 = 2.21$, $g_3 = 1.93$. SQUID (solid, 300 K): $\mu_{\text{eff.}} = 3.19 \mu_{\text{B}}$. Evans (CH_2Cl_2 , 298 K) $\mu_{\text{eff.}} = 4.98 \mu_{\text{B}}$.

2.2.2.10 Synthesis of $[\text{FeOEP}(4\text{-MePyNO})_2]\text{BF}_4$: **4c**

Yield of **4c**: 87.3 %. $^1\text{H NMR}$ (CD_2Cl_2 , 500 MHz, 298 K): $\delta = 60.2$ (4-MePyNO-p-Me , 6H), 46.5 (Pyrrole- CH_2 -, 16H), 39.5 (4-MePyNO-o-H , 4H), 26.7 (4-MePyNO-m-H , 4H), 7.4 (Pyrrole- CH_3 , 24H), and -51.1 ppm (*meso*-H, 4H). UV-vis (CH_2Cl_2): $\lambda_{\text{max}}(\epsilon: 10^4 \text{ mol}^{-1} \text{ dm}^3 \text{ cm}^{-1}) = 394$ (14.2), 500 (0.9), 530 (sh, 0.7), and 617 nm (0.5). HR-MS (ESI-TOF): Found: 697.3439 and 588.2928 m/z; Calcd. for $\text{C}_{42}\text{H}_{51}\text{N}_5\text{OFe}$ ($[\text{M} - 4\text{-MePyNO} - \text{BF}_4]^+$) and $\text{C}_{36}\text{H}_{44}\text{N}_4\text{Fe}$ ($[\text{M} - 2(4\text{-MePyNO}) - \text{BF}_4]^+$) = 931.3438 and 588.2910 m/z. ESR (frozen CH_2Cl_2 -toluene, 15 K): $g_1 = 5.78$, $g_2 = 5.78$, $g_3 = 2.00$. SQUID (solid, 300 K): $\mu_{\text{eff.}} = 5.57 \mu_{\text{B}}$.

2.2.2.11 Synthesis of $[\text{FeOEP}(4\text{-NMe}_2\text{PyNO})_2]\text{BF}_4$: **4e**

Yield of **4e**: 85.5 %. $^1\text{H NMR}$ (CD_2Cl_2 , 500 MHz, 298 K): $\delta = 40.1$ (Pyrrole- CH_2 -, 16H), 32.8 ($4\text{-NMe}_2\text{PyNO-o-H}$, 4H), 21.6 ($4\text{-NMe}_2\text{PyNO-p-NMe}_2$, 12H), 6.2 (Pyrrole- CH_3 , 24H), and -29.4 ppm (*meso*-H, 4H). HR-MS (ESI-TOF): Found: 726.3719 m/z; Calcd. for $\text{C}_{43}\text{H}_{54}\text{N}_6\text{OFe}$ ($[\text{M} - 4\text{-NMe}_2\text{PyNO} - \text{BF}_4]^+$) = 726.3704 m/z. ESR (frozen toluene, 15 K): $g_1 = 5.73(2.41)$, $g_2 = 5.73(2.21)$, $g_3 = 1.99(1.93)$. SQUID (solid, 300 K): $\mu_{\text{eff.}} = 5.06 \mu_{\text{B}}$.

2.2.3 X-ray Crystallographic structure solution and refinement

Crystals suitable for X-ray structure analysis were obtained from CH_2Cl_2 / *n*-hexane mixed-solvent solutions for **1a**, **1c**, **3e**, **4c**, and **4e**, from CH_2Cl_2 / toluene / *n*-hexane mixed-solvent solutions for **1e** and **2e**, and from CHCl_3 / *n*-hexane mixed-solvent solutions for **1f**. X-ray measurements of the single crystals were done with Rigaku VariMax Saturn-724 (1.2 kW Mo rotating anode) at 100 K for **1a**, **1c**, **1e**, **1f**, **2e**, **3e**, **4c**, and **4e**, and at 300 K

for **1c** and **4e**. Single crystals for X-ray analysis were obtained by the diffusion method. X-ray diffraction data were processed using Crystal Clear 1.6.3 followed by CrystalStructure Ver. 4.2.1. Structures were solved from the processed data using SIR 2011 and SHELXT Ver. 2014/5 program package, and then refined by SHELXL-2016/6 program package [20, 21]. Final structures were validated by Platon CIF check. Crystallographic data for complex **1a**, **1c**, **1e**, **1f**, **2e**, and **4c** reported in this paper have been deposited with the Cambridge Crystallographic Data Centre, CCDC nos. 1487353, 1487354, 1487355, 1487356, 1540939, 1487357, and 1511858. Copies of the information may be obtained free of charge from: The Director, CCDC, 12 Union Road, Cambridge, CB2 1EZ, UK (fax: +44-1223-336033; e-mail: deposit@ccdc.cam.ac.uk or via http://www.ccdc.cam.ac.uk/data_request/cif). Crystal data and details concerning the data collection are given in Table 2-1 for **1a**, **1c**, **1e**, **1f**, **2e**, **3e**, **4c**, and **4e**. All non-hydrogen atoms were refined anisotropically. Hydrogen atoms were located in the calculated positions and refined by using a riding mode.

2 Spin-crossover Between High-spin ($S=5/2$) and Low-spin ($S=1/2$) States of Six-coordinate Iron(III) Porphyrins with Two Pyridine-*N* Oxide Derivatives

Table 2-1. Crystal data and data collection details.

| Compound | 1a · 2CH ₂ Cl ₂ | 1c | 1c | 1c | 1e · 2 toluene | 1f · 2CHCl ₃ |
|--|---|---|---|---|---|---|
| Chemical formula | C ₆₂ H ₁₂ N ₂ O ₂ Cl ₂ FeBr ₄ · 2(CH ₂ Cl ₂) | C ₆₂ H ₁₂ N ₂ O ₂ FeBr ₄ | C ₆₂ H ₁₂ N ₂ O ₂ FeBr ₄ | C ₆₂ H ₁₂ N ₂ O ₂ FeBr ₄ | C ₆₂ H ₁₂ N ₂ O ₂ FeBr ₄ · 2(C ₇ H ₈) | C ₆₂ H ₁₂ N ₂ O ₂ FeBr ₄ · 2CHCl ₃ |
| Density (K) | 100(2) | 300(2) | 100(2) | 100(2) | 100(2) | 100(2) |
| Formula weight | 1352.81 | 1141.92 | 1141.92 | 1394.28 | 1421.35 | 1421.35 |
| Crystal size (mm) | 0.15 x 0.15 x 0.10 | 0.25 x 0.10 x 0.08 | 0.50 x 0.40 x 0.40 | 0.20 x 0.05 x 0.02 | 0.30 x 0.14 x 0.05 | 0.30 x 0.14 x 0.05 |
| Crystal color | brown | brown | brown | black | brown | brown |
| Crystal system | Triclinic | Monoclinic | Monoclinic | Triclinic | Triclinic | Triclinic |
| Space group | PT | C _{2h} | C _{2h} | PT | PT | PT |
| Wave length (Å) | 0.71075 | 0.71075 | 0.71075 | 0.71075 | 0.71075 | 0.71075 |
| a (Å) | 12.983(9) | 23.583(3) | 23.480(6) | 14.532(2) | 19.289(1) | 19.289(1) |
| b (Å) | 13.831(9) | 14.931(3) | 14.606(3) | 15.213(2) | 15.859(1) | 15.859(1) |
| c (Å) | 18.824(6) | 17.644(4) | 17.569(4) | 18.230(3) | 16.240(1) | 16.240(1) |
| a (°) | 109.924(2) | 90 | 90 | 70.093(8) | 84.596(2) | 84.596(2) |
| b (°) | 95.24(2) | 112.617(3) | 114.161(3) | 76.760(9) | 63.769(3) | 63.769(3) |
| g (°) | 100.09(2) | 90 | 90 | 77.769(9) | 84.162(2) | 84.162(2) |
| Volume (Å ³) | 3252(2) | 6168(2) | 5966(2) | 3618(1) | 3508(1) | 3508(1) |
| Z | 2 | 4 | 4 | 2 | 2 | 2 |
| Density (Calculated) (g cm ⁻³) | 1.381 | 1.230 | 1.271 | 1.271 | 1.271 | 1.345 |
| Absorption coefficient (mm ⁻¹) | 0.540 | 0.305 | 0.316 | 0.273 | 0.537 | 0.537 |
| Absorption correction | multi-scan | multi-scan | multi-scan | multi-scan | multi-scan | multi-scan |
| Max. and Min. transmission | 0.948 and 0.863 | 0.976 and 0.928 | 0.987 and 0.984 | 0.995 and 0.947 | 0.974 and 0.842 | 0.974 and 0.842 |
| F (000) | 1398 | 2396 | 2396 | 1462 | 1478 | 1478 |
| #Range for data collection (°) | 2.01 to 28.0 | 1.62 to 28.0 | 1.62 to 28.0 | 1.90 to 28.5 | 1.85 to 28.0 | 1.85 to 28.0 |
| Reflections collected | -17<=h<=17, -18<=k<=18, -28<=l<=28 | -33<=h<=33, -19<=k<=19, -23<=l<=23 | -33<=h<=33, -19<=k<=19, -23<=l<=23 | -18<=h<=18, -19<=k<=19, -22<=l<=22 | -20<=h<=20, -20<=k<=20, -21<=l<=21 | -20<=h<=20, -20<=k<=20, -21<=l<=21 |
| Independent reflections | 15681 | 7452 | 7218 | 14974 | 16923 | 16923 |
| Refinement method | 12984 [R _{int} = 0.0683] | 5678 [R _{int} = 0.0690] | 6683 [R _{int} = 0.0985] | 10409 [R _{int} = 0.0977] | 11522 [R _{int} = 0.0628] | 11522 [R _{int} = 0.0628] |
| Data/restraints/parameters | 15661 / 6 / 836 | 7452 / 81 / 401 | 7218 / 60 / 401 | 14974 / 0 / 922 | 16923 / 190 / 922 | 16923 / 190 / 922 |
| Goodness-of-fit on F ² | 1.053 | 1.142 | 1.142 | 1.141 | 1.023 | 1.023 |
| Final R indices (I>2σ(I)) | R ₁ = 0.0683, wR ₂ = 0.1439 | R ₁ = 0.0890, wR ₂ = 0.1802 | R ₁ = 0.0985, wR ₂ = 0.1941 | R ₁ = 0.0977, wR ₂ = 0.1846 | R ₁ = 0.0628, wR ₂ = 0.1327 | R ₁ = 0.0628, wR ₂ = 0.1327 |
| R indices (all data) | R ₁ = 0.0843, wR ₂ = 0.1552 | R ₁ = 0.0947, wR ₂ = 0.1975 | R ₁ = 0.1097, wR ₂ = 0.1986 | R ₁ = 0.1382, wR ₂ = 0.2062 | R ₁ = 0.1012, wR ₂ = 0.1517 | R ₁ = 0.1012, wR ₂ = 0.1517 |
| Largest peak and hole (e Å ⁻³) | +0.81 and -0.91 | +0.29 and -0.54 | +0.57 and -0.50 | +0.56 and -0.48 | +0.80 and -0.84 | +0.80 and -0.84 |
| Compound | 2e · CH ₂ Cl ₂ + 2.5 toluene | 3e · 2CH ₂ Cl ₂ | 4c | 4e · 2CH ₂ Cl ₂ | 4e · 2CH ₂ Cl ₂ | 4e · 2CH ₂ Cl ₂ |
| Temperature (K) | 100(2) | 100(2) | 100(2) | 300(2) | 100(2) | 100(2) |
| Chemical formula | C ₆₂ H ₁₂ N ₂ O ₂ FeBr ₄ · CH ₂ Cl ₂ · 2.5(C ₇ H ₈) | C ₆₂ H ₁₂ N ₂ O ₂ FeBr ₄ · 2(CH ₂ Cl ₂) | C ₆₂ H ₁₂ N ₂ O ₂ FeBr ₄ | C ₆₂ H ₁₂ N ₂ O ₂ FeBr ₄ · 2(CH ₂ Cl ₂) | C ₆₂ H ₁₂ N ₂ O ₂ FeBr ₄ · 2(CH ₂ Cl ₂) | C ₆₂ H ₁₂ N ₂ O ₂ FeBr ₄ · 2(CH ₂ Cl ₂) |
| Formula weight | 1706.80 | 1201.59 | 893.68 | 1121.62 | 1121.62 | 1121.62 |
| Crystal size (mm) | 0.18 x 0.06 x 0.02 | 0.15 x 0.10 x 0.07 | 0.20 x 0.04 x 0.02 | 0.12 x 0.10 x 0.09 | 0.12 x 0.10 x 0.09 | 0.12 x 0.10 x 0.09 |
| Crystal color | black | violet | brown | brown | brown | brown |
| Crystal system | Triclinic | Triclinic | Triclinic | Orthorhombic | Orthorhombic | Orthorhombic |
| Space group | PT | PT | PT | Pccn | Pccn | Pccn |
| Wave length (Å) | 0.71075 | 0.71075 | 0.71075 | 0.71075 | 0.71075 | 0.71075 |
| a (Å) | 14.756(2) | 9.744(2) | 7.9064(2) | 15.593(1) | 15.593(1) | 15.593(1) |
| b (Å) | 15.299(2) | 13.193(3) | 13.709(1) | 23.509(1) | 23.509(1) | 23.509(1) |
| c (Å) | 18.938(2) | 21.788(5) | 20.754(1) | 15.429(1) | 15.429(1) | 15.278(1) |
| a (°) | 92.515(14) | 91.970(5) | 90.870(2) | 90 | 90 | 90 |
| b (°) | 108.315(10) | 96.579(3) | 92.579(2) | 90 | 90 | 90 |
| g (°) | 117.216(8) | 98.536(4) | 93.419(2) | 90 | 90 | 90 |
| Volume (Å ³) | 3619(1) | 2748(1) | 2243(1) | 5656(1) | 5352(1) | 5352(1) |
| Z | 2 | 2 | 2 | 4 | 4 | 4 |
| Density (Calculated) (g cm ⁻³) | 1.611 | 1.452 | 1.333 | 1.317 | 1.392 | 1.392 |
| Absorption coefficient (mm ⁻¹) | 0.410 | 0.536 | 0.399 | 0.515 | 0.544 | 0.544 |
| Absorption correction | multi-scan | multi-scan | multi-scan | multi-scan | multi-scan | multi-scan |
| Max. and Min. transmission | 0.992 and 0.930 | 0.963 and 0.865 | 0.992 and 0.835 | 0.955 and 0.836 | 0.852 and 0.933 | 0.852 and 0.933 |
| F (000) | 1724 | 1238 | 942 | 2348 | 2348 | 2348 |
| #Range for data collection (°) | 2.12 to 26.5 | 1.78 to 28.0 | 1.77 to 28.0 | 1.73 to 28.0 | 1.61 to 28.0 | 1.61 to 28.0 |
| Reflections collected | -18<=h<=18, -19<=k<=19, -23<=l<=23 | -12<=h<=12, -17<=k<=17, -28<=l<=28 | -10<=h<=10, -18<=k<=18, -27<=l<=27 | -20<=h<=20, -31<=k<=31, -20<=l<=20 | -30<=h<=30, -19<=k<=19, -20<=l<=20 | -30<=h<=30, -19<=k<=19, -20<=l<=20 |
| Independent reflections | 10094 [R _{int} = 0.0977] | 10355 [R _{int} = 0.0654] | 8089 [R _{int} = 0.0517] | 4452 [R _{int} = 0.0605] | 5644 [R _{int} = 0.0339] | 5644 [R _{int} = 0.0339] |
| Refinement method | Full-matrix least-squares on F ² | Full-matrix least-squares on F ² | Full-matrix least-squares on F ² | Full-matrix least-squares on F ² | Full-matrix least-squares on F ² | Full-matrix least-squares on F ² |
| Data/restraints/parameters | 14590 / 375 / 1163 | 15222 / 0 / 725 | 10229 / 69 / 701 | 10229 / 0 / 333 | 6473 / 0 / 333 | 6473 / 0 / 333 |
| Goodness-of-fit on F ² | 1.046 | 1.136 | 1.027 | 1.020 | 1.041 | 1.041 |
| Final R indices (I>2σ(I)) | R ₁ = 0.0898, wR ₂ = 0.2119 | R ₁ = 0.0945, wR ₂ = 0.1603 | R ₁ = 0.0517, wR ₂ = 0.1002 | R ₁ = 0.0773, wR ₂ = 0.1167 | R ₁ = 0.0339, wR ₂ = 0.0800 | R ₁ = 0.0339, wR ₂ = 0.0800 |
| R indices (all data) | R ₁ = 0.1373, wR ₂ = 0.2368 | +0.67 and -0.66 | +0.34 and -0.44 | +0.36 and -0.36 | +0.39 and -0.32 | +0.39 and -0.32 |
| Largest peak and hole (e Å ⁻³) | +0.90 and -0.51 | | | | | |

Table 2-2. The selected structural parameters for six-coordinate iron(III) porphyrin complexes with two substituted pyridine *N*-oxides as axial ligand.

| Complex | T (K) | Fe-N ^a | Fe-O ^a | N-O ^a | Fe-O-N ^b | N-O-O-N ^c | θ^d | σ^e |
|--|-------|-------------------|-------------------|------------------|---------------------|----------------------|------------|------------|
| FeTMP(4-ClPyNO)₂BF₄ : 1a | 100 | 2.054(2) | 2.047(3) | 1.337(3) | 125.3(2) | 180.0 | 9.0 | 0.000 |
| FeTMP(4-MePyNO)₂BF₄ : 1c | 300 | 2.048(2) | 2.048(2) | 1.336(6) | 123.7(1) | 180.0 | 7.8 | 0.000 |
| | 100 | 2.029(3) | 2.001(2) | 1.347(4) | 122.0(2) | 180.0 | 9.1 | 0.000 |
| FeTMP(4-NMe₂PyNO)₂BF₄ : 1e | 100 | 1.997(4) | 1.904(3) | 1.364(6) | 120.2(2) | 180.0 | 9.1 | 0.000 |
| FeTMP(3,5-Me₂PyNO)₂ClO₄ : 1f | 100 | 2.041(3) | 2.033(3) | 1.343(3) | 118.8(2) | 180.0 | 8.0 | 0.000 |
| FeTMP(4-NMe₂PyNO)₂BF₄ : 1e | 100 | 1.997(4) | 1.904(3) | 1.364(6) | 120.2(2) | 180.0 | 9.1 | 0.000 |
| FeTPFPP(4-NMe₂PyNO)₂BF₄ : 2e | 100 | 1.996(6) | 1.908(3) | 1.368(7) | 123.4(2) | 172.4 | 6.2 | 0.026 |
| FeTPP(4-NMe₂PyNO)₂BF₄ : 3e | 100 | 2.003(2) | 1.912(2) | 1.367(3) | 118.7(2) | 177.7 | 5.2 | 0.005 |
| FeOEP(4-MePyNO)₂BF₄ : 4c | 100 | 2.044(2) | 2.093(1) | 1.336(3) | 117.3(1) | 180.0 | 1.9 | 0.000 |
| FeOEP(4-NMe₂PyNO)₂BF₄ : 4e | 300 | 2.046(2) | 2.062(2) | 1.357(3) | 120.0(2) | 180.0 | 0.1 | 0.000 |
| | 100 | 2.006(1) | 1.955(1) | 1.360(1) | 118.7(1) | 180.0 | 1.2 | 0.000 |

^aAveraged bond lengths(Å). ^bAveraged angles(°). ^cAveraged torsion angles(°).

^dAveraged angles(°) between heme normal and Fe-O bonds.

^eDistances(Å) between Fe atom and the least-square plane of porphyrin ring.

2.3 Results and Discussion

2.3.1 X-ray Crystallography

Molecular structures of **1a**, **1c**, **1e**, **1f**, **2e**, **3e**, **4c**, and **4e** were determined by X-ray crystallography at 100 K. Table 2-2 lists the selected structural parameters. First, the ORTEP drawings of the six-coordinate iron(III) *meso*-tetramesitylporphyrin cation complexes [Fe(TMP)L₂]⁺ (L = 4-ClPyNO (**1a**), 4-MePyNO (**1c**), 4-NMe₂PyNO (**1e**), and 3,5-Me₂PyNO (**1f**)) bearing two substituted pyridine *N*-oxide as axial ligands are given in Figure 2-1, 2-2, 2-3, and 2-4, respectively. In each complex, the porphyrin ring is almost planar and the iron(III) ion is located within the porphyrin plane perfectly. The O-Fe-O angles are close to 180° in all the complexes examined. The Fe-O axes are tilted from the heme normal by 7.8-9.1°. The average Fe-O-N angles between the Fe(III) ion and the coordinated axial ligands are 120-125°. The torsion angles N-O-O-N in two substituted pyridine *N*-oxide ligands are 180°. This indicated that two pyridine rings are almost parallel and they are oriented along the C_{meso}-Fe-C_{meso} axis to the opposite directions to form a transoid structure. Thus, the ligand orientation in these complexes contrasts to that of analogous [Fe(TPP)(3,5-Me₂PyNO)₂]⁺ where two pyridine rings take an eclipsed conformation and correctly sandwich the porphyrin ring [15].

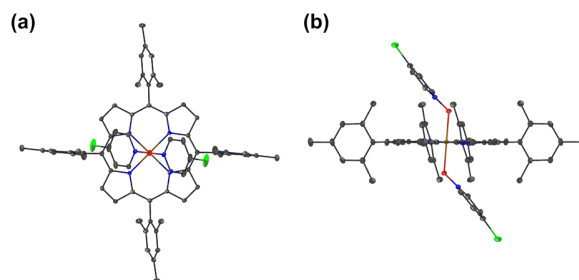


Figure 2-1. ORTEP drawing of **1a** · 2CH₂Cl₂ (100 K) seen along the: (a) O–Fe–O and (b) N–Fe–N axis, showing the thermal ellipsoids at the 30% probability level. Hydrogen,

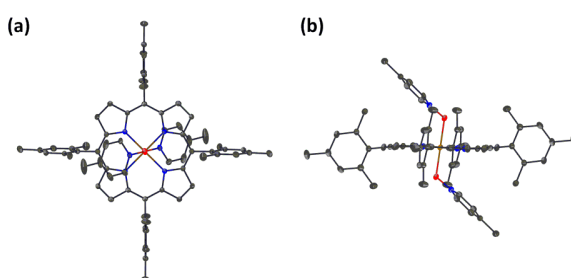


Figure 2-2. ORTEP drawing of **1c** (100 K) seen along the: (a) O–Fe–O and (b) N–Fe–N axis, showing the thermal ellipsoids at the 30% probability level. Hydrogen, solvent, and counter anion atoms are omitted for clarity.

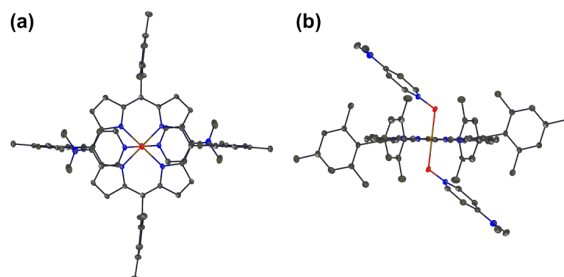


Figure 2-3. ORTEP drawing of **1e** · 2CH₂Cl₂ (100 K) seen along the: (a) O–Fe–O and (b) N–Fe–N axis, showing the thermal ellipsoids at the 30% probability level. Hydrogen, solvent, and counter anion atoms are omitted for clarity.

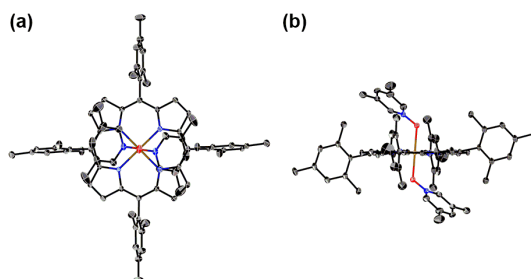


Figure 2-4. ORTEP drawing of **1f** (100 K) seen along the: (a) O–Fe–O and (b) N–Fe–N axis, showing the thermal ellipsoids at the 50% probability level. Hydrogen, solvent, and counter anion atoms are omitted for clarity.

Six-coordinate iron(III) porphyrin complexes with two neutral oxygen ligands such as pyridine *N*-oxides, DMSO, DMF, methanol, and THF are known to adopt a pure $S = 5/2$ state, a mixed $S = 5/2$ and $3/2$ state, or a pure $S = 3/2$ state depending on the field strength of axial ligands and the deformation of the porphyrin ring [16]. For example, a weaker field ligand with a deformed porphyrin ring such as $[\text{Fe}(\text{T}^i\text{PrP})(\text{THF})_2]^+$ adopts a quite pure $S = 3/2$ state, which confirmed by X-ray crystallography, ESR, and NMR measurements: T^iPrP is *meso*-tetraisopropylporphyrin [16,22]. The average Fe- N_p and Fe-O bond length in $[\text{Fe}(\text{T}^i\text{PrP})(\text{THF})_2]^+$ were 1.967(12) and 2.202(19) Å, respectively. The short Fe- N_p distance for the equatorial coordination destabilized the corresponding $d_{x^2-y^2}$ orbital, while the long Fe-O distance for the axial coordination stabilized the corresponding d_x^2 orbital, resulting in a quite pure $S = 3/2$ state. On the other hand, the average Fe- N_p bond lengths in the six-coordinated iron(III) complexes with a planar porphyrin ring **1a**, **1c**, **1e**, and **1f** are 2.054(2), 2.029(3), 1.997(4), and 2.041(3) Å, respectively. The average Fe-O bond lengths for these complexes are 2.047(3), 2.001(2), 1.904(3), and 2.033(3) Å, respectively. Stepwise decrease of both Fe- N_p and Fe-O bonds on going from **1a** and **1f** to **1c**, and then to **1e** indicate the removal of an electron from both $d_{x^2-y^2}$ and d_z^2 orbitals due to the destabilization of the corresponding d orbitals, which in turn indicates that **1a** adopts the $S = 5/2$ state while **1e** adopt the $S=1/2$ state at 100 K. The average Fe- N_p and Fe-O bond lengths of **1f** are the intermediate value between **1a** and **1c**, that suggested the correlation by the difference of affinity of substituted pyridine *N*-oxides to Fe(III) ion: 4-CIPyNO < 3,5-Me₂PyNO < 4-MePyNO < 4-NMe₂PyNO. For further consideration, the structural analysis of **1c** was also carried out at 300 K as shown in Figure 2-5, and the obtained structural parameters are given in Table 2-2. Both the average Fe- N_p and Fe-O lengths in **1c** have increased by 0.019 and 0.047 Å, respectively, when the temperature is raised to 300 K. Therefore, the affinity relationship of substituted pyridine *N*-oxides to Fe(III) ion is written as follows: 4-CIPyNO (100 K) \rightleftharpoons 4-MePyNO (300 K) < 3,5-Me₂PyNO (100 K) < 4-MePyNO (100 K) < 4-NMe₂PyNO (100 K). The increase in the Fe- N_p and Fe-O bond lengths of **1c** at higher temperature is a strong support of spin crossover in **1c** from the structural point of view. As listed in Table 2-1, the volume of the unit cell decreased from 6168(2) Å³ at 300 K to 5966(2) Å³ at 100 K. Although the decrease of the volume is only 3.8%, it would certainly destabilize the high-spin state at 100 K since the Fe-O bond length at 300 K is 2.048 Å while that at 100 K is 2.001 Å [7,23].

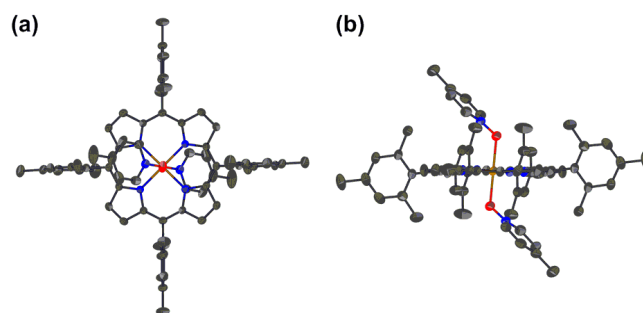


Figure 2-5. ORTEP drawing of **1c** (300 K) seen along the: (a) O–Fe–O and (b) N–Fe–N axis, showing the thermal ellipsoids at the 30% probability level. Hydrogen, solvent, and counter anion atoms are omitted for clarity.

As the subsequent strategy, the author explored the structural properties of a series of iron(III) *meso*-tetraarylsubstituted porphyrin complexes with two 4-NMe₂PyNO as axial ligand by X-ray crystal structure analyses. The substituents are pentafluorophenyl (TPFPP, **2**) and phenyl (TPP, **3**). Although the *meso*-pentafluorophenyl group has a high electron-withdrawing property, the *meso*-mesityl group has a high electron-donating property. In general, the *meso*-tetraphenyl group has been known as the reference sample in a wide range of research fields. Figure 2-6 and 2-7 show the ORTEP drawings of **2e** and **3e** at 100 K. Basically, the six-coordinate framework and the planarity of porphyrin ring resemble to ones of the six-coordinate iron(III) complexes **1a-1f**. The average Fe–N_p bond lengths for **2e** and **3e** are 1.996(6) and 2.003(2) Å, respectively. The average Fe–O bond lengths for these complexes are 1.908(3) and 1.912(2) Å, respectively. These bond lengths are comparable to the corresponding bond lengths of **1e**, which indicates that **2e** and **3e** also adopt the $S=1/2$ state at 100 K.

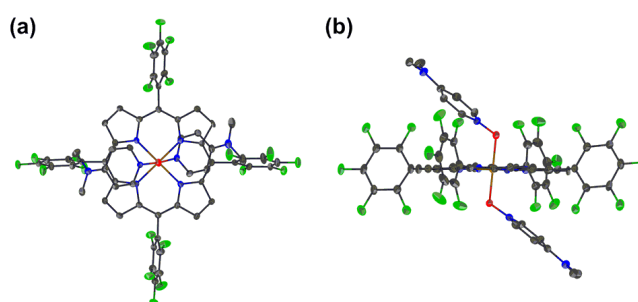


Figure 2-6. ORTEP drawing of **2e** · 2CH₂Cl₂ (100 K) seen along the: (a) O–Fe–O and (b) N–Fe–N axis, showing the thermal ellipsoids at the 30% probability level. Hydrogen, solvent, and counter anion atoms are omitted for clarity.

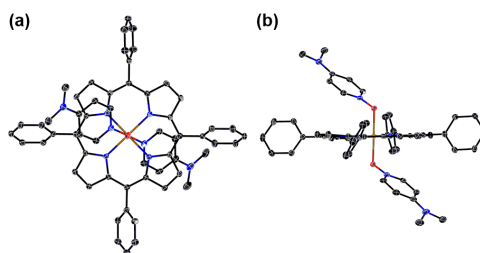


Figure 2-7. ORTEP drawing of **3e** (100 K) seen along the: (a) O–Fe–O and (b) N–Fe–N axis, showing the thermal ellipsoids at the 50% probability level. Hydrogen, solvent, and counter anion atoms are omitted for clarity.

Furthermore, as the models for the prosthetic group in heme proteins, structures of six-coordinate iron(III) OEP complexes with two 4-MePyNO or 4-NMe₂PyNO as axial ligands were confirmed by the single-crystal X-ray analysis: OEP is octaethylporphyrin and have eight ethyl groups at the pyrrole- β position. Figure 2-8, -9, and -10 show the ORTEP drawings of **4c** at 100 K and **4e** at 100 and 300K. In both **4c** and **4e**, the porphyrin ring is planar and the iron(III) ion is located within the porphyrin plane. The average Fe–N bond length of **4c**, 2.045(2) Å, is quite close to that of **1a** (2.054(2) Å). In contrast, the average Fe–O bond length of **4c**, 2.093(1) Å, is longer than that of **1a** (2.047(3) Å) by 0.046 Å. In the case of **4e**, both the average Fe–N_p and Fe–O lengths increased from 2.006(1) and 1.955(1) Å at 100 K to 2.046(2) and 2.062(2) Å at 300 K. Although these bond lengths at 300 K are quite close to one of the corresponding bonds of **1c** at 300 K, *i.e.* both of 2.048(2) Å, these bond distances at 100 K are a little shorter than one of the corresponding bonds of **1c** at 100 K, *i.e.* 2.029(3) and 2.001(2) Å, respectively. These results are thought to be the cause of the difference of the field strength of axial ligands and the steric hindrance and the electron property of ring-periphery substituents.

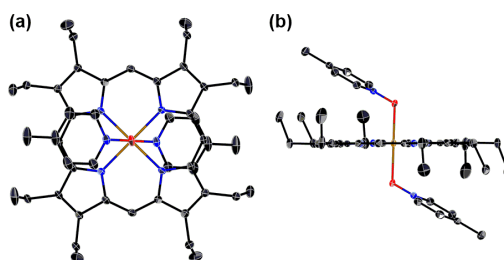


Figure 2-8. ORTEP drawing of **4c** (100 K) seen along the: (a) O–Fe–O and (b) N–Fe–N axis, showing the thermal ellipsoids at the 50% probability level. Hydrogen and counter anion atoms are omitted for clarity.

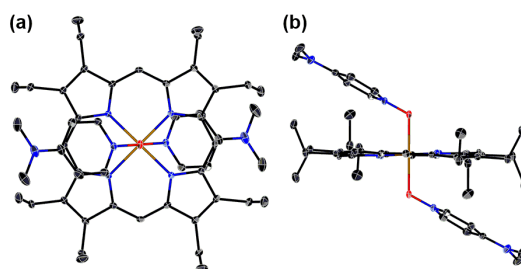


Figure 2-9. ORTEP drawing of **4e** (100 K) seen along the: (a) O–Fe–O and (b) N–Fe–N axis, showing the thermal ellipsoids at the 50% probability level. Hydrogen, solvent, and counter anion atoms are omitted for clarity.

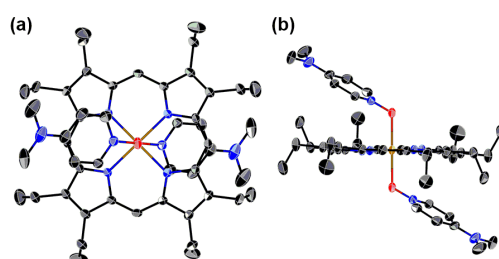


Figure 2-10. ORTEP drawing of **4e** (300 K) seen along the: (a) O–Fe–O and (b) N–Fe–N axis, showing the thermal ellipsoids at the 30% probability level. Hydrogen, solvent, and counter anion atoms are omitted for clarity.

2.3.2. SQUID Magnetometry

Magnetic behaviors were examined by SQUID magnetometry for the microcrystalline samples in 2-300 K range as shown in Figure 2-11. While **1a** and **1b** maintained the $S=5/2$ state above 50 K, all the other complexes showed clear decrease in μ_{eff} values at lower temperature. At 50 K, the μ_{eff} values for **1c**, **1d**, and **1e** reached 3.0, 2.5, and 1.9 μ_{B} , respectively, indicating that not only **1e** but also **1c** and **1d** exhibited the spin-crossover between high spin $S=5/2$ and low spin $S=1/2$ state in the solid state. The μ_{eff} values in **1f** were smoothly decreased from 5.2 to 4.8 μ_{B} in the range of 50 – 300 K, which showed the beginning of spin-crossover phenomenon between $S=5/2$ and $S=1/2$ states.

Figure 2-12 also shows the temperature dependence of the μ_{eff} of powdered **1e**, **2e**, and **3e** between 2 and 300 K. Stepwise decrease of μ_{eff} at 300 K on going from **1e** (4.2 μ_{B}) to **3e** (3.2 μ_{B}), and then to **2e** (2.5 μ_{B}) indicate that spin states of iron(III) ion become from a mixed $S=5/2$ and $1/2$ state to a pure $S=1/2$ state depending on the porphyrin ring-periphery substituents. In the case of TPFPP, the *meso*-pentafluorophenyl groups affect the electron deficient of the porphyrin ring, which increased the coordination ability of axial ligands to iron(III) ion. Therefore, the μ_{eff} in **2e** maintained a low spin $S=1/2$ state over a wide range of temperature.

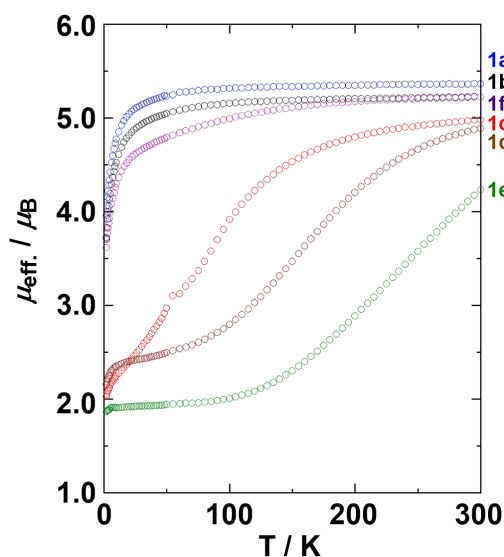


Figure 2-11. Temperature dependence of the effective magnetic moments of **1a** (blue), **1b** (black), **1c** (red), **1d** (brown), **1e** (green), and **1f** (purple) taken for micro-crystalline samples by SQUID magnetometry.

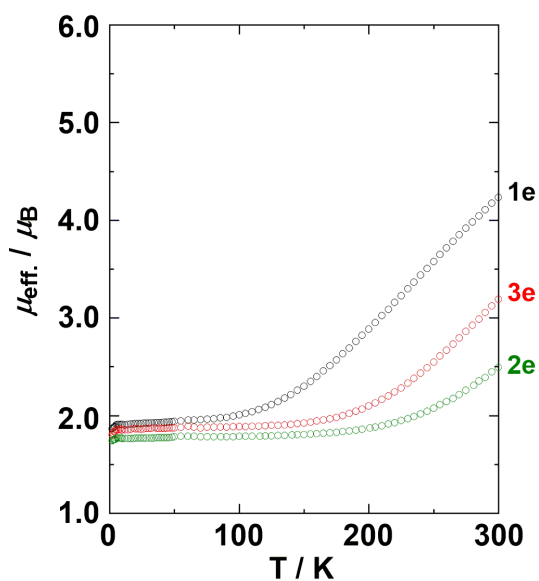


Figure 2-12. Temperature dependence of the effective magnetic moments of **1e** (black), **2e** (green), and **3e** (red) taken for micro-crystalline samples by SQUID magnetometry.

As shown in Figure 2-13, the magnetic property of **4c** and **4e** in solid state has been measured by SQUID magnetometry for the microcrystalline sample at 2–300 K. The μ_{eff} values for **4c** were maintained at 5.6 μ_B in the range 100–300 K, corresponding to the high spin $S=5/2$ state values. Although, the powdered **4e** was 5.0 μ_B such as the nearly $S=5/2$ at 300 K, this sample showed a smooth drop of μ_{eff} value, and reached a value of 2.2 μ_B at 2.0 K. This result indicated that **4e**

adopt the mixed $S = 5/2$ and $1/2$ state with spin-crossover phenomenon over 2–300 K despite the bearing two 4-NMe₂PyNO as the axial ligands. These results are thought to be the cause of the difference of the steric hindrance and the electron property of ring-periphery substituents: such as pyrrole- β substituted porphyrins (OEP) and *meso*-substituted aryl porphyrin (TMP, TPP, and TPFPP).

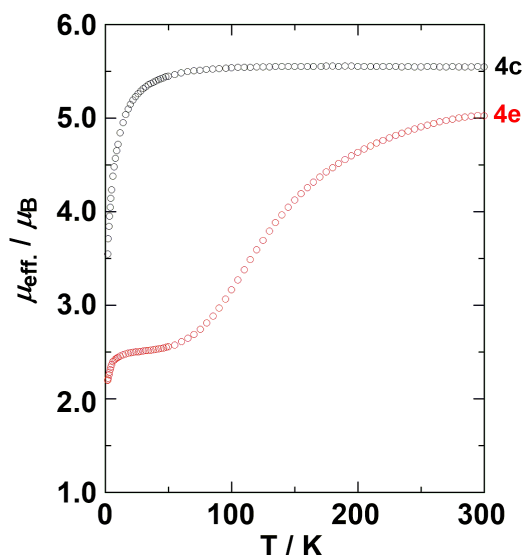


Figure 2-13. Temperature dependence of the effective magnetic moments of **4c** (black) and **4e** (red) taken for micro-crystalline samples by SQUID magnetometry.

2.3.3 Mössbauer spectra

As mentioned, six coordinate iron(III) porphyrin complexes with neutral oxygen ligands usually adopt $S = 5/2$ or a mixed $S = 5/2$ and $3/2$ state. Under very limited conditions, the complex can adopt the $S = 3/2$ state. In order to reveal if the spin-crossover from the $S = 5/2$ to the $S = 1/2$ state proceeds via the $S = 3/2$ state, the author has measured the Mössbauer spectra of **1e** at several temperatures between 294 and 78K. As shown in Figure 2-14 (a) and (b), the sample contained small amount of high-spin impurity. The major species showed extensive broadening as the temperature was lowered probably due to the paramagnetic relaxation. Although the author is unable to fully interpret the Mössbauer spectra of the major component at this point, the spectral change seems to be consistent with the direct transition from the $S = 5/2$ to the $S = 1/2$ state since the QS values never exceeded 3.0 mm s^{-1} throughout the temperature range examined [24,25]. The IS and QS values of the major component at 78 K were 0.28 and 2.52 mm s^{-1} , showing the low-spin state with the $(d_{xy})^2(d_{xz}, d_{yz})^3$ electron configuration.

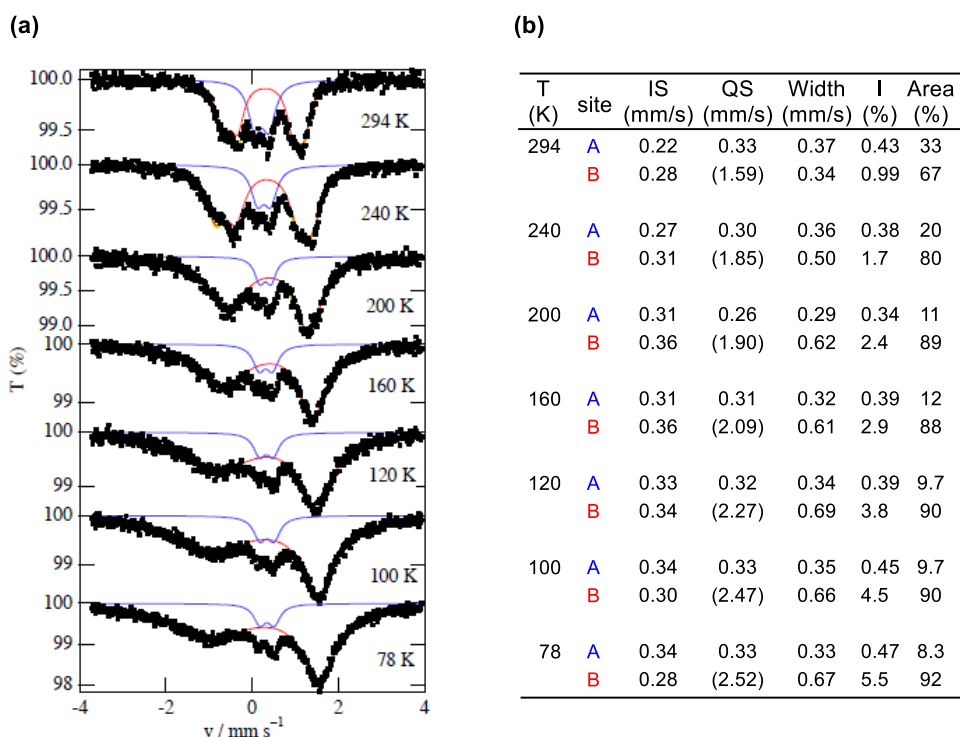


Figure 2-14. ^{57}Fe Mössbauer spectra (a) and parameters (b) of **1e** taken for a microcrystalline sample. taken for micro-crystalline samples by SQUID magnetometry.

2.3.4 ESR Spectra

To obtain further information on the magnetic behaviors in solution, the author has measured the ESR spectra in the microcrystalline samples at 4 K and in frozen CH_2Cl_2 -toluene solutions at 15 K. As shown in Figure 2-15(a) and (b), the ESR spectra differed considerably among complexes depending on the substituents of the axial ligands. In both of solid and solution states, while **1a** and **1b** showed axial type spectra with $g_{\perp} = 5.9$ - 5.7 and $g_{\parallel} = 2.0$ as in the case of $S=5/2$ $[\text{Fe}(\text{TPP})(\text{PyNO})_2]^+$ reported in previous paper by Hoshino et al.[14], **1e** exhibited the rhombic type spectra where three signals were observed at $g_1 = 2.4$, $g_2 = 2.2$, and $g_3 = 1.9$. As revealed from the previous studies, there are two types of electronic ground states in low-spin iron(III) porphyrin complexes, $d\pi$ -type (2E_g state) and d_{xy} -type (${}^2B_{2g}$ state) [9,26-29]. The unpaired electron is in one of the $d\pi$ (d_{xz} or d_{yz}) orbitals in the former case while it is in the d_{xy} orbital in the latter one. The ESR spectra of these two types of low-spin complexes are quite different. While the $d\pi$ -type complexes exhibit either rhombic spectra as in the present case or large g_{max} spectra as in the case of bis-cyanide complexes, the d_{xy} -type complexes exhibit axial spectra where the g_{\perp} value is less than 2.6 [26]. Thus, it is clear that **1a** and **1b** adopt the high spin $S = 5/2$ state while **1e** adopts the $d\pi$ -type low spin $S=1/2$ state with a $(d_{xy})^2(d_{xz}, d_{yz})^3$ electron configuration. However,

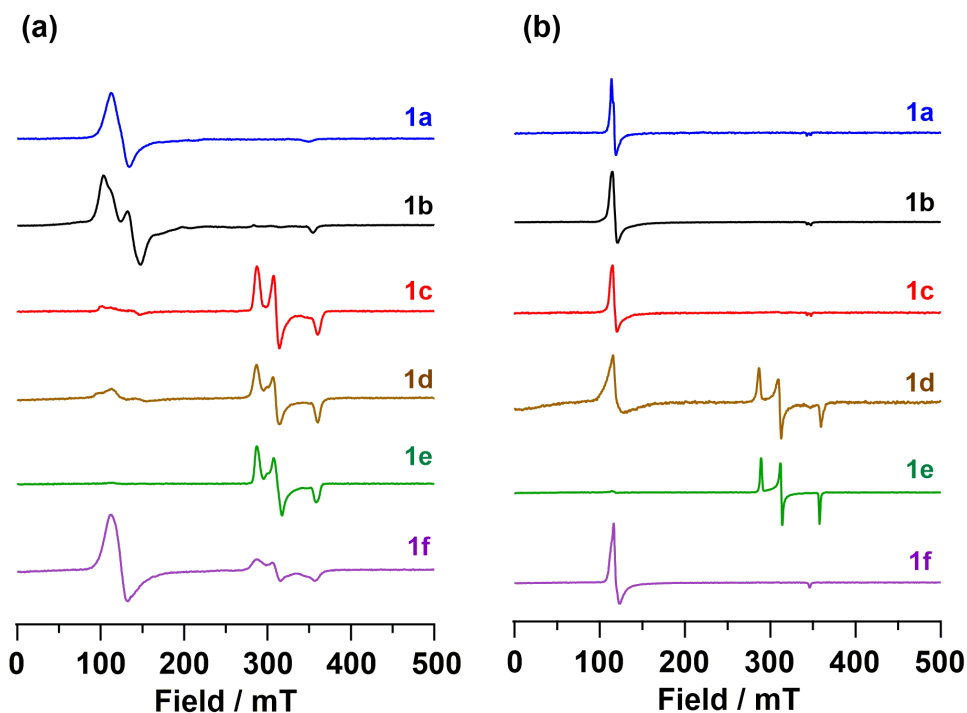


Figure 2-15. EPR spectra of **1a-1f** taken (a) in the solid state at 4 K and (b) in frozen CH_2Cl_2 -toluene solutions at 15 K.

the ESR spectra of **1c**, **1d**, and **1f** were different from those between solid and solution states. While the ESR spectra of **1c** and **1f** showed only axial type signals characteristic of the high spin $S = 5/2$ state in solution, the same complexes exhibited mostly the rhombic and the axial type signals in solid state, respectively. In the case of **1d**, both the axial with $g_{\perp} = 5.7$ and $g_{\parallel} = 2.0$ and the rhombic signals with $g_1 = 2.4$, $g_2 = 2.2$, and $g_3 = 1.9$ coexisted for the both of solid and solution states. The results clearly indicate that **1d** exists as an equilibrium mixture given by eqn. (1): in frozen CH_2Cl_2 -toluene solution at 15 K.

High spin state ($S = 5/2$) \rightleftharpoons Low spin state ($S = 1/2$) (1)

These result suggests that the low spin $S=1/2$ state is stabilized in the solid probably due to the crystal packing force [30]. Therefore, it is quite unusual that **1e** adopts the quite pure $S=1/2$ state with a $(d_{xy})^2(d_{xz}, d_{yz})^3$ electron configuration at 15 K in spite of the coordination of neutral oxygen ligand and solution state.

Figure 2-16 (a) and (b) show the ESR spectra of **2e** and **3e** with 4-NMe₂PyNO as the axial ligand in both of solid and solution state. The ESR spectra of **2e** and **3e** exhibited the rhombic signals with $g_1 = 2.37$ and 2.39, $g_2 = 2.19$ and 2.21, and $g_3 = 1.95$ and 1.93 in solid state at 4 K, and also showed three signals with $g_1 = 2.42$ and 2.41, $g_2 = 2.19$ and 2.21, and $g_3 = 1.95$ and 1.93 in solid state at 4 K, respectively. These values indicated that **2e** and **3e** also adopts the quite pure $d\pi$ -type low spin $S = 1/2$ state with a $(d_{xy})^2(d_{xz}, d_{yz})^3$ electron configuration in both of solid and solution states.

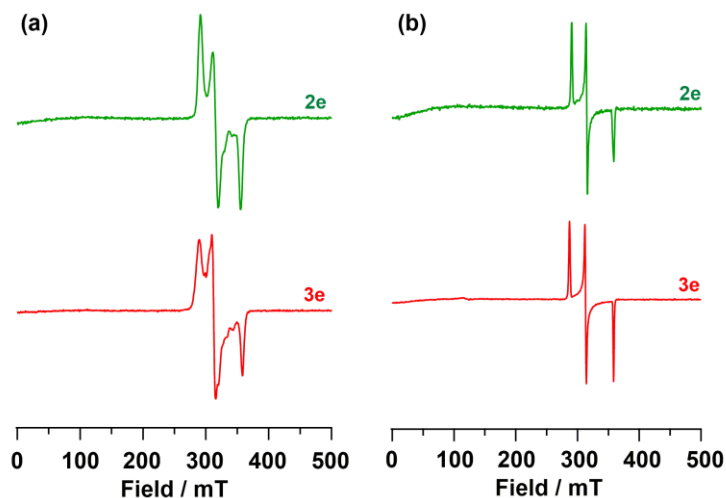


Figure 2-16. ESR spectra of **2e** and **3e** taken (a) in the solid state at 4 K and (b) in frozen CH₂Cl₂-toluene solutions at 15 K.

Figure 2-17 shows the ESR spectra of **4c** and **4e** bearing OEP as the macrocycle skeleton in frozen CH₂Cl₂-toluene solution at 15 K. The ESR spectrum of **4c** with 4-MePyNO exhibited the axial type signals with $g_{\perp} = 5.78$ and $g_{\parallel} = 2.00$, which also indicates that **4c** maintains a pure high spin $S = 5/2$ state. On the other hand, the ESR spectrum of **4e** with 4-NMe₂PyNO exhibited both the axial with $g_{\perp} = 5.73$ and $g_{\parallel} = 1.99$ and the rhombic signals with $g_1 = 2.41$, $g_2 = 2.21$, and $g_3 = 1.93$ coexisted. This result indicated that **4e** also adopts the mixed $S = 5/2$ and $1/2$ states in solution at 15 K in spite of the using two 4-NMe₂PyNO with the high affinity to iron(III) ion.

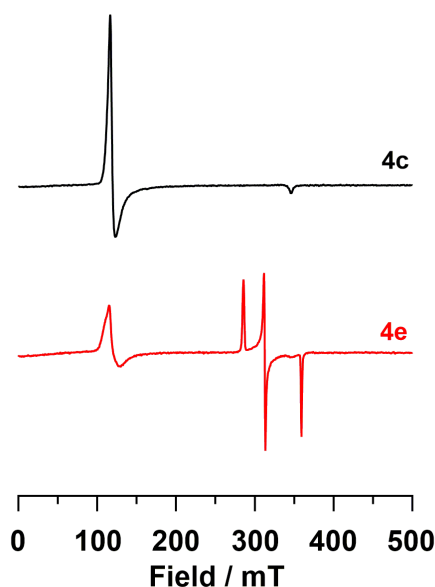


Figure 2-17. EPR spectra of **4c** and **4e** taken in frozen CH₂Cl₂-toluene solutions at 15 K.

2.3.5 NMR Spectral Study

^1H NMR spectra of **1a–1f** shown in Figure 2-18 were taken in CD_2Cl_2 solution at 298 and 183 K. Figure 2-19 shows the Curie plots of the pyrrole-H signals for **1a–1f**. The pyrrole-H signals for **1a–1d** and **1f** exhibited good linearity. The large downfield shifts, 60–70 ppm at 298 K, together with positive slopes clearly indicate that these complexes adopt the high spin $S = 5/2$ state [14]. In contrast, the Curie plots of the pyrrole-H signals in **1e** carrying an electron donating dimethylamino ($-\text{NMe}_2$) group showed a curvature with a negative slope. The pyrrole-H signals observed at 57.4 ppm at 298 K for **1e** moved to 34.5 ppm at 183 K. The result indicates that the

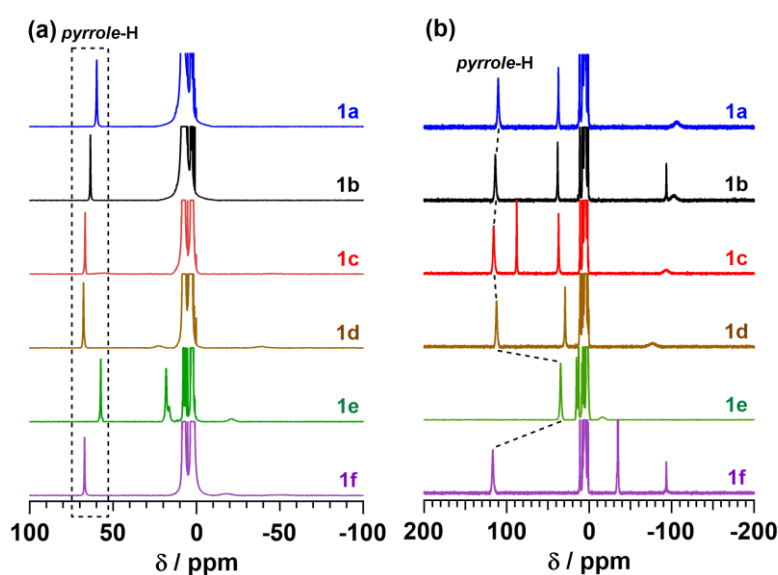


Figure 2-18. ^1H NMR spectra of **1a–1f** taken in CD_2Cl_2 solutions at (a) 298 K and (b) 183 K.

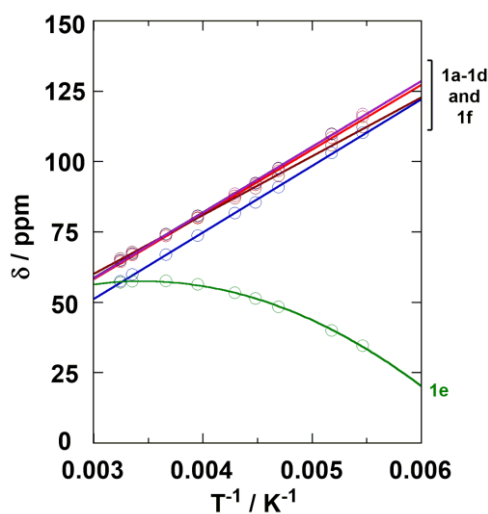


Figure 2-19. Curie plots of the pyrrole-H signals of **1a** (blue), **1b** (black), **1c** (red), **1d** (brown), **1e** (green), and **1f** (purple) taken in CD_2Cl_2 solutions.

contribution of a high spin $S = 5/2$ state decreased with decreasing temperature. The solution magnetic moments (μ_{eff}) determined by the Evans method in the same temperature range for **1a**–**1e** are given in Figure 2-20 [16]. While the μ_{eff} values of **1a**–**1d** were maintained at 5.3–5.8 μ_{B} , those of **1e** showed a large decrease as the temperature was lowered; from 4.7 μ_{B} at 298 K to 3.4 μ_{B} at 183 K. The results suggest that **1e** exhibits a spin-crossover phenomenon in CD_2Cl_2 solution between high spin $S = 5/2$ and low spin $S = 1/2$ states as shown in eqn. (1).

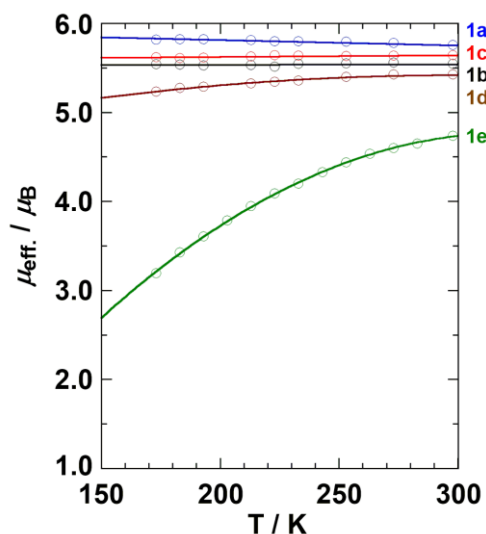


Figure 2-20. Temperature dependence of the effective magnetic moments of **1a** (blue), **1b** (black), **1c** (red), **1d** (brown), and **1e** (green) taken in CH_2Cl_2 solutions by the Evans method at

To obtain further remarkable information on the spectroscopic and magnetic properties behaviors, I measured the ^1H NMR variable-temperature measurements for the six-coordinate iron(III) *meso*-tetraarylporphyrin complexes with two 4- NMe_2PyNO molecules **2e** and **3e**. Figure 2-21 exhibited the ^1H NMR spectra of **2e** and **3e** taken in CD_2Cl_2 solution at 298 and 183 K. Figure 2-22 also shows the Curie plots of the *pyrrole*-H signals for **1e**, **2e**, and **3e**, which exhibited a curvature with a negative slope. In particular, *pyrrole*-H signal for **2e** showed the most upfield-shifted at the lower temperature. The *pyrrole*-H signals observed at 24.1 (**2e**) and 55.3 ppm (**3e**) at 298 K moved to -10.2 (**2e**) and 22.3 ppm (**3e**) at 183 K. The results indicate that the contribution of a low spin $S = 1/2$ state increased with lower temperature. In addition, the solution magnetic moments (μ_{eff}) determined by the Evans method in the same temperature range for **1e**, **2e**, and **3e** are given in Figure 2-23 [16]. The μ_{eff} values of **2e** and **3e** showed a large decrease as the temperature was lowered; from 3.7 (**2e**) and 5.0 μ_{B} (**3e**) at 298 K to 2.2 (**2e**) and 3.2 μ_{B} (**3e**) at 183 K. The results suggest that the aryl substituents at *meso*-position in macrocycle are arranged in descending order of the pyrrole shifts and the solution magnetic moments, which indicated that the low spin $S=1/2$ contribution increases on going from TMP to TPP, and then to TPFPP.

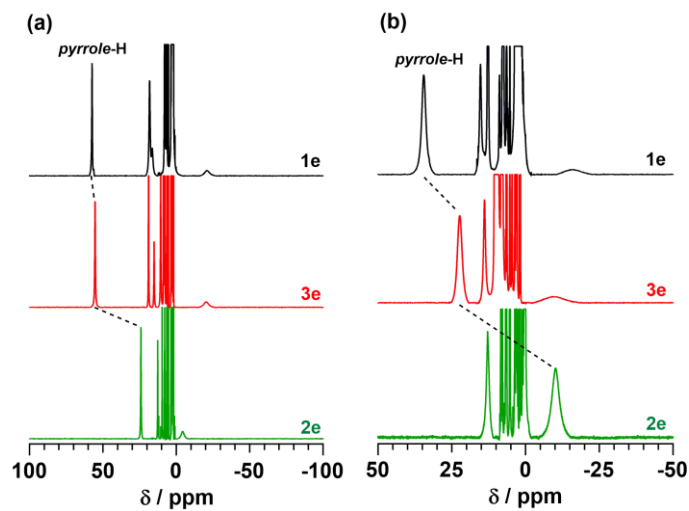


Figure 2-21. ^1H NMR spectra of **1e**, **2e**, and **3e** taken in CD_2Cl_2 solutions at (a) 298 K and (b) 183 K.

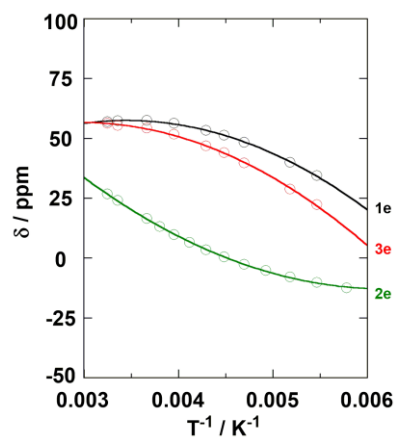


Figure 2-22. Curie plots of the pyrrole-H signals of **1e** (black), **2e** (green), and **3e** (red) taken in CD_2Cl_2 solutions.

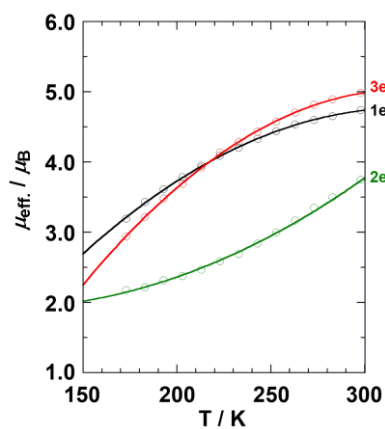


Figure 2-23. Temperature dependence of the effective magnetic moments of **1e** (black), **2e** (green), and **3e** (red) taken in CH_2Cl_2 solutions by the Evans method at 173–298 K.

The curvature in the Curie plots of **1e**, **2e**, and **3e** shown in Figure 2-22 can then be explained in terms of the spin-crossover from the high spin $S = 5/2$ to the low spin d_{π} -type $S = 1/2$ state with decreasing temperature. The difference in the magnetic behaviors in **1e**, **2e**, and **3e** as compared with those in **1a–1d** and **1f** should be ascribed to the strong electron donating dimethylamino group in the former complexes, which should raise the energy level of the d_{z^2} orbital and consequently stabilize the low-spin state. The facts that **2e** showed a pyrrole-H signal at -10.2 ppm at 183 K together with the effective magnetic moment of $2.22 \mu_B$ at the same temperature suggest that the complex adopts mainly the d_{π} -type low-spin state at 183 K. Thus, the electron withdrawing group at the *meso* positions stabilizes the d_{π} -type rather than the d_{xy} -type low spin state. This is consistent with our previous results showing that the d_{xy} -type low spin state is stabilized by the electron donating *meso* substituents [29]. The Curie plots in Figure 2-22 and the temperature dependence of the effective magnetic moments in Figure 2-23 clearly indicate that the population of the low spin state is much larger in **2e** than in **1e** and **3e**, indicating that the electron withdrawing substituents at the *meso* positions stabilize the low spin state. It is expected that the coordination strength of the porphyrin ring is weakened by the electron withdrawing groups at the *meso* positions. Consequently, the axial coordination should be strengthened, which stabilizes the low spin state.

In principle, thermodynamic parameters corresponding to the spin-crossover process of **1e** could be obtained from the Curie plots given in Figure 2-22 since the equilibrium constant in eqn. (1) is expressed by eqn. (2), where δ_{obs} , δ_{HS} , and δ_{LS} are the chemical shifts of the *pyrrole*-H signals in **1e** and the corresponding high spin and low spin complexes, respectively:

$$K = [S = 1/2] / [S = 5/2] = (\delta_{\text{HS}} - \delta_{\text{obs}}) / (\delta_{\text{obs}} - \delta_{\text{LS}}) \quad (2)$$

The author used the *pyrrole*-H chemical shifts of **1b** and $[\text{Fe}(\text{TMP})(\text{Py})_2]^+$ as δ_{HS} and δ_{LS} in eqn. (2) [31], respectively, and determined the K value at each temperature. Figure 2-24 shows the van't Hoff plots, from which the thermodynamic parameters were calculated to be $\Delta H^\circ = -9.7 \text{ kJ mol}^{-1}$ and $\Delta S^\circ = -48 \text{ J mol}^{-1} \text{ K}^{-1}$. A similar treatment was applied to **2e** to yield ΔH° and ΔS° values of -13 kJ mol^{-1} and $-40 \text{ J mol}^{-1} \text{ K}^{-1}$, respectively. The negative ΔH° values are consistent with a general tendency that the Fe–ligand bond in a low-spin complex is much stronger than that in the corresponding high-spin complex as is revealed from the shorter bond lengths in the low-spin complex [31]. The negative ΔS° values can then be explained in terms of the restriction of the internal motion such as the rotation around the Fe–O bond.

Although there are ample examples on the spin-crossover of this type as exemplified by methemoglobin, metmyoglobin, and their model complexes, they commonly have nitrogen bases as axial ligands [1-5,26-29]. The only exception is low-spin $[\text{Fe}(\text{TPP})(\text{OMe})(\text{OO}^t\text{Bu})]^-$ reported by Rivera and coworkers. However, this complex has two anionic ligands and is considered to

adopt the $(d_{xz}, d_{yz})^4(d_{xy})^1$ electron configuration at 193 K [31]. Thus, this is the first example of the spin-crossover in solution between high spin $S = 5/2$ and low spin $S = 1/2$ states in iron(III) porphyrin complexes with neutral oxygen ligands at the axial position.

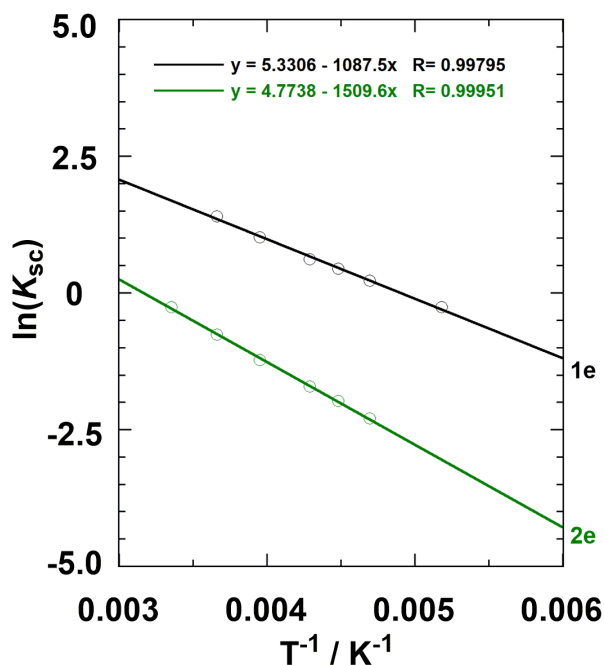
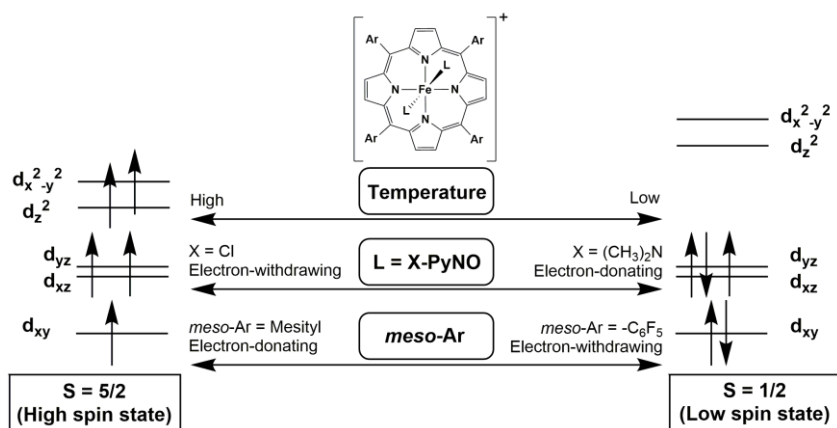


Figure 2-24. Van't Hoff plots for 1e (black) and 2e (green).

2.4 Conclusion

In conclusion, the spin-crossover phenomenon in iron porphyrin complexes has attracted much attention of chemists and biochemists who are working to reveal the functions and catalytic processes of heme proteins as well as their model complexes. As an extension of our work on seeking for the new spin-crossover system, the author have examined the electronic, magnetic, and structural properties of iron(III) *meso*-tetramesitylporphyrin cation complexes $[\text{Fe}(\text{TMP})\text{L}_2]^+$, *meso*-tetra(perfluorophenyl)porphyrin cation complex $[\text{Fe}(\text{TPFPP})\text{L}_2]^+$, *meso*-tetraphenylporphyrin cation complex $[\text{Fe}(\text{TPP})\text{L}_2]^+$, octaethylporphyrin cation complexes $[\text{Fe}(\text{OEP})\text{L}_2]^+$ *para*- or *meta*-substituted pyridine *N*-oxides ($\text{L} = 4\text{-XPyNO}$ or $3,5\text{-Me}_2\text{PyNO}$; $\text{X} = \text{Cl}, \text{H}, \text{Me}, \text{OMe}, \text{NMe}_2$) as axial ligands. Among them, molecular structures of some sample were determined by X-ray crystallography at 100 K. In each complex, the porphyrin ring is almost planar and the iron(III) ion is located within the porphyrin plane perfectly. In the case of a series of $[\text{Fe}(\text{TMP})\text{L}_2]^+$, stepwise decrease of both Fe- N_p and Fe-O bonds on going from $[\text{Fe}(\text{TMP})(4\text{-ClPyNO})_2]^+$ and $[\text{Fe}(\text{TMP})(3,5\text{-Me}_2\text{PyNO})_2]^+$ to $[\text{Fe}(\text{TMP})(4\text{-MePyNO})_2]^+$, and then to

$[\text{Fe}(\text{TMP})(4\text{-NMe}_2\text{PyNO})_2]^+$ indicate the removal of an electron from both $d_{x^2-y^2}$ and d_z^2 orbitals due to the destabilization of the corresponding d orbitals, which in turn indicates that $[\text{Fe}(\text{TMP})(4\text{-ClPyNO})_2]^+$ adopts the $S = 5/2$ state while $[\text{Fe}(\text{TMP})(4\text{-NMe}_2\text{PyNO})_2]^+$ adopt the $S = 1/2$ state at 100 K. In addition, both the average Fe–N_p and Fe–O lengths in $[\text{Fe}(\text{TMP})(4\text{-MePyNO})_2]^+$ have increased by 0.019 and 0.047 Å, respectively, when the temperature is raised to 300 K. As the models for the prosthetic group in heme proteins, structures of six-coordinate $[\text{Fe}(\text{OEP})(4\text{-MePyNO})_2]^+$ and $[\text{Fe}(\text{OEP})(4\text{-NMe}_2\text{PyNO})_2]^+$ were confirmed by the single-crystal X-ray analysis. Both the average Fe–N_p and Fe–O lengths are thought to be the cause of the difference of the field strength of axial ligands and the steric hindrance and the electron property of ring-periphery substituents. As the general tendency, the six-coordinate iron(III) porphyrin complexes with neutral oxygen ligands adopt a high-spin state in a wide range of temperature. By using of X-ray crystal structure, SQUID, Mössbauer, ESR, and NMR measurements results, however, the author has found that $[\text{Fe}(\text{TPFPP})(4\text{-NMe}_2\text{PyNO})_2]^+$ is the first example of six-coordinated iron(III) porphyrin that adopts the $S=1/2$ state. Furthermore, some of these complexes have shown spin-crossover phenomenon between high-spin ($S = 5/2$) and low-spin ($S = 1/2$) with a $(d_{xy})^2(d_{xz}, d_{yz})^3$ electron configuration states both in solution and solid states as shown in Scheme 2-2. The difference in the magnetic behaviours in $[\text{Fe}(\text{TMP})(4\text{-NMe}_2\text{PyNO})_2]^+$ and $[\text{Fe}(\text{TPFPP})(4\text{-NMe}_2\text{PyNO})_2]^+$ as compared with those in $[\text{Fe}(\text{TMP})\text{L}_2]^+$ (L = 4-XPyNO or 3,5-Me₂PyNO; X = Cl, H, Me, OMe, NMe₂), should be ascribed to the strong electron donating dimethylamino group in the former complexes, which should raise the energy level of the d_{z^2} orbital and consequently stabilize the low-spin state. In addition, the electron withdrawing group at the *meso* positions stabilizes the d_{π} -type rather than the d_{xy} -type low-spin state. It is expected that the coordination strength of the porphyrin ring is weakened by the electron withdrawing groups at the *meso* positions. Consequently, the axial coordination should be strengthened, which stabilizes the low-spin state.



Scheme 2-2. Spin crossover between $S=5/2$ (high spin state) and $S=1/2$ (low spin state) for these Fe(III) porphyrin complexes.

2.6 References

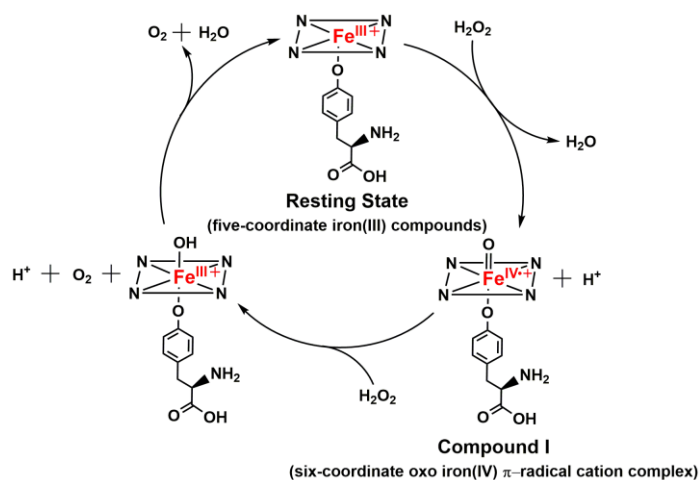
- [1] J. Beetlestone, P. George, *Biochemistry* 1964, 3, 707–714.
- [2] T. Iizuka, M. Kotani, *Biochim. Biophys. Acta* 1969, 194, 351–363.
- [3] S. McCoy, W. S. Caughey, *Biochemistry* 1970, 9, 2387–2393.
- [4] J. O. Alben, L. Y. Fager, *Biochemistry* 1972, 11, 842–847.
- [5] W. R. Scheidt, D. K. Geiger, K. J. Haller, *J. Am. Chem. Soc.* 1982, 104, 495–499.
- [6] T. Ikeue, Y. Ohgo, T. Yamaguchi, M. Takahashi, M. Takeda, M. Nakamura, *Angew. Chem. Int. Ed.* 2001, 40, 2617–2620.
- [7] Y. Ohgo, T. Ikeue, M. Nakamura, *Inorg. Chem.* 2002, 41, 1698–1700.
- [8] T. Ikeue, Y. Ohgo, O. Ongayi, M. Graça. H. Vicente, M. Nakamura, *Inorg. Chem.* 2003, 42, 5560–5571.
- [9] M. Nakamura, *Coord. Chem. Rev.* 2006, 250, 2271–2294.
- [10] A. Ikezaki, M. Takahashi, M. Nakamura, *Angew. Chem. Int. Ed.* 2009, 48, 6300–6303.
- [11] G. A. Caignan, R. Deshmukh, Y. Zeng, A. Wilks, R. A. Bunce, M. Rivera, *J. Am. Chem. Soc.* 2003, 125, 11842–11852.
- [12] M. Rivera and G. A. Caignan, *Anal. Bioanal. Chem.*, 2004, 378, 1464–1483.
- [13] D. Sahoo, M. G. Quesne, S. P. de Visser, S. P. Rath, *Angew. Chem. Int. Ed.* 2015, 54, 4796–4800.
- [14] A. Hoshino, Y. Ohgo, M. Nakamura, *Inorg. Chem.* 2005, 44, 7333–7344.
- [15] Y. Ohgo, A. Hoshino, H. Uekusa, M. Nakamura, *Inorg. Chem. Commun.* 2006, 9, 1183–1186.
- [16] D. F. Evans, T. A. James, *J. Chem. Soc., Dalton Trans.* 1979, 723–726.
- [17] J. T. Groves, R. Quinn, T. J. McMurry, M. Nakamura, G. Lang, B. Boso, *J. Am. Chem. Soc.* 1985, 107, 354–360.
- [18] R. W. Wagner, D. S. Lawrence, J. S. Lindsey, *Tetrahedron Lett.* 1987, 28, 3069–3070.
- [19] C. T. Watson, S. Cai, N. V. Shokhirev, F. A. Walker, *Inorg. Chem.* 2005, 44, 7468–7484.
- [20] M. C. Burla, R. Caliendo, M. Camalli, B. Carrozzini, G. L. Casciarano, C. Giacovazzo, M. Mallamo, A. Mazzone, G. Polidori, R. Spagna, *J. Appl. Cryst.* 2012, 45, 357–361.
- [21] G. M. Sheldrick, *Acta Cryst.* 2015, C71, 3–8.
- [22] Y. Ohgo, T. Saitoh, M. Nakamura, *Acta Cryst.* 2001, C57, 233–234.
- [23] Y. Ohgo, T. Ikeue, M. Takahashi, M. Takeda, M. Nakamura, *Eur. J. Inorg. Chem.* 2004, 798–809.
- [24] P. Gütllich, J. Ensling, *Inorganic Electronic Structure and Spectroscopy* (Eds.: E. I. Solomon, A. B. P. Lever), Wiley, New York, 1999, pp. 161–211.
- [25] M. Nakamura, M. Takahashi, *Mössbauer Spectroscopy* (Eds.: V. K. Sharma, G. Klingelhofer, T. Nishida), Wiley, New York, 2013, pp. 177–201.

- [26] F. A. Walker, *In The Porphyrin Handbook*, Vol. 5, (Eds.: K. M. Kadish, K. M. Smith, R. Guilard), Academic Press, San Diego, CA, 2000, pp. pp 81–183.
- [27] F. A. Walker, H. Nasri, I. Turowska-Tyrk, K. Mohanrao, C. T. Watson, N. V. Shokhirev, P. G. Debrunner, W. R. Scheidt, *J. Am. Chem. Soc.* 1996, 118, 12109–12118.
- [28] M. Nakamura, Y. Ohgo, A. Ikezaki, *In The Porphyrin Handbook*, Vol. 7, (Eds.: K. M. Kadish, K. M. Smith, R. Guilard), Academic Press, San Diego, CA, 2000, pp 1–146.
- [29] A. Ikezaki, T. Ikeue, M. Nakamura, *Inorg. Chim. Acta*, 2002, 335, 91–99.
- [30] M. K. Safo, G. P. Gupta, C. T. Watson, U. Simonis, F. A. Walker, W. R. Scheidt, *J. Am. Chem. Soc.* 1992, 114, 7066–7075.
- [31] M. Rivera, G. A. Caignan, A. V. Astashkin, A. M. Raitsimring, T. K. Shokhireva, F. A. Walker, *J. Am. Chem. Soc.* 2002, 124, 6077–6089.

3 Synthesis of Oxo-Iron(IV) Porphyrin π -Radical Cation Complex with Pyridine N-Oxide Derivative

3.1 Introduction

The word “cytochrome” was coined more than 100 years ago, in 1884 by McMunn, to describe the colored substances in cells [1]. Later, many of these “cytochromes” were found to contain hemes, that is to say, porphyrins complexed to iron [2,3]. The active centers in heme proteins such as cytochrome P450, peroxidase, and catalase have a very important function of electron transfer and enzyme by the difference of axial ligands [4-7]. For example, the active center of cytochrome P450 consists of the heme with cysteine molecule as axial ligand having sulfur coordination site. Similarly, one of peroxidase and catalase consist of the heme with histidine and tyrosine residues bearing nitrogen and oxygen coordination sites, respectively. When the active site of peroxidase and catalase are activated by peroxides or peracids, they form an oxo iron(IV) porphyrin π -radical cation intermediate called Compound I [8-10]. Scheme 3-1 shows the catalyst cycle of the active center in catalase. There are the axial ligand exchange binding to the iron porphyrin and the change of oxidation number for iron ions. Compound I is also believed to be an active intermediate in the reactions of oxygenases such as cytochrome P450 [11-14]. The compound I in cytochrome P450 directly transfers a single oxygen atom to a variety of substrates. It is generally accepted that the diverse functions of compound I are controlled by heme environmental structures, such as porphyrin peripheral structures, heme axial ligands, and protein structures around heme. Therefore, elucidation of the electronic structures in a variety of iron porphyrin complexes as model compounds is quite important to understand the function and catalytic



Scheme 3-1. Catalyst cycle of active center in catalase.

processes of naturally occurring heme proteins. Although the model compound of Compound I with the very high reactivity in catalytic cycle attracts an interest of many scientists, there are only a few literatures. The formation of an oxo iron(IV) porphyrin π -radical cation complex was first reported by J. T. Groves et al. in 1981, by the oxidation of five-coordinate chloro iron(III) *meso*-tetramesitylporphyrin (TMP) with *m*-chloroperbenzoic acid (*m*-CPBA) at 195 K [14]. The obtained green compound was characterized as an oxo iron(IV) TMP π -cation radical complex, $[\text{O}=\text{Fe}^{\text{IV}}(\text{TMP})^+]$, like compounds-I of peroxidases and catalases. Recently, instead of *m*-CPBA, O_3 or dimethyldioxirane can also be used to prepare the oxo iron(IV) porphyrin π -radical cation complex from iron(III) porphyrin complexes [15-18]. Furthermore, the author reported the electronic, magnetic, and structural properties of six-coordinate iron(III) TMP complexes bearing suitably substituted pyridine *N*-oxides, as precursors of the model compound in catalase active center with tyrosine molecules [19]

In this research, the synthesis and characterization of five-coordinate iron(III) TMP complex with one 4-dimethylaminopyridine *N*-oxide (4-NMe₂PyNO) $[\text{Fe}^{\text{III}}(\text{TMP})(4\text{-NMe}_2\text{PyNO})]\text{ClO}_4$ as the precursor of high-valent oxo iron porphyrins in synthetic model systems are summarized. The author also synthesized oxo iron(IV) porphyrin π -radical cation complex, six-coordinate $[\text{O}=\text{Fe}^{\text{IV}}(\text{TMP})(4\text{-NMe}_2\text{PyNO})]\text{ClO}_4$. The electronic structure and spectroscopic property of oxo iron(IV) porphyrin π -radical cation complex will be discussed in detail.

3.2 Experimental Section

3.2.1 Instrumentation

Elemental Analyses for carbon, hydrogen, and nitrogen were conducted using a Yanako CHN CORDER MT-6. UV-Vis absorption spectra were recorded in CH_2Cl_2 solution on a Shimadzu UV-3100 spectrometer. ¹H NMR spectra were recorded on a JEOL delta ECX-500 spectrometer operating at 500.1 MHz. Chemical shifts for ¹H NMR spectra were referenced to CH_2Cl_2 ($\delta = 5.32$ ppm). Mass spectra were recorded on a Bruker micrOTOF using positive mode ESI-TOF method for acetonitrile solutions by using sodium formate as reference. Unless otherwise noted, materials obtained from commercial suppliers were used without further purification. ESR spectra were recorded on a Bruker E500 spectrometer operating at the X band and equipped with an Oxford helium cryostat. The *g*-values were determined by the simulation of observed spectra. The simulation spectra were obtained by using EasySpin software package [20]. The solid-state magnetic susceptibilities were measured between 2 and 300 K under a magnetic field of 0.5 T with the SQUID magnetometers (Quantum Design MPMS-7 and MPMS-XL7).

3.2.2 Syntheses and Complex Data

3.2.2.1 Synthetic procedure

The general synthetic procedures were carried out according to previous literatures [14]. Free base porphyrin $H_2(TMP)$ was prepared by the Lindsey methods [21]. The corresponding iron(III) complexes $[Fe(TMP)Cl]$ were also prepared by the literature methods [22]. The iron(III) chloride porphyrin complexes were converted to the perchlorate complexes by the reaction with $AgClO_4$ (2 eq.) in dehydrated THF solution. The crude solid was purified by the recrystallization from CH_2Cl_2 , THF and *n*-hexane. The five-coordinate iron(III) porphyrin complex $[Fe^{III}(TMP)(4-NMe_2PyNO)]ClO_4$ were obtained at ambient temperature by the addition of 4-dimethylamino- pyridine *N*-oxide (4-NMe₂PyNO: 1.0 eq.) as axial ligand into a CH_2Cl_2 solution containing the perchlorate complexes $Fe(Por)ClO_4$. Analytically pure solid sample was obtained by recrystallization from CH_2Cl_2 / hexane mixed solvent solution, which was identified by ¹H NMR, UV-Vis, ESI-TOF-Mass, and elemental analyses measurements. Figure 3-1 shows the UV-Vis spectrum of five-coordinate iron(III) complex $[Fe^{III}(TMP)(4-NMe_2PyNO)]ClO_4$ taken in CH_2Cl_2 solution, and Figure 3-2 also exhibits the result of ESI-TOF-Mass spectrum. In addition, spectroscopic and magnetic properties were investigated by variable-temperature ¹H NMR, ESR, and SQUID measurements.

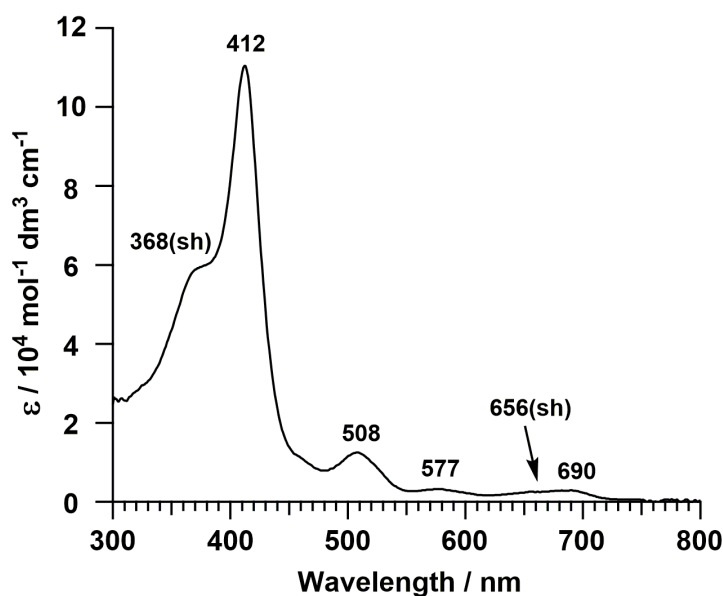


Figure 3-1. UV-Vis spectrum of five-coordinate $[Fe^{III}(TMP)(4-NMe_2PyNO)]ClO_4$ taken in CH_2Cl_2 solution.

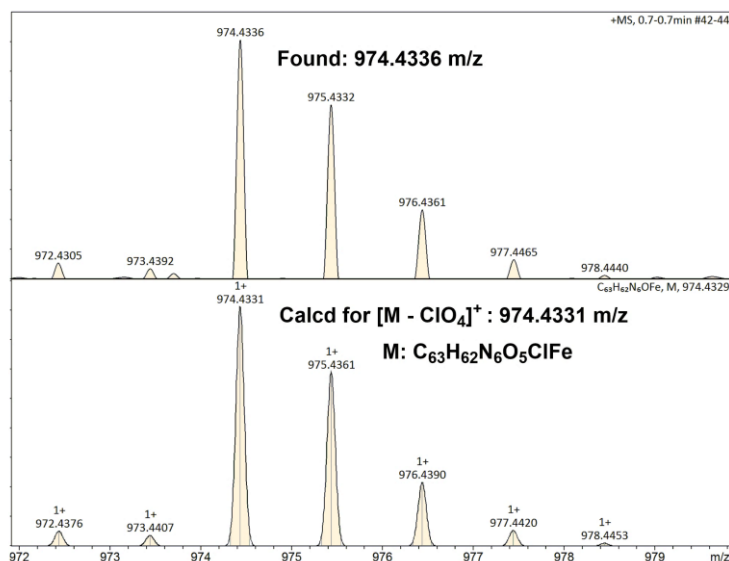
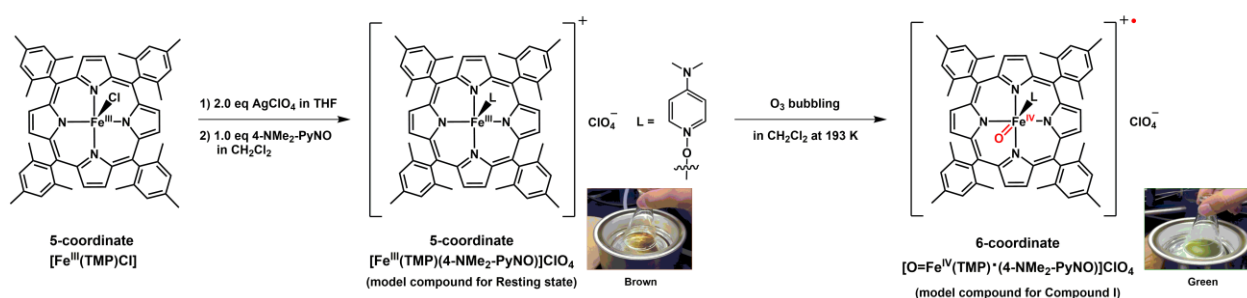


Figure 3-2. ESI-TOF-Mass spectrum of five-coordinate $[Fe^{III}(TMP)(4-NMe_2PyNO)]ClO_4$ taken in acetonitrile solution for positive mode.

The synthesis of six-coordinate oxo iron(IV) porphyrin π -radical cation complex was carried out according to reported methods [13]. Under the low temperature of 193 K, the solution of five-coordinate iron(III) porphyrin complex $[Fe^{III}(TMP)(4-NMe_2PyNO)]ClO_4$ in CH_2Cl_2 changed from the brown color to the green color by the bubbling of O_3 , resulting in the six-coordinate oxo iron(IV) porphyrin π -radical cation complex as shown in Scheme 3-2. The obtained $[O=Fe^{IV}(TMP)\cdot(4-NMe_2PyNO)]ClO_4$ was identified by the ESR measurement at 15 K.



Scheme 3-2. Synthetic scheme of six-coordinate oxo iron(IV) porphyrin π -radical cation complex.

3.2.2.2 Analytical and spectroscopic data for five-coordinate iron(III) porphyrin complex [Fe^{III}(TMP)(4-NMe₂PyNO)]ClO₄

This complex was obtained as a brown solid. Anal. Found: C, 70.05; H, 5.71; N, 7.67 %, Calcd. for C₆₃H₆₂N₆O₅ClFe: C, 70.42; H, 5.82; N, 7.82 %. ¹H NMR (CD₂Cl₂, 500 MHz, 298 K): δ = 65.1 (*pyrrole*-H, 8H), 34.2 (L: *p*-NMe₂, 6H), 21.0 (L: *m*-H, 2H), 13.9 (Mes: *m*-H, 4H), 12.7 (Mes: *m*-H, 4H), 6.1 (Mes: *o*-Me, 12H), 4.2 (Mes: *p*-Me, 12H), 2.6 (Mes: *o*-H, 12H), and -26.3 ppm (L: *o*-H, 2H). UV-Vis (CH₂Cl₂): λ_{\max} (ϵ : 10⁴ mol⁻¹ dm³ cm⁻¹) = 368 (sh, 5.8), 412 (11.0), 508 (1.2), 577 (0.3), 656 (sh, 0.3), and 690 nm (0.3). HR-MS (ESI-TOF, CH₃CN, positive): Found: 974.4336 m/z; Calcd. for C₆₃H₆₂N₆OFe ([M - ClO₄]⁺) = 974.4331 m/z. EPR (frozen CH₂Cl₂-toluene, 15 K): g₁ = 5.79, g₂ = 5.79, g₃ = 2.00; (solid, 4 K): g₁ = 5.52, g₂ = 5.52, g₃ = 1.99. SQUID (solid, 300 K): μ_{eff} = 5.3 μ_{B} .

3.2.3 X-ray Crystallographic structure solution and refinement

Crystals suitable for X-ray structure analysis were obtained from CH₂Cl₂ / toluene / *n*-hexane mixed-solvent solutions. X-ray measurements of the single crystals were done with Rigaku VariMax Saturn-724 (1.2 kW Mo rotating anode) at 100 K. Single crystals for X-ray analysis were obtained by the diffusion method. X-ray diffraction data were processed using Crystal Clear 1.6.3 followed by CrystalStructure Ver. 4.2.2. Structures were solved from the processed data using SIR 2011 program package, and then refined by SHELXL-2014/7 program package [23,24]. Final structures were validated by Platon CIF check. Copies of the information may be obtained free of charge from: The Director, CCDC, 12 Union Road, Cambridge, CB2 1EZ, UK (fax: +44-1223-336033; e-mail: deposit@ccdc.cam.ac.uk or via http://www.ccdc.cam.ac.uk/data_request/cif). Crystal data and details concerning the data collection are given in Table 3-1. All non-hydrogen atoms were refined anisotropically. Hydrogen atoms were located in the calculated positions and refined by using a riding.

Table 3-1. Crystallographic data of five-coordinate $[\text{Fe}^{\text{III}}\text{TMP}(4\text{-NMe}_2\text{PyNO})]\text{ClO}_4$ at 100 K

| Compound | $[\text{Fe}(\text{TMP})(4\text{-NMe}_2\text{-PyNO})]\text{ClO}_4 \cdot 0.5$ toluene, 1.18 Hexane, CH_2Cl_2 |
|---|---|
| Temperature (K) | 100(2) |
| Chemical formula | $\text{C}_{63}\text{H}_{62}\text{N}_6\text{OFeClO}_4 \cdot 0.5(\text{C}_7\text{H}_8)$, 1.18(C_6H_{14}), (CH_2Cl_2) |
| Formula weight | 1307.21 |
| Crystal size (mm) | 0.220 X 0.180 X 0.060 |
| Crystal color | brown, block |
| Crystal system | Triclinic |
| Space group | $P\bar{1}$ |
| Wave length (\AA) | 0.71075 |
| a (\AA) | 13.6720(4) |
| b (\AA) | 13.9707(4) |
| c (\AA) | 20.2511(6) |
| α ($^\circ$) | 73.536(2) |
| β ($^\circ$) | 77.425(2) |
| γ ($^\circ$) | 82.207(2) |
| Volume (\AA^3) | 3609.23(19) |
| Z | 2 |
| Density (Calculated) (g cm^{-3}) | 1.203 |
| Absorption coefficient (mm^{-1}) | 0.372 |
| Absorption correction | multi-scan |
| Max. and Min. transmission | 0.978 and 0.934 |
| F (000) | 1382.00 |
| θ Range for data collection ($^\circ$) | 1.992 to 28.00 |
| Index ranges | $-18 \leq h \leq 18$, $-18 \leq k \leq 18$, $-26 \leq l \leq 26$ |
| Reflections collected | 17381 |
| Independent reflections | 10496 [$R_{\text{int}} = 0.0702$] |
| Refinement method | Full-matrix least-squares on F^2 |
| Data/restraints/parameters | 17381 / 696 / 1002 |
| Goodness-of-fit on F^2 | 1.001 |
| Final R indices ($I > 2s(I)$) | $R_1 = 0.0985$, $wR_2 = 0.2482$ |
| R indices (all data) | $R_1 = 0.1556$, $wR_2 = 0.2865$ |
| Largest peak and hole (e \AA^{-3}) | +0.870 and -0.999 |

3.3 Results and Discussion

3.3.1 Structural, spectroscopic, and magnetic properties for the five-coordinate iron(III) complex $[\text{Fe}^{\text{III}}(\text{TMP})(4\text{-NMe}_2\text{PyNO})]\text{ClO}_4$

3.3.1.1 X-ray Crystallography

As shown in Figure 3-3, molecular structure of five-coordinate iron(III) complex $[\text{Fe}^{\text{III}}(\text{TMP})(4\text{-NMe}_2\text{PyNO})]\text{ClO}_4$ was determined by X-ray crystallography at 100 K. Table 3-2 lists the selected structural parameters. The axially coordinated a 4-NMe₂PyNO molecule and four mesityl groups at *meso*- position are clearly observed. The Fe-O-N angles between the Fe(III) ion and the coordinated axial ligands are 118.9(3) °. The dihedral angle between the ring plane of an axially coordinated 4-NMePyNO molecule and the least-square plane of the heme core was 23.7 °. The structure of the porphyrin ring is almost planar in spite of five-coordinated conformation. The largest deviations of carbon and nitrogen atoms in macrocycle from the least-square plane of the C₂₀N₄ porphyrinato core are 0.123 and 0.084 Å, respectively, which are very small values. In

addition, the calculated RMS value on the basis of the deviation of 24 atoms from the mean porphyrin plane is quite small (0.059 Å) as compared with one of the related complexes. For example, the five-coordinate iron(III) *meso*-tetraalkylporphyrin complexes, [Fe(TⁿPrP)Cl] and [Fe(TⁱPrP)Cl] (TⁿPrP = tetrapropylporphyrin, TⁱPrP = tetraisopropylporphyrin), have reported the deformed ruffling structures by Ikeue et al. [25,26]. In [Fe^{III}(TMP)(4-NMe₂PyNO)]ClO₄, the torsion angle between the four macrocycle nitrogen atoms is 1.667°. The Fe(III) ion is located in a distorted square-pyramidal coordination geometry and is displaced from the least-squares plane of macrocycle (C₂₀N₄) by 0.43 Å toward the oxygen atom of the axially coordinated 4-NMe₂PyNO molecule. The average bond length for Fe–N_{por} is 2.053 Å. These parameters are consistent with the parameter observed for five-coordinated iron(III) porphyrin complexes with high spin $S = 5/2$ state [27-29]. Displacements of iron(III) ion from heme plane and bond lengths Fe–N_{por} for [Fe(TPP)I] and [Fe(TPP)NCS] are 0.53, 2.060 Å and 0.49, 2.065 Å, respectively [30]. On the other hand, Fe–O_{ax} bond length for [Fe^{III}(TMP)(4-NMe₂PyNO)]ClO₄ is 1.912 Å. Fe–axial ligand distances in five-coordinate iron(III) porphyrin complexes with high spin $S = 5/2$ state range from 1.905 Å in [Fe(TPP)(2,6-Cl₂pcyd)] to 2.554 Å in [Fe(TPP)I]; pcyd is phenylcyanamide [29,30].

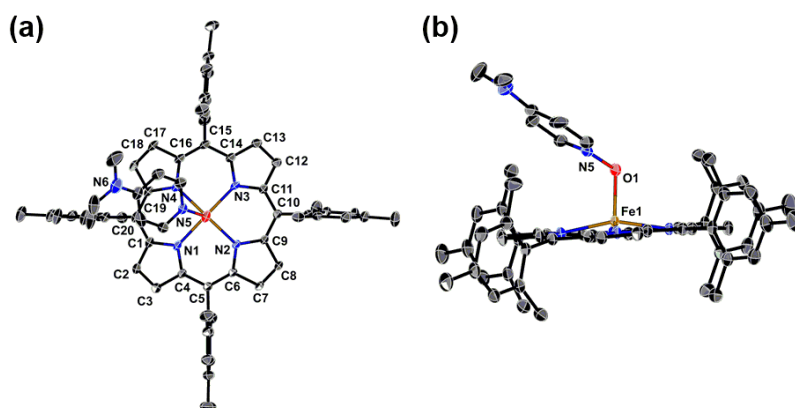


Figure 3-3. ORTEP drawing of five-coordinate [Fe^{III}TMP(4-NMe₂PyNO)]ClO₄ (100 K); (a) side view and (b) top view, showing the thermal ellipsoids with some atom labeling at the 30% probability level. Hydrogen, solvent, and counter anion atoms are omitted for clarity.

Table 3-2. Structural parameters of five-coordinate [Fe^{III}TMP(4-NMe₂PyNO)]ClO₄ at 100 K.

| Fe–N _{por} ^a / Å | Fe–O _{ax} ^b / Å | ΔFe ^c / Å | ΔC ^d / Å | ΔN ^e / Å | τ ^f /° | RMS ^g /Å |
|--------------------------------------|-------------------------------------|-----------------------|----------------------|----------------------|-------------------|---------------------|
| 2.053(3) | 1.912(3) | 0.434 | 0.123 | 0.084 | 1.667 | 0.059 |

^a Average value of the four Fe–N(porphyrin) bond lengths.

^b Fe–O(axial ligand) bond length.

^c The out-of-plane displacement of Fe(III) ion.

^d The maximum out-of-plane displacement of Carbon atoms.

^e The maximum out-of-plane displacement of Nitrogen atoms.

^f The maximum torsion angle between the four macrocycle nitrogen atoms.

^g The RMS values for deformation of the macrocycles(C₂₀N₄).

3.3.1.2 SQUID Magnetometry

Magnetic behaviors of five-coordinate $[\text{Fe}^{\text{III}}(\text{TMP})(4\text{-NMe}_2\text{PyNO})]\text{ClO}_4$ were examined by SQUID magnetometry for the microcrystalline samples in 2–300 K range as shown in Figure 3-4. The effective magnetic moments (μ_{eff}) values were maintained at $5.3 \mu_{\text{B}}$ in the range 100–300 K, which is some lower than the spin-only value for a high spin $S = 5/2$ state, *i.e.* $\mu_{\text{eff}} = 5.9 \mu_{\text{B}}$. The five-coordinate $[\text{Fe}^{\text{III}}(\text{TMP})(4\text{-NMe}_2\text{PyNO})]\text{ClO}_4$ showed a drop of μ_{eff} below 20 K, and reached a value of $3.9 \mu_{\text{B}}$ at 2.0 K. This drop was ascribed to the zero-field splitting.

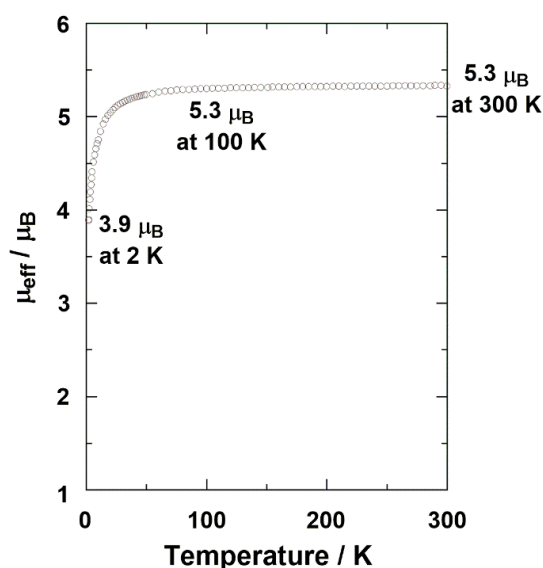


Figure 3-4. Temperature dependence of the effective magnetic moments of five-coordinate $[\text{Fe}^{\text{III}}\text{TMP}(4\text{-NMe}_2\text{PyNO})]\text{ClO}_4$ taken for micro-crystalline samples by SQUID magnetometry.

3.3.1.3 NMR Spectral Study

^1H NMR spectrum at 298 K and Curie plots of some proton signals at 183–303 K for five-coordinate $[\text{Fe}^{\text{III}}\text{TMP}(4\text{-NMe}_2\text{-PyNO})]\text{ClO}_4$ shown in Figure 3-5 were taken in CD_2Cl_2 solution. The assignment of all proton signals was carried out on the basis of the relative integral intensities and the signal widths, which indicated the five-coordinate conformation. The pyrrole-H signal appears at 65.1 ppm, which is quite close to the corresponding chemical shifts of the related six-coordinate high spin $S = 5/2$ state iron(III) porphyrin complexes with two substituted pyridine *N*-oxides as axial ligand at 298 K, *i.e.* $[\text{FeTMP}(4\text{-ClPyNO})_2]\text{BF}_4$: 59.8 ppm, $[\text{FeTMP}(\text{PyNO})_2]\text{BF}_4$: 63.6 ppm [19]. In addition, Curie plots of some proton signals at 183–303 K for five-coordinate $[\text{Fe}^{\text{III}}\text{TMP}(4\text{-NMe}_2\text{-PyNO})]\text{ClO}_4$ exhibited good linearity, which indicated no spin-crossover and/or no exchange of axial ligands in the range of 303 and 183 K. The positive slope of pyrrole-H clearly indicates that five-coordinate $[\text{Fe}^{\text{III}}\text{TMP}(4\text{-NMe}_2\text{-PyNO})]\text{ClO}_4$ adopts the high spin $S = 5/2$ state [31].

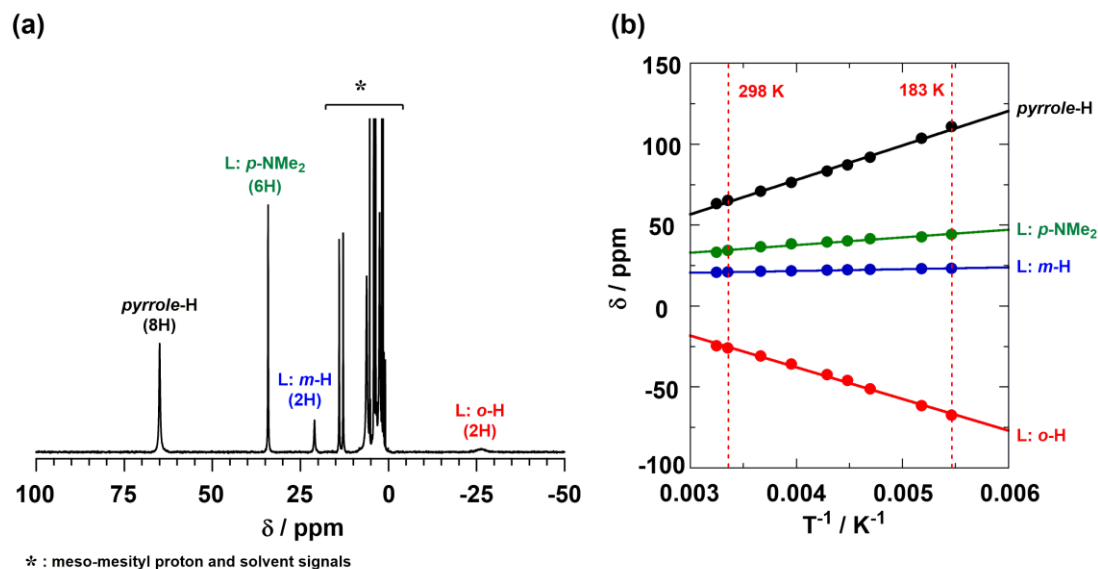


Figure 3-5. (a) ^1H NMR spectrum of five-coordinate $[\text{Fe}^{\text{III}}\text{TMP}(4\text{-NMe}_2\text{PyNO})]\text{ClO}_4$ taken in CD_2Cl_2 solution at 298 K. (b) Curie plots of some proton signals of five-coordinate $[\text{Fe}^{\text{III}}\text{TMP}(4\text{-NMe}_2\text{PyNO})]\text{ClO}_4$ taken in CD_2Cl_2 solution at 183-303 K.

3.3.2 Spectroscopic properties for five-coordinate $[\text{Fe}^{\text{III}}(\text{TMP})(4\text{-NMe}_2\text{PyNO})]\text{ClO}_4$ and six-coordinate $[\text{O}=\text{Fe}^{\text{IV}}(\text{TMP})(4\text{-NMe}_2\text{PyNO})]\text{ClO}_4$

Figure 3-6 (a) and (b) show the ESR spectra of five-coordinate $[\text{Fe}^{\text{III}}\text{TMP}(4\text{-NMe}_2\text{PyNO})]\text{ClO}_4$ in both of solid and solution states. The ESR spectra in solid and solution states exhibited both of axial type signals with $g_{\perp} = 5.52$ and 5.79 , and $g_{\parallel} = 1.99$ and 2.00 , respectively, which also

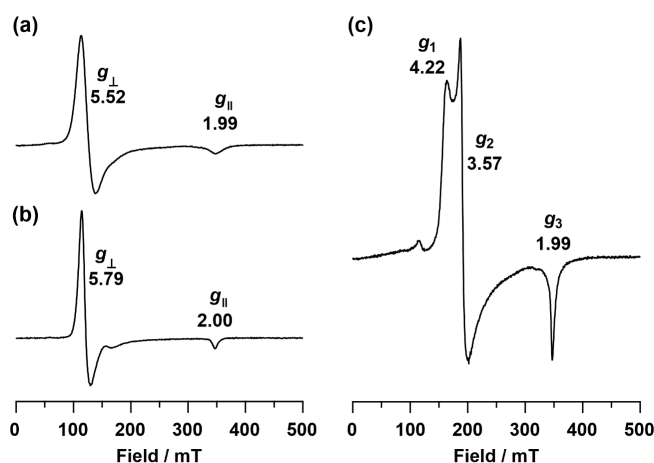
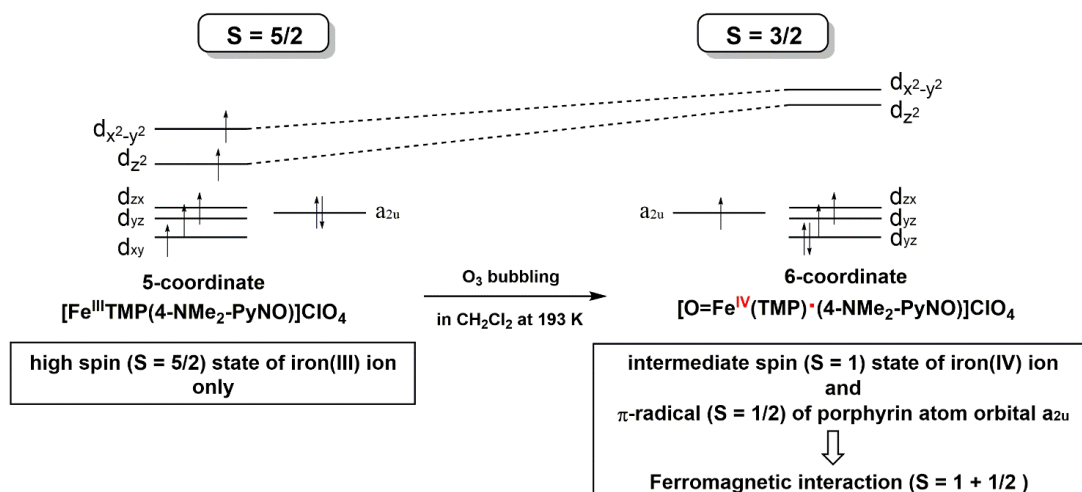


Figure 3-6. ESR spectra of five-coordinate $[\text{Fe}^{\text{III}}\text{TMP}(4\text{-NMe}_2\text{PyNO})]\text{ClO}_4$ measured in (a) the solid state at 4 K and (b) frozen CH_2Cl_2 -toluene solution at 15 K, and (c) six-coordinate $[\text{O}=\text{Fe}^{\text{IV}}(\text{TMP})(4\text{-NMe}_2\text{PyNO})]\text{ClO}_4$ taken in frozen CH_2Cl_2 -toluene solution at

indicated that five-coordinate $[\text{Fe}^{\text{III}}\text{TMP}(4\text{-NMe}_2\text{PyNO})]\text{ClO}_4$ maintains a pure high spin $S = 5/2$ state. As shown in Figure 3-6 (c), on the other hand, synthesized oxo iron(IV) porphyrin π -radical cation complex by the bubbling of O_3 , the ESR spectrum of six-coordinate $[\text{O}=\text{Fe}^{\text{IV}}(\text{TMP})\cdot(4\text{-NMe}_2\text{PyNO})]\text{ClO}_4$ exhibited axial type spectrum where three signals were observed at $g_1 = 4.22$, $g_2 = 3.57$, and $g_3 = 1.99$. The obtained signals were similar to those of $[\text{O}=\text{Fe}^{\text{IV}}(\text{TMP})^+]\text{ClO}_4$ and $[\text{O}=\text{Fe}^{\text{IV}}(\text{TMP})^+(2\text{-MeIm})]\text{ClO}_4$ [13,32]. The ESR spectrum of six-coordinate $[\text{O}=\text{Fe}^{\text{IV}}(\text{TMP})\cdot(4\text{-NMe}_2\text{PyNO})]\text{ClO}_4$ was typical of signals of $S = 3/2$ systems, indicating strong ferromagnetic interactions between the Fe(IV) ion (high spin $S = 1$ state) and the porphyrin π -radical cation ($S = 1/2$) as shown in Scheme 3-3. To further understand in detail, as revealed from the previous studies for $[\text{O}=\text{Fe}^{\text{IV}}(\text{TArP})^+]$, a porphyrin *meso*-substituent changed the reactivity and electronic state of the oxo iron(IV) porphyrin π -radical cation complex. Although the magnetic interaction between Fe(IV) ion and porphyrin π -radical cation spins was not drastically changed with an increase in the electron-withdrawing effect of *meso*-substituent, the ESR signals indicated a decrease in E/D value of the oxo iron(IV) porphyrin π -radical cation complex with an increase in the electron-withdrawing effect of *meso*-substituent. When the *meso*-substituent is much more electronegative, such as pentafluorophenyl, the orbital energy of the a_{2u} orbital would be lower than that of the a_{1u} orbital, leading the a_{1u} porphyrin π -radical cation state. the w spin $S = 1/2$ state with a $(d_{xy})^2(d_{xz}, d_{yz})^3$ electron configuration in both of solid and solution states. As a result, the EPR spectrum of $[\text{O}=\text{Fe}^{\text{IV}}(\text{TPFPP})^+]$ exhibited a broad signal around $g = 2$ at 4 K [33], suggesting very weak magnetic interaction.



Scheme 3-3 Electron configurations of five-coordinate $[\text{Fe}^{\text{III}}\text{TMP}(4\text{-NMe}_2\text{-PyNO})]\text{ClO}_4$ and six-coordinate $[\text{O}=\text{Fe}^{\text{IV}}(\text{TMP})\cdot(4\text{-NMe}_2\text{-PyNO})]\text{ClO}_4$.

3.4 Conclusion

The active centers in heme proteins such as cytochrome P450, peroxidase, and catalase have a very important function of electron transfer and enzyme by the difference of axial ligands. When the active site of peroxidase and catalase are activated by peroxides or peracids, they form an oxo iron(IV) porphyrin π -radical cation intermediate called Compound I. It is generally accepted that the diverse functions of compound I are controlled by heme environmental structures, such as porphyrin peripheral structures, heme axial ligands, and protein structures around heme. Therefore, elucidation of the electronic structures in a variety of iron porphyrin complexes as model compounds is quite important to understand the function and catalytic processes of naturally occurring heme proteins. The synthesis and characterization of five-coordinate iron(III) TMP complex with one 4-dimethylaminopyridine *N*-oxide (4-NMe₂PyNO) [Fe^{III}(TMP)(4-NMe₂PyNO)]ClO₄ as the precursor of high-valent oxo iron porphyrins in synthetic model systems were summarized. The molecular structure of five-coordinate iron(III) complex [Fe^{III}(TMP)(4-NMe₂PyNO)]ClO₄ was determined by X-ray crystallography at 100 K. While the porphyrin ring is almost planar (RMS value is 0.059 Å), Fe(III) ion was displaced from the least-squares plane of macrocycle (C₂₀N₄) by 0.43 Å toward the oxygen atom of the axially coordinated 4-NMe₂PyNO molecule. The bond lengths for Fe–N_{por(ave.)} and Fe–O_{ax} were 2.053 and 1.912 Å, respectively. The effective magnetic moments (μ_{eff}) values were maintained at 5.3 μ_{B} in the range 100–300 K, corresponding to the high spin $S = 5/2$ state value. ¹H NMR spectrum at 298 K and Curie plots of some proton signals at 183–303 K for five-coordinate [Fe^{III}TMP(4-NMe₂-PyNO)]ClO₄ were taken in CD₂Cl₂ solution. The assignment of all proton signals was carried out on the basis of the relative integral intensities and the signal widths, which indicated the five-coordinate conformation. The pyrrole-H signal appears at 65.1 ppm, and Curie plots of some proton signals at 183–303 K exhibited good linearity, which indicated no spin-crossover and/or no exchange of axial ligands in the range of 303 and 183 K. The positive slope of *pyrrole*-H clearly indicates that five-coordinate [Fe^{III}TMP(4-NMe₂-PyNO)]ClO₄ adopts the high spin $S = 5/2$ state. The ESR spectra in solid and solution states exhibited both of axial type signals with $g_{\perp} = 5.52$ and 5.79, and $g_{\parallel} = 1.99$ and 2.00, respectively, which also indicated that five-coordinate [Fe^{III}TMP(4-NMe₂PyNO)]ClO₄ maintains a pure high spin $S = 5/2$ state.

Under the low temperature of 193 K, the solution of five-coordinate iron(III) porphyrin complex [Fe^{III}(TMP)(4-NMe₂PyNO)]ClO₄ in CH₂Cl₂ changed from the brown color to the green color by the bubbling of O₃, resulting in the six-coordinate oxo iron(IV) porphyrin π -radical cation complex. The ESR spectrum of six-coordinate [O=Fe^{IV}(TMP)(4-NMe₂PyNO)]ClO₄ exhibited axial type signals with $g_1 = 4.22$, $g_2 = 3.57$, and $g_3 = 1.99$, which was typical of signals of $S = 3/2$ systems, indicating strong ferromagnetic interactions between the Fe(IV) ion (high spin $S = 1$ state) and the porphyrin π -radical cation ($S = 1/2$). Consequently, I confirmed the procedure and

the spectroscopic property of six-coordinate oxo iron(IV) porphyrin π -radical cation complex bearing one 4-NMe₂PyNO as the model compound in catalase active center with tyrosine molecule.

3.5 References

- [1] E. Margoliash, A. Schejter, *Trends Biochem. Sci.* 1984, 9, 364.
- [2] D. Keilin, *Proc. R. Soc. London B: Biol. Sci.* 1925, 98, 312.
- [3] C. Slater, *J. Biol. Chem.* 2003, 278, 16455 - 16461.
- [4] *Biocatalysis Based on Heme Peroxidases* (Eds.: E. Torres, M. Ayala), Springer, 2010.
- [5] *Concepts and Models in Bioinorganic Chemistry* (Eds.: H. -B. Kraatz, N. Metzler-Nolte), WILEY-VCH, Weinheim, 2006.
- [6] D. Dolphin, *The Porphyrins*, Academic Press, New York, 1978.
- [7] H. Uehara, Y. Shisaka, T. Nishimura, H. Sugimoto, Y. Shiro, Y. Miyake, H. Shinokubo, Y. Watanabe, Osami Shoji, *Angew. Chem. Int. Ed.* 2017, 56, 15279 - 15283.
- [8] H. -P. Hersleth, U. Ryde, P. Rydberg, C. H. Görbitz, K. K. Andersson, *J. Inorg. Biochem.* 2006, 100, 460–476.
- [9] H. B. Dunford, *Heme Peroxidases*, Wiley-VCH, New York, 1999.
- [10] H. N. Kirkman, G. F. Gaetani, *Trends Biochem. Sci.* 2007, 32, 44–50.
- [11] I. G. Denisov, T. M. Makris, S. G. Sliger, I. Schlichting, *Chem. Rev.* 2005, 105, 2253–2278.
- [12] P. R. Ortiz de Montellano, *Cytochrome P450. Structure, Mechanism, and Biochemistry*, 2nd ed., Plenum Publishing Corporation, New York, 1995.
- [13] A. Takahashi, T. Kurahashi, H. Fujii, *Inorg. Chem.* 2009, 48, 2614–2625.
- [14] J. T. Groves, R. Quinn, T. J. McMurry, M. Nakamura, G. Lang, Brian Boso, *J. Am. Chem. Soc.*, 1985, 107, 354–360.
- [15] H. Sugimoto, H. -C. Tung, D. T. Sawyer, *J. Am. Chem. Soc.* 1988, 110, 2465–2470.
- [16] H. Fujii, T. Yoshimura, H. Kamada, *Inorg. Chem.* 1997, 36, 6142–6143.
- [17] H. Fujii, *Coord. Chem. Rev.* 2002, 226, 51–60.
- [18] S. Wolowiec, L. Latos-Grazynski, *Inorg. Chem.* 1998, 37, 2984.
- [19] Y. Ide, N. Murai, H. Ishimae, M. Suzuki, S. Mori, M. Takahashi, M. Nakamura, K. Yoshinod, T. Ikeue, *Dalton Trans.* 2017, 46, 242–249.
- [20] S. Stoll, A. Schweiger, *J. Magn. Reson.* 2006, 178, 42–55.
- [21] R. W. Wagner, D. S. Lawrence, J. S. Lindsey, *Tetrahedron Lett.* 1987, 28, 3069–3070.
- [22] C. T. Watson, S. Cai, N. V. Shokhirev, F. A. Walker, *Inorg. Chem.* 2005, 44, 7468–7484.
- [23] M. C. Burla, R. Caliendo, M. Camalli, B. Carrozzini, G. L. Cascarano, C. Giacobozzo, M. Mallamo, A. Mazzone, G. Polidori, R. Spagna, *J. Appl. Cryst.* 2012, 45, 357–361.

- [24] G. M. Sheldrick, *Acta Cryst.* 2015, C71, 3–8.
- [25] Y. Ohgo, T. Ikeue, M. Nakamura, *Acta. Cryst.* 1999, C55, 1817–1819.
- [26] T. Ikeue, Y. Ohgo, A. Uchida, M. Nakamura, H. Fujii, M. Yokoyama, *Inorg. Chem.* 1999, 38, 1276–1281.
- [27] D.V. Behere, R. Birdy, S. Mitra, *Inorg. Chem.* 1981, 20, 2786–2789.
- [28] W. R. Scheidt, *J. Porphyrin and Phthalocyanines* 2008, 12, 979–992.
- [29] H. Chiniforoshan, N. Safari, J. M. Nezhad, H. Hadadzadeh, A. H. Mahmoudkhani, *Inorg. Chim. Acta* 2006, 359, 2101–2106.
- [30] W. R. Scheidt, *Acc. Chem. Res.* 1977, 10, 339–345.
- [31] A. Hoshino, Y. Ohgo, M. Nakamura, *Inorg. Chem.* 2005, 44, 7333–7344.
- [32] H. Fujii, T. Yoshimura, H. Kamada, *Inorg. Chem.* 1996, 35, 2373–7377.
- [33] H. Fujii, *Chem. Lett.* 1994, 1491–1494.

Summary

As the author has described in this dissertation, to understand the electronic structure of active center in heme proteins, the author synthesized porphyrinoid complexes bearing the paramagnetic metal ions, confirmed the structure by X-ray crystal structure, and investigated the spectroscopic and magnetic properties both in solution and solid states by the UV-Vis, NMR, ESR, Mössbauer spectra, and SQUID measurements.

In first chapter, four-coordinate Ni(II) complex of pyrrolidine-fused pyrrocorphin was prepared by successive 1,3-dipolar cycloaddition reactions of an azomethine ylide to *meso*-tetra(pentafluorophenyl) porphyrin. The addition of excess pyridine to four-coordinate Ni(II) pyrrocorphin complex in toluene solution yielded five-coordinate Ni(II) pyrrocorphin complex with mono-pyridine molecule, which was then converted completely to six-coordinate Ni(II) pyrrocorphin complex with bis-pyridine molecules. The first oxidation potentials of four-coordinate Ni(II) complexes determined by Cyclic Voltammetry in CH₂Cl₂ solution were quite different; they showed a large decrease as the reduction of the porphyrin ring proceeds. In contrast, the first reduction potentials were not so sensitive to the difference in porphyrin structure. Consequently, the HOMO–LUMO gap (ΔE) was the smallest in four-coordinate Ni(II) pyrrocorphin complex, 1.45 V, as compared with Ni(II) porphyrin complex (2.34 V), Ni(II) chlorin complex (2.08 V), and Ni(II) isobacteriochlorin complex (1.88 V). The result was further verified by UV-Vis spectroscopy and DFT calculation. SQUID magnetometry for the microcrystalline sample revealed that six-coordinate Ni(II) pyrrocorphin complex with bis-pyridine molecules was paramagnetic with $S = 1$ spin state between 2 and 300 K. Correspondingly, ¹H NMR spectrum showed the *pyrrole* and *pyrrolidine* β -proton signals extremely downfield and upfield positions, respectively, supporting the presence of unpaired electrons. Close inspection of the chemical shifts suggested that the spin densities on *pyrrocorphin* α -carbon and nitrogen atoms are quite different as is revealed from the large difference in chemical shifts of the *pyrrolidine* β -proton signals at –21.0, –17.5, and –0.93 ppm. UV-Vis and NMR titration experiments have shown that the binding constant of pyridine to six-coordinate Ni(II) pyrrocorphin complex with bis-pyridine molecules is ca. 4 times as large as that of Ni(II) isobacteriochlorin complex. The difference was ascribed to the fact that four-coordinate Ni(II) pyrrocorphin complex has longer a Fe–N(porphyrin) length than the other three complexes. Thus, the pyridine ligand prefers the electron deficient Ni(II) in six-coordinate Ni(II) pyrrocorphin complex, resulting in the larger binding constant as compared with other three complexes.

In second chapter, as an extension of our work on seeking for the new spin-crossover system, the author have examined the electronic, magnetic, and structural properties of iron(III) *meso*-tetramesitylporphyrin cation complexes [Fe(TMP)L₂]⁺, *meso*-tetra(perfluorophenyl)porphyrin

cation complex $[\text{Fe}(\text{TPFPP})\text{L}_2]^+$, *meso*-tetraphenylporphyrin cation complex $[\text{Fe}(\text{TPP})\text{L}_2]^+$, octaethylporphyrin cation complexes $[\text{Fe}(\text{OEP})\text{L}_2]^+$ *para*- or *meta*-substituted pyridine *N*-oxides ($\text{L} = 4\text{-XPyNO}$ or $3,5\text{-Me}_2\text{PyNO}$; $\text{X} = \text{Cl}, \text{H}, \text{Me}, \text{OMe}, \text{NMe}_2$) as axial ligands. Among them, molecular structures of some sample were determined by X-ray crystallography at 100 K. In each complex, the porphyrin ring is almost planar and the iron(III) ion is located within the porphyrin plane perfectly. In the case of a series of $[\text{Fe}(\text{TMP})\text{L}_2]^+$, stepwise decrease of both Fe-N_p and Fe-O bonds on going from $[\text{Fe}(\text{TMP})(4\text{-ClPyNO})_2]^+$ and $[\text{Fe}(\text{TMP})(3,5\text{-Me}_2\text{PyNO})_2]^+$ to $[\text{Fe}(\text{TMP})(4\text{-MePyNO})_2]^+$, and then to $[\text{Fe}(\text{TMP})(4\text{-NMe}_2\text{PyNO})_2]^+$ indicate the removal of an electron from both $d_{x^2-y^2}$ and d_z^2 orbitals due to the destabilization of the corresponding d orbitals, which in turn indicates that $[\text{Fe}(\text{TMP})(4\text{-ClPyNO})_2]^+$ adopts the $S = 5/2$ state while $[\text{Fe}(\text{TMP})(4\text{-NMe}_2\text{PyNO})_2]^+$ adopt the $S = 1/2$ state at 100 K. In addition, both the average Fe-N_p and Fe-O lengths in $[\text{Fe}(\text{TMP})(4\text{-MePyNO})_2]^+$ have increased by 0.019 and 0.047 Å, respectively, when the temperature is raised to 300 K. As the models for the prosthetic group in heme proteins, structures of six-coordinate $[\text{Fe}(\text{OEP})(4\text{-MePyNO})_2]^+$ and $[\text{Fe}(\text{OEP})(4\text{-NMe}_2\text{PyNO})_2]^+$ were confirmed by the single-crystal X-ray analysis. Both the average Fe-N_p and Fe-O lengths are thought to be the cause of the difference of the field strength of axial ligands and the steric hindrance and the electron property of ring-periphery substituents. As the general tendency, the six-coordinate iron(III) porphyrin complexes with neutral oxygen ligands adopt a high-spin state in a wide range of temperature. By using of X-ray crystal structure, SQUID, Mössbauer, ESR, and NMR measurements results, however, the author has found that $[\text{Fe}(\text{TPFPP})(4\text{-NMe}_2\text{PyNO})_2]^+$ is the first example of six-coordinated iron(III) porphyrin that adopts the $S = 1/2$ state. Furthermore, some of these complexes have shown spin-crossover phenomenon between high-spin ($S = 5/2$) and low-spin ($S = 1/2$) with a $(d_{xy})^2(d_{xz}, d_{yz})^3$ electron configuration states both in solution and solid states. The difference in the magnetic behaviours in $[\text{Fe}(\text{TMP})(4\text{-NMe}_2\text{PyNO})_2]^+$ and $[\text{Fe}(\text{TPFPP})(4\text{-NMe}_2\text{PyNO})_2]^+$ as compared with those in $[\text{Fe}(\text{TMP})\text{L}_2]^+$ ($\text{L} = 4\text{-XPyNO}$ or $3,5\text{-Me}_2\text{PyNO}$; $\text{X} = \text{Cl}, \text{H}, \text{Me}, \text{OMe}, \text{NMe}_2$), should be ascribed to the strong electron donating dimethylamino group in the former complexes, which should raise the energy level of the d_z^2 orbital and consequently stabilize the low-spin state. In addition, the electron withdrawing group at the *meso* positions stabilizes the d_π -type rather than the d_{xy} -type low-spin state. It is expected that the coordination strength of the porphyrin ring is weakened by the electron withdrawing groups at the *meso* positions. Consequently, the axial coordination should be strengthened, which stabilizes the low-spin state.

In third chapter, the active centers in heme proteins such as cytochrome P450, peroxidase, and catalase have a very important function of electron transfer and enzyme by the difference of axial ligands. When the active site of peroxidase and catalase are activated by peroxides or peracids, they form an oxo iron(IV) porphyrin π -radical cation intermediate called Compound I. It is

generally accepted that the diverse functions of compound I are controlled by heme environmental structures, such as porphyrin peripheral structures, heme axial ligands, and protein structures around heme. Therefore, elucidation of the electronic structures in a variety of iron porphyrin complexes as model compounds is quite important to understand the function and catalytic processes of naturally occurring heme proteins. The synthesis and characterization of five-coordinate iron(III) TMP complex with one 4-dimethylaminopyridine *N*-oxide (4-NMe₂PyNO) [Fe^{III}(TMP)(4-NMe₂PyNO)]ClO₄ as the precursor of high-valent oxo iron porphyrins in synthetic model systems were summarized. The molecular structure of five-coordinate iron(III) complex [Fe^{III}(TMP)(4-NMe₂PyNO)]ClO₄ was determined by X-ray crystallography at 100 K. While the porphyrin ring is almost planar (RMS value is 0.059 Å), Fe(III) ion was displaced from the least-squares plane of macrocycle (C₂₀N₄) by 0.43 Å toward the oxygen atom of the axially coordinated 4-NMe₂PyNO molecule. The bond lengths for Fe–N_{por}(ave.) and Fe–O_{ax} were 2.053 and 1.912 Å, respectively. The effective magnetic moments (μ_{eff}) values were maintained at 5.3 μ_{B} in the range 100–300 K, corresponding to the high spin $S = 5/2$ state value. ¹H NMR spectrum at 298 K and Curie plots of some proton signals at 183–303 K for five-coordinate [Fe^{III}TMP(4-NMe₂-PyNO)]ClO₄ were taken in CD₂Cl₂ solution. The assignment of all proton signals was carried out on the basis of the relative integral intensities and the signal widths, which indicated the five-coordinate conformation. The pyrrole-H signal appears at 65.1 ppm, and Curie plots of some proton signals at 183–303 K exhibited good linearity, which indicated no spin-crossover and/or no exchange of axial ligands in the range of 303 and 183 K. The positive slope of pyrrole-H clearly indicates that five-coordinate [Fe^{III}TMP(4-NMe₂-PyNO)]ClO₄ adopts the high spin $S = 5/2$ state. The ESR spectra in solid and solution states exhibited both of axial type signals with $g_{\perp} = 5.52$ and 5.79, and $g_{\parallel} = 1.99$ and 2.00, respectively, which also indicated that five-coordinate [Fe^{III}TMP(4-NMe₂PyNO)]ClO₄ maintains a pure high spin $S = 5/2$ state. Under the low temperature of 193 K, the solution of five-coordinate iron(III) porphyrin complex [Fe^{III}(TMP)(4-NMe₂PyNO)]ClO₄ in CH₂Cl₂ changed from the blown color to the green color by the bubbling of O₃, resulting in the six-coordinate oxo iron(IV) porphyrin π -radical cation complex. The ESR spectrum of six-coordinate [O=Fe^{IV}(TMP)(4-NMe₂PyNO)]ClO₄ exhibited axial type signals with $g_1 = 4.22$, $g_2 = 3.57$, and $g_3 = 1.99$, which was typical of signals of $S = 3/2$ systems, indicating strong ferromagnetic interactions between the Fe(IV) ion (high spin $S = 1$ state) and the porphyrin π -radical cation ($S = 1/2$). Consequently, I confirmed the procedure and the spectroscopic property of six-coordinate oxo iron(IV) porphyrin π -radical cation complex bearing one 4-NMe₂PyNO as the model compound in catalase active center with tyrosine molecule.

Finally, owing to the fruitful development of the synthesis of porphyrinoids, porphyrinoids with paramagnetic properties have gained potent tools to create various types of porphyrin-based materials and to reveal a variety of reactivities and mechanism in heme and chromophore by

spectroscopic and magnetic measurements. Consequently, porphyrinoid chemists can now focus on exploring the properties and functions of sophisticated porphyrinoid complexes. The important goal for chemists is to achieve intriguing and useful properties and functions of materials not the synthesis itself. To approach this goal, new design concepts of functional porphyrins are strongly awaited.

List of Publications

1. Y. Harada, T. Ikeue, **Y. Ide**, Y. Kimura, I. Hiromitsu, D. Yoshioka, M. Mikuriya, Y. Kataoka, M. Handa, Synthesis, structures, and properties of lantern-type dinuclear ruthenium(II,III) complexes cis-[Ru₂{3,5-(CF₃)₂-pf}₂(O₂CMe)₂Cl] and [Ru₂{3,5-(CF₃)₂-pf}₃(O₂CMe)Cl], 3,5-(CF₃)₂-pf⁻ = *N,N'*-bis[3,5-bis(trifluoromethyl)phenyl]formamidinate anion, *Inorg. Chim. Acta*, Elsevier, 2015, 424, 186–193.
2. **Y. Ide**, T. Ikeue, Y. Kataoka, R. Inoue, M. Nakamura, D. Yoshioka, M. Mikuriya, T. Kawamoto, M. Handa, Preparation, structure, and dynamic and electrochemical behaviors of dinuclear rhodium(I) complexes with bridging formamidinato ligands, *J. Organomet. Chem.*, Elsevier, 2016, 803, 92–103.
3. **Y. Ide**, N. Murai, H. Ishimae, M. Suzuki, S. Mori, M. Takahashi, M. Nakamura, K. Yoshino, T. Ikeue, Spin-crossover between high-spin (S=5/2) and low-spin (S=1/2) states in six-coordinate iron(III) porphyrin complexes having two pyridine-*N* oxide derivatives, *Dalton Trans.*, Royal Society of Chemistry(RSC), 2017, 46, 242–249.
4. R. Fujishiro, H. Sonoyama, **Y. Ide**, S. Mori, T. Sugimori, A. Nagai, K. Yoshino, M. Nakamura, T. Ikeue, Molecular Structure and Spectroscopic Properties of 2,3,9,10,16,17,23,24-Octakis(3-carboxyphenoxy)phthalocyaninato-κ⁴N](pyridine-κN)zinc(II) Pyridine Octasolvate, *Heterocycles*, The Japan Institute of Heterocyclic Chemistry, 2017, 94, 131–139.
5. T. Tanaka, S. Ooi, **Y. Ide**, T. Ikeue, M. Suzuki, P. P.-Y. Chen, M. Takahashi, A. Osuka, Different Antiferromagnetic Coupling between 5,5'- and 10,10'-Linked Iron(III) Corrole Dimers, *Eur. J. Inorg. Chem.*, Wiley-VCH, 2017, 2017, 1374–1381.
6. **Y. Ide**, Y. Yamada, S. Mori, T. Ikeue, Crystal Structure of a Six-coordinated (2,3,7,8,12,13,17,18-Octaethylporphyrinato) iron(III) Complex with Two 4-methylpyridine *N*-oxides, *X-ray Struct. Anal. Online*, The Japan Society for Analytical Chemistry(JSAC), 2017, 33, 25–27.
7. **Y. Ide**, H. Hosoda, H. Ishimae, S. Mori, T. Ikeue, Crystal Structure of a Six-coordinated [5,10,15,20-Tetrakis(2,4,6-trimethylphenyl)porphyrinato-κ⁴N] iron(III) Complex with Two 3,5-dimethylpyridine *N*-oxides, *X-ray Struct. Anal. Online*, The Japan Society for Analytical Chemistry(JSAC), 2017, 33, 49–51.
8. **Y. Ide**, T. Kuwahara, S. Takeshita, R. Fujishiro, M. Suzuki, S. Mori, H. Shinokubo, M. Nakamura, K. Yoshino, T. Ikeue, Nickel (II) pyrrocorphin: Enhanced binding ability in a highly reduced porphyrin complexes, *J. Inorg. Biochem.*, Elsevier, 2018, 178, 115–124.
9. T. Yoshida, K. Takahashi, **Y. Ide**, R. Kishi, J. Fujiyoshi, S. Lee, Y. Hiraoka, D. Kim, M. Nakano, T. Ikeue, H. Yamada, H. Shinokubo, Benzonorcorrole Ni(II) Complexes: Enhancement of Paratropic Ring Current and Singlet Diradical Character by Benzo-Fusion, *Angew. Chem. Int. Ed.*, Wiley-VCH, 2018, 57, 2209–2213.

List of Domestic Presentations

[Oral Presentations]

1. ○井手雄紀, 池上崇久, 井上諒子, 吉岡大輔, 御厨正博, 半田 真, 嵩高い置換基を有するホルムアミジナートイオンとシクロオクタジエンが配位したロジウム(I)二核錯体の構造と性質, 2013年日本化学会中国四国支部大会, 2P26, 広島大学(広島), (2013年11月).
2. ○井手雄紀, 井上諒子, 池上崇久, 吉岡大輔, 御厨正博, 半田 真, ホルムアミジナートイオンとシクロオクタジエンを配位子とするロジウム二核錯体の構造と性質, 日本化学会第93春季年会, 4B5-12, 立命館大学(滋賀), (2013年3月).
3. ○Yuki IDE, Takahisa IKEUE, Ryoko INOUE, Daisuke YOSHIOKA, Masahiro MIKURIYA, Makoto HANDA, *N,N'*-Diarylformamidinato-bridged Rhodium Dinuclear Complexes with 1,5-Cyclooctadiene, 錯体化学会第63回討論会, 11a-06, 琉球大学(沖縄), (2013年11月).
4. ○Yuki Ide, Takahisa Ikeue, Ryoko Inoue, Daisuke Yoshioka, Masahiro Mikuriya, Makoto Handa, Structures and Properties of Dinuclear Rhodium(I) Complexes with Formamidinato Bridging Ligands, 日本化学会第94春季年会, 1C1-09, 名古屋大学(愛知), (2014年3月).
5. ○井手雄紀, 池上崇久, 吉岡大輔, 御厨正博, 川本達也, 片岡祐介, 半田 真, ホルムアミジナートイオンとシクロオクタジエンが配位した三種のロジウム二核錯体の構造と性質, 錯体化学会第64回討論会, 1Ad-06, 中央大学(東京), (2014年9月).
6. ○Yuki Ide, Takahisa Ikeue, Daisuke Yoshioka, Masahiro Mikuriya, Tatsuya Kawamoto, Yusuke Kataoka, Makoto Handa, Dinuclear Rhodium(I) Complexes with Formamidinate and Cyclooctadiene, 「新規分子磁性化合物の探索」2014年シンポジウム, Lecture 18, 関西学院大学(兵庫), (2014年10月).
7. ○井手雄紀, 池上崇久, 吉岡大輔, 御厨正博, 川本達也, 片岡祐介, 半田 真, ホルムアミジナートイオンとノルボルナジエンを配位子とするロジウム二核錯体の構造と性質, 2014年日本化学会中国四国支部大会, 1C06, 山口大学(山口), (2014年11月).
8. ○井手雄紀, 池上崇久, 吉岡大輔, 御厨正博, 川本達也, 片岡祐介, 半田 真, ホルムアミジナートイオンを分子内架橋配位子とするロジウム二核錯体の構造と電気化学的性質, 日本化学会第95春季年会, 2F6-35, 日本大学(千葉), (2015年3月).
9. ○井手雄紀, 池上崇久, 吉岡大輔, 御厨正博, 半田 真, ホルムアミジナートイオンと酸素化されたシクロオクタジエンを有するロジウム二核錯体の合成と性質, 2015年日本化学会中国四国支部大会, 15SC04, 岡山大学(岡山), (2015年11月).
10. ○桑原孝光, 井手雄紀, 森 重樹, 鈴木優章, 池上崇久, 1,3-双極子環化付加反応によるピロコルフインニッケル(II)錯体の合成とその構造, 2016年日本化学会中国四国支部大会, 1J10, 香川大学(香川), (2016年11月).
11. ○石前裕樹, 井手雄紀, 山田祐也, 鈴木優章, 森 重樹, 高橋 正, 中村幹夫, 吉野勝美, 池上崇久, 種々のピリジン N-オキシドを軸配位子とするポルフィリン鉄(III)錯体のスピン状態, 2016年日本化学会中国四国支部大会, 2H09, 香川大学(香川), (2016年11月).

12. ○Yuki Ide, Hiroki Ishimae, Masaaki Suzuki, Shigeki Mori, Akira Ikezaki, Mikio Nakamura, Takahisa Ikeue, Structures and Magnetic Properties of Five- and Six-Coordinated Iron (III) Porphyrin Complexes with Axially Pyridine N-oxide Derivatives, 日本化学会第 97 春季年会, 3C2-18, 慶応義塾大学(神奈川県), (2017 年 3 月).
13. ○山田祐也, 細田 悠, 井手雄紀, 森 重樹, 根矢 三郎, 中村幹夫, 池上崇久, ペリジン N-オキシドを有するテトラアルキルポルフィリン鉄(III)錯体の構造と動的挙動, 日本化学会第 97 春季年会, 3C2-20, 慶応義塾大学(神奈川県), (2017 年 3 月).
14. ○田中隆行, 大井翔太, 井手雄紀, 池上崇久, 大須賀篤弘, 二種類のメゾメゾ結合コロール二量体鉄錯体の合成・構造及び磁気特性, 日本化学会第 97 春季年会, 3F6-09, 慶応義塾大学(神奈川県), (2017 年 3 月).
15. ○井手雄紀, 梅谷将隆, 細田 悠, 田中隆行, 大須賀篤弘, 池上崇久, *meso-meso* 位で連結した鉄(III)ポルフィリン二量体の磁氣的性質および ESR シミュレーション, 第 56 回電子スピンスイエンス学会年会 SEST2017, 3Ba7, 東京工業大学(東京), (2017 年 11 月).
16. ○井手雄紀, 山田祐也, 鈴木優章, 森 重樹, 根矢 三郎, 中村幹夫, 池上崇久, オキシペリポルフィリン鉄(III)錯体の構造および磁氣的性質, 2017 年日本化学会中国四国支部大会, OR208B, 鳥取大学(鳥取) (2017 年 11 月).

[Poster Presentations]

1. ○井手雄紀, 池上崇久, 井上諒子, 吉岡大輔, 御厨正博, 半田 真, 嵩高い置換基を有するホルムアミジナートイオンとシクロオクタジエンが配位したロジウム(I)二核錯体の構造と性質, 2013 年日本化学会中国四国支部大会, 2P26, 広島大学(広島), (2013 年 11 月).
2. ○井手雄紀, 池上崇久, 片岡祐介, 中村幹夫, 吉岡大輔, 御厨正博, 川本達也, 半田 真, ホルムアミジナートイオンを架橋配位子とするロジウム二核錯体の構造および動的挙動における研究, 錯体化学会第 65 回討論会, 1PA-46, 奈良女子大学(奈良), (2015 年 9 月).
3. ○井手雄紀, 池上崇久, 片岡祐介, 中村幹夫, 吉岡大輔, 御厨正博, 川本達也, 半田 真, ホルムアミジナートイオンを分子内架橋配位子とするロジウム二核錯体の電気化学的性質および動的挙動における研究, 第 26 回基礎有機化学討論会, 2P045, 愛媛大学(愛媛), (2015 年 9 月).
4. ○石前裕樹, 池上崇久, 井手雄紀, 原田靖子, 御厨正博, 吉岡大輔, 半田 真, 4 つのホルムアミジナートイオンを架橋配位子とするランタン型ルテニウム(II,III)二核錯体の電子状態, 2015 年日本化学会中国四国支部大会, 14P20, 岡山大学(岡山), (2015 年 11 月).
5. ○石前裕樹, 池上崇久, 井手雄紀, 原田靖子, 吉岡大輔, 御厨正博, 半田 真, 4 つの 3,5-ジクロロフェニルホルムアミジナートイオンが架橋したルテニウム(II,III)二核錯体のスピン状態, 2015 ハロゲン利用ミニシンポジウム(第 8 回臭素化学懇話会年会 in 松江), P-25, 島根大学(島根), (2015 年 11 月).

6. ○井手雄紀, 池上崇久, 吉岡大輔, 御厨正博, 半田 真, ハロゲンが導入された配位子を有する新規ロジウム二核錯体の構造と性質, 2015 ハロゲン利用ミニシンポジウム(第 8 回臭素化学懇話会年会 in 松江), P-26, 島根大学(島根), (2015 年 11 月).
7. ○井手雄紀, 石前裕樹, 鈴木優章, 森 重樹, 高橋 正, 中村幹夫, 吉野勝美, 池上崇久, 軸位にピリジン N-オキシドを有する鉄(III)ポルフィリン錯体の固体および溶液状態におけるスピントロスオーバー挙動, 第 27 回基礎有機化学討論会, 2P049, 広島国際会議場(広島), (2016 年 9 月).
8. ○井手雄紀, 石前裕樹, 山田祐也, 鈴木優章, 森 重樹, 中村幹夫, 池上崇久, ポルフィリン鉄(III)誘導体の電子状態および ESR シミュレーション, 第 55 回電子スピンスイエンズ学会年会 SEST2016, 2P14, 大阪市立大学(大阪), (2016 年 11 月).
9. ○竹下 翔, 井手雄紀, 鈴木優章, 森 重樹, 池上崇久, ピロコルフィン金属錯体の合成および分光学的性質の研究, 生体機能関連化学若手の会第 29 回サマースクール, P-21, 松江ニューアーバンホテル(島根), (2017 年 7 月).
10. ○井手雄紀, 細田 悠, 鈴木優章, 森 重樹, 中村幹夫, 吉野勝美, 池上崇久, ピリジン N-オキシドを軸位に有するポルフィリン鉄錯体の磁氣的性質, 生体機能関連化学若手の会第 29 回サマースクール, P-22, 松江ニューアーバンホテル(島根), (2017 年 7 月).
11. ○細田 悠, 井手雄紀, 鈴木優章, 吉野勝美, 池上崇久, meso-meso 位で連結したポルフィリン鉄(III)二核錯体の合成と性質, 生体機能関連化学若手の会第 29 回サマースクール, P-23, 松江ニューアーバンホテル(島根), (2017 年 7 月).
12. ○井手雄紀, 竹下 翔, 藤城 零, 鈴木優章, 森 重樹, 中村幹夫, 吉野勝美, 池上崇久, アゾメチンイリドを有するピロコルフィン金属錯体の合成と性質, 第 28 回基礎有機化学討論会, 1P013, 九州大学(福岡), (2017 年 9 月).
13. ○竹下 翔, 井手雄紀, 鈴木優章, 森 重樹, 吉野勝美, 池上崇久, ピロポルフィリン金属錯体の合成と性質, 2017 年日本化学会中国四国支部大会, OR25P, 鳥取産業体育館(鳥取), (2017 年 11 月).
14. ○細田 悠, 井手雄紀, 鈴木優章, 池上崇久, Meso-位で連結したポルフィリン鉄(III)二核錯体の合成と磁氣的性質, 2017 年日本化学会中国四国支部大会, OR32P, 鳥取産業体育館(鳥取), (2017 年 11 月).

List of International Presentations

[Oral Presentations]

1. ○Ikeue, T, **Ide, Y**, Mori, S, Nakamura, M, Structures and Magnetic Properties of Five- and Six- Coordinated Iron (III) Porphyrin Complexes with Axially Pyridine *N*-oxide Derivatives, 6th Asian Conference on Coordination Chemistry ACCC6, pp. 161, Melbourne, Australia (2017 年 7 月).

[Poster Presentations]

1. ○**Ide, Y**, Kuwahara, T, Fujishiro, R, Mori, S, Nakamura, M, Ikeue, T, Structure and Properties of Ni(II) Pyrrocorphin Complexes with azomethine ylides, 6th Asian Conference on Coordination Chemistry ACCC6, 190, Melbourne, Australia (2017 年 7 月).

List of Awards

1. 平成 25 年 11 月 2013 年日本化学会中国四国支部大会 学生優秀発表賞 受賞
○井手雄紀, 池上崇久, 井上諒子, 吉岡大輔, 御厨正博, 半田 真, 嵩高い置換基を有するホルム
アミジナートイオンとシクロオクタジエンが配位したロジウム(I)二核錯体の構造と性質, 2013
年日本化学会中国四国支部大会, 2P26, 広島大学(広島), (2013 年 11 月).
2. 平成 26 年 4 月 島根大学学生表彰 受賞

Acknowledgements

This dissertation deals with the studied accomplished by the author under the direction of Prof. Dr. Takahisa Ikeue in his laboratory at Shimane University.

First of all, the author would like to express his acknowledgement thanks to Prof. Dr. Takahisa Ikeue at Shimane University for the invaluable guidance and constant encouragement throughout the course of this research.

The author is also deeply grateful to Prof. Dr. Mikio Nakamura at Toho University, Prof. Dr. Masashi Takahashi at Toho University, and Prof. Dr. Akira Ikezaki at Toho University for their important discussions and guidance especially about the electronic structure investigations of iron(III) porphyrin complexes bearing paramagnetic metal ions.

The author would like to express his gratitude to Prof. Dr. Saburo Neya at Chiba University and Prof. Dr. Masaaki Suzuki at Shimane University for their generous and helpful cooperation.

Grateful acknowledgements are also made to Prof. Dr. Shigeki Mori at Ehime University for X-ray crystal structure analysis.

The author wishes to express their sincere thanks to Prof. Dr. Atsuhiko Osuka at Kyoto University, Prof. Dr. Hiroshi Shinokubo at Nagoya University, and Prof. Dr. Takayuki Tanaka at Kyoto University for their insightful suggestions and their generous help.

The author feels grateful to Prof. Dr. Toshikazu Nakamura at Institute for Molecular Science and Prof. Dr. Mizue Asada at Institute for Molecular Science for ESR measurement and simulation and fruitful suggestions.

The author would like to thank Prof. Dr. Katsumi Yoshino at Shimane Institute for Industrial Technology, Prof. Dr. Atsushi Nagai at Shimane University, and Prof. Dr. Tamotsu Sugimori at Toyama University for fruitful suggestions about spectroscopic properties, pharmacological activity experimental, and measurement of MALDI-TOF-Mass Spectra.

The author sincerely thanks Prof. Dr. Michiko Egawa at Shimane University for her measurements of elemental analysis.

The author appreciates Prof. Dr. Dongho Kim at Yonsei University, Korea, Prof. Dr. Peter P. -Y. Chen at National Chung Hsing University, Taiwan, Prof. Dr. Hiroko Yamada at Nara Institute of Science and Technology, Prof. Dr. Masayoshi Nakano at Osaka University, Prof. Dr. Masahiro Mikuriya at Kwansai Gakuin University, Prof. Dr. Makoto Handa at Shimane University, Prof. Dr. Hiroshi Sakiyama at Yamagata University, Prof. Dr. Ichiro Hiromitsu at Shimane University, Prof. Dr. Tatsuya Kawamoto at Kanagawa University, Prof. Dr. Yusuke Kataoka at Shimane University, Dr. Ryohei Kishi at Osaka University, Dr. Daisuke Yoshioka at Kwansai Gakuin University, Mr. Takuya Yoshida at Nagoya University, Mr. Yuya Hiraoka at Nagoya University, Mr. Kohtarō Takahashi at Nara Institute of Science and Technology, Mr. Jun-ya Fujiyoshi at Osaka University,

Mr. Sangsu Lee at Yonsei University, Korea, Ms. Ryoko Inoue at Shimane University, Ms. Yuko Kimura at Shimane University, and Ms. Yasuko Harada at Shimane University for their kind support and useful suggestion.

The author is also thankful to all members of Ikeue laboratory at Shimane University, especially, Mr. Rei Fujishiro, Mr. Hayato Sonoyama, Mr. Yuya Yamada, Mr. Syo Takeshita, Ms. Haruka Hosoda, Mr. Hiroki Ishimae, Mr. Takamitsu Kuwahara, and Ms. Nami Murai for discussion about syntheses and spectroscopic properties of porphyrinoid complexes and encouragements.

Finally, the author wants to thank his mother, Noriko Ide, his sister, Yukari Ide, his brother, Kouki Ide, and his father, Yukio Ide for their heartfelt encouragement and continuous assistant.

Yuki Ide